FIRST PRINCIPLES VIBRATIONAL SPECTRA OF TETRAHEDRALLY-BONDED GLASSES: SiO$_2$, GeO$_2$ AND GeSe$_2$

THÈSE N^O 3738 (2007)

PAR

Luigi GIACOMAZZI

Dottore in fisica, Università degli Studi di Padova, Italie
de nationalité italienne

EPFL

ÉCOLE POLYTECHNIQUE
FÉDÉRALE DE LAUSANNE

Lausanne, EPFL
2007

Résumé

Les materiaux vitreux, comme par example la silice amorphe (v-SiO$_2$), l'oxyde de germanium amorphe (v-GeO$_2$), et les verres de la famille des chalcogenides, dont un représentant est le diséléniure de germanium (v-GeSe$_2$), sont actuellement des matériaux clés dans plusieurs applications technologiques. Ils sont notamment employés dans la production des fibres optiques, des dispositifs microélectroniques et pour le stockage d'informations. Cela est entre autres une des motivations qui justifient l'intérêt croissant dédié à l'étude de la structure des matériaux amorphes. Les techniques de diffraction, comme les rayons x et la diffraction des neutrons, appliquées aux matériaux amorphes peuvent seulement fournir une caractérisation partielle de la structure à l'échelle atomique, étant donné que ces matériaux manquent de symétrie translationelle. D'autres techniques experimentales, comme les spectroscopies vibrationelles, se montrent sensibles à la structure microscopique sousjacente. Cependant, extraire l'information structurelle de ce type de donnés experimentales, s'avère plutôt difficile et nécessite surtout une modélisation théorique soigneuse du matériau considéré.

Cette thèse est consacrée à l'étude Premiers-Principes des spectres vibrationels des verres v-SiO$_2$, v-GeO$_2$, et v-GeSe$_2$, dans lesquels les liaisons entre cations et anions donnent lieu à des structures formées principalement de tétrahèdres. Pour cette étude, on fera usage des méthodes basées sur la thèorie de la fonctionnelle de la densité qui nous permettront de calculer les spectres vibrationels d'un ensemble choisi de modèles structurels de ces matériaux. On fera, en particulier, recours à une technique nouvelle dernièrement développée qui consiste dans l'application d'un champ électrique fini, avec conditions périodiques au bord, permettant de déduire les facteurs de "coupling" nécessaires au calcul des spectres infrarouge et Raman.

À travers la comparaison de nos résultats avec les données experimentales de spectroscopies vibrationelles, et compte tenu des différences structurelles de nos modèles, on donnera une interprétation des principales caractéristiques des spectres. Par consequent on extraira des informations structurelles apportant un raffinement de nôtre connaissance des matériaux étudiés.

Mots-clés: amorphes, v-SiO$_2$, v-GeO$_2$, v-GeSe$_2$, spectres vibrationels, infrarouge, Raman, structure atomique, Premiers-Principes.

Abstract

Disordered oxides, such as vitreous silica (v-SiO$_2$) and vitreous germania, (v-GeO$_2$) and chalcogenide glasses, such as vitreous germanium diselenide (v-GeSe$_2$) are currently key materials in many technological fields, ranging from Si-based microelectronic to optical fibers and information storage devices production. Thus an increasing interest is nowadays devoted to understanding the structural arrangements of atoms in these materials. Diffraction probes like x-ray and neutron diffraction applied to amorphous materials can only partially characterize their atomic structure, since these materials lack translational symmetry. A complementary class of experimental techniques is constituted by vibrational spectroscopies, since the latter are also sensitive to the underlying structure. Yet, extracting structural information from the associated experimental data is rather difficult and above all it requires an accurate theoretical modeling of the material under investigation.

This thesis is dedicated to the first-principles investigation of vibrational spectra of the tetrahedrally bonded glasses v-SiO$_2$, v-GeO$_2$ and v-GeSe$_2$. To this aim, we make use of methods based on density functional theory which allow us to calculate vibrational spectra for a set of selected model structures for each one of these materials. We take advantage of a recent development which consists in applying a finite electric field under the constraint of periodic boundary conditions to calculate coupling factors, and hence to derive the infrared and Raman spectra. Through a comparison with experimental data of several vibrational spectroscopies, and by taking into account the structural differences of our models, we interpret features of the considered vibrational spectra. The extracted structural information represents a refinement of our knowledge of the investigated materials.

Keywords: vitreous materials, glasses, v-SiO$_2$, v-GeO$_2$, v-GeSe$_2$, vibrational spectra, infrared, Raman, atomic structure, first-principles methods.

Sommario

Gli ossidi amorfi, come ad esempio la silice amorfa (v-SiO$_2$), la germania amorfa (v-GeO$_2$), e i vetri della famiglia dei calcogenidi, di cui un rappresentante è il diseleniuro di germanio (v-GeSe$_2$), sono attualmente materiali chiave per molte applicazioni tecnologiche, che vanno dalle fibre ottiche, alla microelettronica basata sul silicio, fino alla produzione di dispositivi per la memorizzazione di informazione. Questa è una delle motivazioni che giustificano il crescente interesse dedicato alla comprensione e allo studio della struttura dei materiali amorfi. Le tecniche di diffrazione, come i raggi x e la diffrazione di neutroni, quando applicate ai materiali amorfi possono solo fornire una caratterizzazione parziale della struttura alla scala atomica, dato che questi materiali mancano di simmetria traslazionale. Altre tecniche sperimentali, come le spettroscopie vibrazionali, si mostrano sensibili alla struttura microscopica sottostante. Tuttavia, estrarre informazione strutturale da questo tipo di dati sperimentali risulta piuttosto difficile e soprattutto richiede un'accurata modellizzazione teorica del materiale che si sta investigando.

Questa tesi è dedicata allo studio da principi-primi degli spettri vibrazionali dei vetri v-SiO$_2$, v-GeO$_2$, and v-GeSe$_2$ nei quali il legame fra catione ed anioni da luogo a strutture formate principalmente da tetraedri. In questo studio si farà uso di metodi basati sulla teoria del funzionale densità che ci permetteranno di calcolare gli spettri vibrazionali di un gruppo scelto di modelli strutturali di questi materiali. Faremo, in particolare, ricorso ad una tecnica innovativa recentemente sviluppata che consiste nell'applicare un campo elettrico finito, con condizioni periodiche al bordo, per ricavare i fattori di coupling necessari per il calcolo degli spettri vibrazionali infrared e Raman. Attraverso il confronto con i dati sperimentali di diverse spettroscopie vibrazionali e tenendo conto delle differenze strutturali fra i nostri modelli, interpreteremo le caratteristiche principali degli spettri considerati, ricavandone informazione strutturale che rappresenta un raffinamento della nostra conoscenza dei materiali investigati.

Parole-chiave: amorfi, v-SiO$_2$, v-GeO$_2$, v-GeSe$_2$, spettri vibrazionali, infrared, Raman, struttura atomica, metodi da principi-primi.

Contents

Introduction

Amorphous materials are non-crystalline materials which feature randomness to some degree. An increasing interest is nowadays devoted to understanding their atomic structure due to the their wide range of applications in a variety of industrial sectors [1, 2].

Since amorphous materials lack translational symmetry, their atomic structure can only partially be characterized through diffraction probes such as x-ray and neutron diffraction. Complementary structural information can be achieved by applying other experimental probes sensitive to the underlying structure, such as vibrational spectroscopies. However, the interpretation of features in the vibrational spectra of amorphous materials constitutes a difficult task.

Our understanding of the structure of amorphous materials can be improved through the use of density functional methods, as recent applications to vitreous SiO_2 [3, 4] and B_2O_3 [5] have shown. The aim of any theoretical modeling approach consists in the generation of structural models for which the comparisons with all the available experimental data show a good agreement.

Among the vibrational spectroscopies, infrared and Raman spectroscopy are commonly used tools for investigating materials [6]. At variance, the main difficulty faced by theory in modeling the infrared and Raman spectra is given by the calculation of infrared oscillator strengths and Raman cross sections. Several requirements are necessary to calculate these quantities, including a reliable structural model, its vibrational modes, and finally the coupling matrix elements. Viable structural models of several types of glasses can be generated by using classical molecular dynamics [7, 8]. However, the calculation of vibrational modes constitutes a more critical issue. First-principles methods are generally required to accurately describe the vibrational properties [9].

This thesis is devoted to the investigation of the structural and dynamical properties of vitreous silica (v-SiO_2), vitreous germania (v-GeO_2), and vitreous germanium diselenide (v-$GeSe_2$), through the study of their vibrational spectra. To this end, we intend to use methods based on density functional theory which allow us to calculate vibrational spectra for model structures of these materials. Through a comparison with experimental data,

we aim to interpret the main features in these spectra and use the extracted information to refine our knowledge of the structural properties of the investigated materials.

Vitreous silica and vitreous germania

Disordered [1] oxides, such as v-SiO$_2$ and v-GeO$_2$, are currently key materials in many technological applications, ranging from optical fibers [10] to Si-based microelectronic devices [11]. These materials are also very important in geophysics where a detailed knowledge of their structure in the liquid and amorphous state, and their high-pressure behavior, is required to understand the physical properties of the earth mantel [12]. Furthermore, these oxides represent archetypical materials for the study of the vitreous state. Hence, both technological and fundamental interests justify the substantial efforts which have been devoted to the detailed characterization of their atomic structure. Experimental probes, such as neutron or x-ray diffraction, provide direct information on the structural arrangement in these oxides. The short-range order is characterized by regular bonding configurations in which the cation (Si or Ge) is located at the center of corner-sharing tetrahedra having O atoms at their corners. The disorder sets in at medium-range distances through a distribution of bond angles on O atoms [13, 14] and through a statistics of different ring sizes [15]. While the short-range order is well described by diffraction probes, structural arrangements on medium range distances are more difficult to access because of the variety of interfering correlations. Interestingly, the networks of v-SiO$_2$ and v-GeO$_2$ present noticeable differences on these length scales. The average Ge-O-Ge bond angle in v-GeO$_2$ is 133° (Ref. [14]), significantly lower than the corresponding Si-O-Si bond angle in v-SiO$_2$ (151°, Ref. [16]). Consequently, v-GeO$_2$ is characterized by a higher packing density of tetrahedra than v-SiO$_2$ [17]. These differences also suggest that the ring statistics of the two materials differ, favoring higher concentrations of small rings in v-GeO$_2$. More generally, understanding the structure of v-GeO$_2$ might provide information on structural reorganizations occuring in v-SiO$_2$ when subject to external pressure [18].

In v-SiO$_2$, the presence of small rings has long been debated. Finally two sharp defect lines (known as D$_1$ and D$_2$) [19, 20] in the Raman spectrum have definitely been assigned to breathing vibrations of oxygen atoms in four- and three-membered ring structures, respectively [21]. v-GeO$_2$ can be considered a structural analogous of v-SiO$_2$. However the HH Raman spectrum of the former glass does not show any sharp feature, although the higher packing density of tetrahedral units should favor a higher concentration of small rings in v-GeO$_2$ [Fig. 1 (right)]. The Raman spectrum is characterized by two shoulders known as X_1 and X_2 occurring on either side of the main Raman peak [Fig. 1 (left)]. In

---

[1] By disordered materials we mean materials lacking translational symmetry.
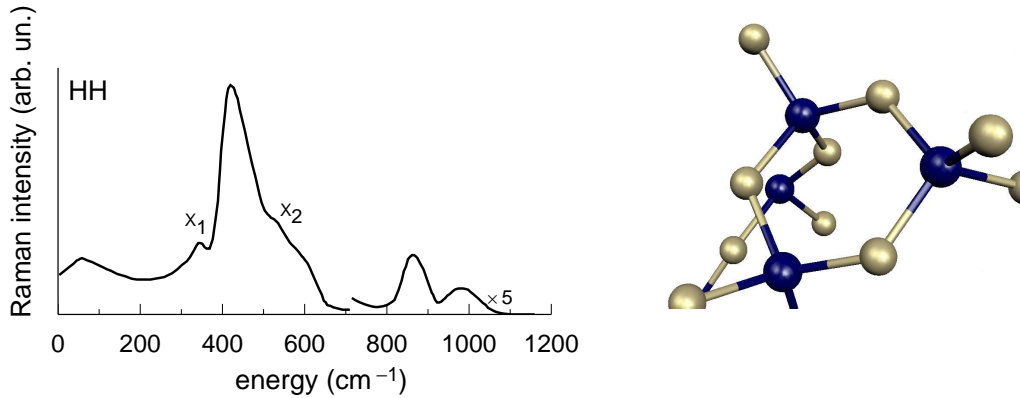
Figure 1: Left: experimental HH Raman spectrum of vitreous germania [22]. Right: a particular of the structure of v-GeO$_2$ showing a three-membered ring. Germanium and oxygen atoms are depicted with dark and bright colors, respectively.

analogy with the D_1 and D_2 lines, the X_2 shoulder has tentatively been assigned to three- or four-membered rings [22, 23]. The nature of X_1 has remained more elusive, although it is known from experiments that X_1 mainly involves Ge motion with a modest admixture of O motion [22].

First-principles investigations of v-SiO$_2$ have succeeded in assigning D_1 and D_2 lines to three- or four-membered rings, and more recently in giving an estimate of their concentrations [21, 4]. We expect, similarly, that an accurate theoretical description of vibrational spectra, in particular of the Raman spectra, would improve our understanding of the role played by three- and four-membered rings in v-GeO$_2$.

Vitreous germanium diselenide

After our investigations of v-SiO$_2$ and v-GeO$_2$, we consider v-GeSe$_2$, another archetypical material in glass science. Indeed v-GeSe$_2$ is one of the prototypical chalcogenide glasses. These materials are currently used in the field of information storage, for example, in high-capacity rewritable DVD optical memory disks [1].

Despite the similar stoichiometric formula, v-GeSe$_2$ shows a structure very different from that of other AX$_2$ glasses like v-GeO$_2$ or v-SiO$_2$. While v-GeO$_2$ and v-SiO$_2$ are well described by random networks of cornersharing tetrahedra [24], it has long been established that v-GeSe$_2$ also shows a considerable fraction [7] of edge-sharing tetrahedra [Fig. 2 (right)]. More strikingly, due to the close electronegativities of Ge and Se, the atomic structure of v-GeSe$_2$ can depart from chemical order and give rise to homopolar bonds, as shown in recent neutron diffraction experiments [25]. Moreover, first-principles molecular dynamics simulations of liquid GeSe$_2$ [26, 27] have shown the occurrence of a rich variety
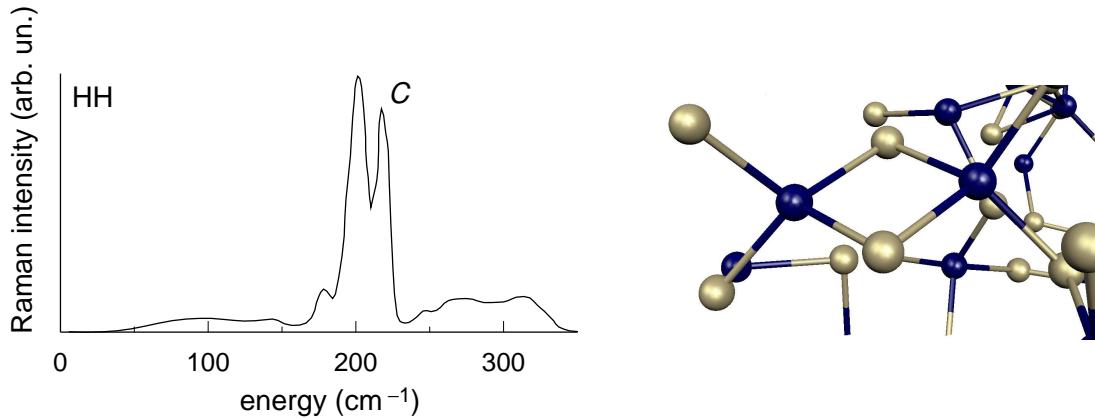
Figure 2: Left: experimental HH Raman spectrum of v-GeSe$_2$ [39]. The "companion line" is labelled with a C. Right: snapshot of the structure of v-GeSe$_2$. In particular two edge-sharing tetrahedra (four-atom ring) are shown. Germanium and selenium atoms are depicted in dark and bright colors, respectively.

of structural motifs, including not only homopolar bonds, but also over- and undercoordinated atoms.

Hence, the current theoretical and experimental situation leads to two contending conceptions of the structure of v-GeSe$_2$. To match experimental data [25], both structural conceptions should account for a small fraction of homopolar bonds. The first conception then corresponds to a structure with strong chemical order, in which the tetrahedral bonding nature of the network is respected to a very large extent, the main distinction with respect to v-GeO$_2$ and v-SiO$_2$ being the occurrence of edge-sharing tetrahedra. Model structures of this nature have indeed been generated via classical molecular dynamics [7]. The second conception is based on molecular dynamics simulations of the liquid which indicate a considerable fraction of nontetrahedral bonding configurations with over- and undercoordinated atoms [26, 27, 28]. A quench from the liquid would then give a vitreous structure which preserves these features [29]. Models generated according to either conception generally give structure factors in good agreement with experiment [7, 29, 30]. Thus diffraction data appear unable to clearly distinguish between the two kind of atomic structures. It is therefore highly desirable to determine the structure of v-GeSe$_2$ by considering also experimental results other than diffraction data. This could be achieved through accurate theoretical modeling of vibrational spectra.

Among the vibrational spectra of v-GeSe$_2$ particularly appealing is the HH Raman spectrum because of the so called "companion line" [cf. Fig. 2 (left)], the origin of which has long been debated [31, 32, 33, 34]. Recent work supports the assignment of this line to vibrations in edge-sharing tetrahedra [cf. Fig. 2 (right)]. The accurate modeling of v-GeSe$_2$ should also account for the Raman intensity of the companion line, and hence for the concentration of the edge-sharing tetrahedra.

Modeling of vibrational spectra

For v-SiO$_2$, v-GeO$_2$, and v-GeSe$_2$, vibrational spectra are currently routinely measured through inelastic neutron scattering (INS), infrared spectroscopy, and Raman scattering. The INS spectrum of these glasses is expected to closely resemble the vibrational density of states [35, 36]. Indeed, the interaction between the neutron and the lattice vibrations is mediated by atomic neutron scattering lengths, which are well known experimentally and do not depend on the electronic structure in the glass. At variance, the infrared and Raman spectra of v-SiO$_2$ and v-GeO$_2$ show important frequency-dependent modulations with respect to the vibrational density of states [3, 4, 37]. In these measurements, the electronic structure plays an important role in determining the coupling factors. Consequently, infrared and Raman spectra may differ considerably from the vibrational density of states. For instance, in the Raman spectrum of v-SiO$_2$ two sharp lines appear [19, 20] which do not have counterparts in the other vibrational spectra. In the case of v-GeSe$_2$, the analysis of the vibrational spectra is expected to carry similar information. For instance, the doublet in the Raman spectrum is absent both in the inelastic neutron and in the infrared spectra [38, 32, 39]. The sensitivity of the Raman spectrum to the underlying electronic structure is, in the case of v-GeSe$_2$, also expected to reveal homopolar bonding and miscoordinations.

It has recently been shown [4, 37] that Raman spectra in disordered oxides are highly sensitive to the oxygen bond angle distribution, thus offering an indirect structural probe for the connections between tetrahedra. This sensitivity is particularly valuable since it specifically highlights medium-range arrangements, which are more difficult to access through diffraction probes. However, the interpretation of vibrational spectra in terms of structural correlations is not trivial and can occur only through accurate theoretical modeling. Modeling approaches do not only face the difficulty of estimating coupling factors, but also require viable model structures and accurate vibrational properties. The aim of an optimal modeling approach then consists in determining a structural model through a virtuous circle in which intermediate models progressively show improved comparisons with experimental spectra.

An appropriate theoretical approach should meet several requirements. Structural models for disordered materials can be generated through simulation approaches of varying level of complexity. For instance, for v-SiO$_2$, v-GeO$_2$ and v-GeSe$_2$, classical molecular dynamics simulations yield model structures which generally compare well with diffraction data [40, 41, 7]. In principle, further structural refinement could be achieved with *ab initio* methodologies. However, as far as the vibrational properties are concerned, classical modeling approaches are generally not sufficiently accurate [35, 9]. Furthermore, the modeling of infrared and Raman coupling factors requires an explicit treatment of the

electronic structure. An additional constraint results from the necessity of treating model systems of relatively large size in order to describe the disordered nature of the oxide in an appropriate statistical way.

Density functional methodologies appear at present most suitable to address these issues. Vibrational properties of both crystalline [42] and disordered materials [35, 37, 5] are described with great accuracy. The description of the electronic structure gives access to infrared [3, 43] and Raman intensities [44, 45, 46]. Moreover, a recent development which consists in applying a finite electric field in conjunction with periodic boundary conditions allow one to calculate coupling factors for systems of relatively large size [47, 48].

Outline of the thesis

Using a density-functional scheme, we study the structural and vibrational properties of v-SiO$_2$, v-GeO$_2$ and v-GeSe$_2$. Through the use of classical and first-principles molecular dynamics methods, we generate a set of periodic model structures containing about hundred atoms. Our investigation of these model structures starts with a detailed structural analysis both in real and reciprocal spaces. Our study comprises the angular distributions, the atomic arrangements in the first-neighbor shells, the partial pair correlation functions, the total neutron correlation function, the neutron and x-ray total structure factors, the Faber-Ziman and Bhatia-Thornthon partial structure factors. We then obtain the vibrational frequencies and eigenmodes. We analyze the vibrational density of states in terms of motions of the component atomic species, and further in terms of rocking, bending, and stretching contributions. The inelastic neutron spectrum is found to differ only marginally from the vibrational density of states. Using a methodology based on the application of finite electric fields, we derive dynamical Born charge tensors and Raman coupling tensors. The knowledge of these coupling tensors and of the vibrational eigenmodes allow us to compute infrared and Raman spectra within a density-functional framework. For the infrared spectra, we calculate the real and imaginary parts of the dielectric function, including the high-frequency and static dielectric constants.

In our work on v-SiO$_2$ we consider three model structures of different size showing differences for medium-range properties, like ring statistics and intertetrahedral angle distributions. In our investigations, we mainly focused on the largest of the three models. Concerning the structural properties of this model, we find an overall good agreement with available experimental data. We compare the inelastic neutron and infrared spectra of our three models and find that the structural organization beyond nearest-neighbors only gives rise to minor differences in these spectra. At variance, the Raman spectrum is shown to be highly sensitive to the medium-range organization of the network. In partic-

ular, we focus on the relation between the content of three- and four-membered rings and the D_1 and D_2 lines in the Raman spectrum. Finally, we derive bond polarizability parameters from the calculated Raman coupling tensors and demonstrate their level of reliability in reproducing the spectra of v-SiO$_2$.

In our work on v-GeO$_2$ we consider a set of four model structures, differing by size, ring statistics, and intertetrahedral angle distributions. We focus in particular on the largest of them, for which we carry out an extensive analysis of the structure and find overall good agreement with available experimental data. Through a comparison between the Raman spectra of our models, we show that the Raman spectrum is sensitive to the medium-range structure. Furthermore, our investigation of Raman spectra supports an average Ge-O-Ge angle of 135°. We identify the shoulder X_2 as a signature of breathing O vibrations in three-membered rings. Four-membered rings are found to contribute to the main Raman peak. We advance an interpretation for the shoulder X_1 in terms of delocalized bond-bending modes. We derive bond polarizability parameters from the calculated Raman coupling tensors and demonstrate their level of reliability in reproducing the spectra of v-GeO$_2$.

In our study of v-GeSe$_2$ we generated a set of structural models that shows a varying degree of chemical disorder. In particular, two types of structural concepts are represented: one in which the tetrahedral order is preserved to a very large extent, and one which reproduces the high degree of disorder in first-neighbor shells found in first-principles molecular dynamics simulations of the liquid. Comparison with experimental x-ray and the neutron structure factors gives overall good agreement for the models of either structural conception. We then investigate the vibrational properties via the vibrational density of states and the inelastic neutron spectrum. The considered models yield similar spectra, which agree with experimental data. For infrared and Raman spectra, significant differences appear among the models. The comparison with experiment favors a model showing a high degree of chemical order. The Raman intensity is analyzed in terms of the underlying atomic vibrations. The assignment of the Raman companion line to Se motions in edge-sharing tetrahedra is supported.

In Chapter 1 we give a short introduction of the methods and techniques used in this thesis. Chapter 2 is devoted to the study of vitreous silica. For this purpose we consider three models of v-SiO$_2$, one of which is generated in this work. Furthermore we introduce, in this chapter, concepts and analyses that we will use throughout the rest of this thesis. Chapter 3 is dedicated to the study of vitreous germania. The structural and the vibrational properties of v-GeO$_2$ are discussed through the analyses of four models and through the comparisons with experiments. Chapter 4 is dedicated to the study of v-GeSe$_2$. We generate and analyse three models, corresponding to two contending conceptions of the

structure of v-GeSe$_2$. By comparing with experiments we discuss the reliability of these two structural conceptions. Finally, we draw the conclusions of the present thesis work.

Chapter 1

Methods

In this thesis, we proceed through several sequential steps. In the first step the main objective is to generate, at low computational cost, viable model structures which will subsequently be used in the study of vibrational spectra. We therefore begin by generating structural models using molecular dynamics techniques based on classical interaction potentials. In the case of both vitreous silica and germania, one can find classical potentials in the literature [8, 49] giving reasonable model structures, from which our study can begin. In the case of v-GeSe$_2$ classical potentials are less reliable because they give structures that are constituted of tetrahedra [7] alone, while chemical order is expected to be broken in the liquid and glassy state [50]. Therefore, in principle, it would be preferable to include a step of first-principles molecular dynamics simulations in the generation procedure of v-GeSe$_2$.

In the second step, a set of models is selected for an extended analysis of their vibrational properties. The selected models are further relaxed through a damped ab-initio molecular dynamics. The dynamical matrix is obtained by finite differences, recording the *ab initio* atomic forces for different finite displacements of the atoms along Cartesian directions. The vibrational frequencies and eigenmodes are then obtained by diagonalization. This method has been proved very successful both for v-SiO$_2$ and v-B$_2$O$_3$ [35, 3, 5].

For calculating infrared and Raman spectra, it is necessary to access coupling matrix elements. To this end, we will use a very recent method based on the application of a finite electric field in periodic density functional calculations [47]. In this method, the electronic structure is relaxed in the presence of a finite electric field. The infrared and Raman coupling elements are then obtained from the first and second derivatives of the atomic forces with respect to the electric field, respectively (cf. Sections 2.6.2 and 2.7). These derivatives can be calculated by finite differences with an additional computational effort that is negligible with respect to the calculation of the vibrations. Once all these data are available, the

analyses of the spectra in terms of the underlying vibrational modes will be made possible. In the next chapter, dedicated to the modeling of the structural and vibrational properties of v-SiO$_2$, we are going to give an explicit example of the generation and investigation procedures outlined above.

This chapter is devoted to the introduction of the basic theoretical tools we have used throughout this thesis. In Section 1.1 we give a concise introduction to classical molecular dynamics. We then describe (Secs. 1.1.1 and 1.1.2) the potentials that we used to generate our models of v-SiO$_2$, v-GeO$_2$, and v-GeSe$_2$. Finally, we give a short outline of the technique for carrying out first-principles molecular dynamics (Sec. 1.2) within a finite electric field (Sec. 1.2.1). The conclusions are given in Sec. 1.3.

1.1   Classical molecular dynamics

In this section, we give a description of classical molecular dynamics, as part of our model generation procedure, and we refer to [51] for an extensive treatise. In our investigations we took advantage of a code for classical molecular dynamics used in previous studies of disordered oxides [52].

Classical molecular dynamics is a tool that allows us to model systems of several thousands of atoms. The method is based on the Newtonian equations of motion. Molecular dynamics simulation consists in the numerical integration of the classical equations of motion, which for a simple atomic system of N atoms may be written

$$M_I \frac{d^2 \mathbf{R}_I}{dt^2} = \mathbf{F}_I \qquad \mathbf{F}_I = -\boldsymbol{\nabla}_I U \tag{1.1}$$

where M_I and $\mathbf{R}_I$ are the mass and position of the Ith atom. The numerical solutions of Eq. (1.1) are found by applying time integration algorithms based on finite differences methods [51]. In Eq. (1.1), the forces $\mathbf{F}_I$ acting on the atoms are derived from a potential energy $U(\mathbf{R}^N)$, where $\mathbf{R}^N = (\mathbf{R}_1, \mathbf{R}_1 \ldots \mathbf{R}_N)$ represents the complete set of the $3N$ atomic coordinates. Thus the reliability of the trajectories obtained by solving Eq. (1.1) is strongly dependent on the quality of the chosen potential.

The type of potential energy $U(\mathbf{R}^N)$ that we consider here is composed of two- and three-body terms only:

$$U(\mathbf{R}^N) = \sum_{J>I} \phi(\mathbf{R}_I, \mathbf{R}_J) + \sum_{K>J>I} \psi(\mathbf{R}_I, \mathbf{R}_J, \mathbf{R}_K). \tag{1.2}$$

In binary systems like SiO$_2$ and GeSe$_2$ the cohesion arises from the shortest bond, namely, the Si–O and Ge–Se bonds, respectively. This involves charge transfer from Si to O (or from Ge to Se), which imparts an ionic character to the bonds. The negative ions,

O^{2-} or Se^{2-}, have a large size and consequently large electronic polarizabilities, which lead to a very substantial charge-dipole interaction. Thus, the effective potential Eq. (1.2) for SiO_2 or $GeSe_2$-type systems should have at least three ingredients: the Coulomb interaction, charge-dipole interactions, and a steric repulsion to balance them. In SiO_2 and $GeSe_2$ three-body forces become important at medium-range length scales. For instance, in v-$GeSe_2$ their inclusion improves the description of the first sharp diffraction peak [7]. In the next sections we give the explicit form of the interactions for the glasses studied in this work.

1.1.1   Interaction potential for v-SiO_2 and v-GeO_2

For v-SiO_2 we made use of the interaction potential introduced in Ref. [8]. This potential is of the form:

$$\phi_{IJ} = \frac{q_I q_J}{R_{IJ}} + A_{IJ}e^{-b_{IJ}R_{IJ}} - \frac{c_{IJ}}{R_{IJ}^6},$$ (1.3)

where $R_{IJ} = |\mathbf{R}_I - \mathbf{R}_J|$ and where ϕ_{IJ} is the interaction energy of atoms I and J, which consists of a Coulomb term, a covalent short-range contribution, and a van der Waals-like term. The Coulomb forces are described by a single free parameter, the effective silicon charge q_{Si}. The oxygen charge is fixed by the condition of charge neutrality: $q_O = -\frac{1}{2}q_{Si}$. Interactions are restricted to short-range and only two types are considered. The first type, Si-O, describes the silica bond and the second type, the nonbonded O-O interaction, ensures a tetrahedral arrangement of oxygen atoms around the silicon atom. The interaction potential defined in Eq. (1.3) has been widely used to simulate both crystalline and amorphous silica, and it has been proved to give a good description of the structure of v-SiO_2 [40, 53].

For v-GeO_2 we first considered the potential developed by Elliott, which has been tested for the α-quartz form of GeO_2 [49]. All the models we generated by using this potential within our classical molecular dynamics setup presented unrealistic features like edge-sharing tetrahedra or threefold coordinated Ge atoms. We, then, preferred to generate v-GeO_2 model structures by starting with classical dynamics of v-SiO_2. We could force the intertetrahedral angle to take values close to the average Ge-O-Ge angle in v-GeO_2,

Table 1.1: Parameters of the effective potential for SiO_2 taken from Ref. [8].

$I - J$	A_{IJ} (eV)	b_{IJ} (Å^{-1})	c_{IJ} (eVÅ^6)	
O-O	1388.7730	2.76000	175.0000	$q_O = -1.2$
Si-O	18003.7572	4.87318	133.5381	$q_{Si} = 2.4$

through a three-body term of the form:

$$\psi_{IJK} = B_{IJK} f(R_{IJ}, R_{IK})(\cos\theta_{IJK} - \cos\bar{\theta}_{IJK})^2 \qquad (1.4)$$

$$f(R_{IJ}, R_{IK}) = \begin{cases} \exp\left\{\frac{1}{R_{IJ}-R_0} + \frac{1}{R_{IK}-R_0}\right\} & \text{for } R_{IJ}, R_{IK} < R_0 \\ 0 & \text{for } R_{IJ}, R_{IK} > R_0, \end{cases} \qquad (1.5)$$

where θ_{IJK} indicates the angle subtended by $\mathbf{R}_{JI}$ and $\mathbf{R}_{IK}$. This three-body term drives the system to relax bond angles, as much as it is possible, towards the chosen target angle $\bar{\theta}_{IJK}$. In the function f in Eq. (1.5), R_0 is a cutoff distance beyond which the interactions are set to zero. B_{IJK} are the strengths of the three-body interactions. For the full set of parameters, we refer to [54]. After the generation of models of v-SiO$_2$ by means of the interaction potential [8] and the three-body term given in Eq. (1.4), we obtained structures of v-GeO$_2$ by replacing Si atoms with Ge atoms and by performing a damped first-principles molecular dynamics.

1.1.2   Interaction potential for v-GeSe$_2$

In the effective potential that we have used in our classical molecular dynamics simulation, Ge and Se are treated as ions having effective charges of $+4Z$ and $-2Z$, respectively. These charges give rise to a Coulomb interaction. The interaction potential also includes a charge-dipole and a steric repulsion between Ge and Se ions. The two-body interparticle potential is of the form:

$$\phi_{IJ} = \frac{Z_I Z_J}{R_{IJ}} - \frac{\frac{1}{2}(\alpha_I Z_J^2 + \alpha_J Z_I^2)}{R_{IJ}^4} e^{-R_{IJ}/r_{4s}} + A_{IJ} \left[\frac{\sigma_I + \sigma_J}{R_{IJ}}\right]^{\eta_{IJ}} \qquad (1.6)$$

where Z_I, σ_I, and α_I denote the effective charge, the radius and the polarizability of the Ith ion, and r_{4s} is a radial cutoff. In Table 1.2 we report the values of the parameters of the effective potential for GeSe$_2$ [Eq. (1.6)] taken from Ref. [7]. The polarizability of the Ge^{4+} ion, α_{Ge}^{4+}, is neglected, in first approximation, because the size of Ge^{4+} is considerably smaller than that of Se^{2-}. The A_{IJ}, also as a first approximation, have been considered to

Table 1.2:   Parameters of the effective potential for GeSe$_2$ taken from Ref. [7].

Z	$Z_{Se^{2+}}$	$Z_{Ge^{4+}}$	$\alpha_{Ge^{4+}}$	$\alpha_{Se^{2-}}$	r_{4s}
0.33$|e|$	-0.66$|e|$	1.32$|e|$	0	7.0 Å^3	4.43 Å

A	$\sigma_{Ge^{4+}}$	$\sigma_{Se^{2-}}$	η_{GeGe}	η_{GeSe}	η_{SeSe}
249.7 meV	0.73 Å	2.00 Å	11	9	7

be independent from the interaction I–J and are set to a common value A. Different exponents η_{IJ} are chosen for the interactions Ge-Ge, Ge-Se, and Se-Se according to an optimum criterion [7, 55]. The neutron structure factors of glassy and molten $GeSe_2$ calculated for a molecular dynamics run performed with the two-body potential in Eq. (1.6) are in good agreement with experiment. The full interaction potential we have used for v-$GeSe_2$ also includes a three-body term of the type shown in Eq. (1.4), the effect of which is to slightly improve the agreement with experiment for the first sharp diffraction peak in the neutron structure factor [7].

1.2   First-principles molecular dynamics

In this section, we briefly summarize the main ideas of first-principles molecular dynamics. For a review of the first-principles methods and of the Car-Parrinello method we refer to Refs. [56] and [57]. First-principles molecular dynamics is based on two fundamental assumptions. The first one states that the positions and momenta of the nuclei evolve in time according to Newton's equations of motion [Eq. (1.1)]. The second assumption claims that forces on the nuclei at any instant of time are those produced by the electron system in its ground state, calculated as if the nuclei were completely static at their current instantaneous positions. The first assumption is accurate provided the temperature of the system is well above the Debye temperature, which is usually the case for problems concerning glasses in ambient conditions. The second assumption concerning the forces is the Born-Oppenheimer approximation, which says that the electrons follow the motions of the nuclei adiabatically. This assumption is justified when the frequencies of the nuclear motions (typically $\sim 10^{13}$ Hz) are much lower than those of electronic excitations (typically $\sim 10^{15}$ Hz). In these conditions, the nuclear motions do not significantly excite the electronic system, which can therefore be considered in its ground state.

1.2.1   First-principles molecular dynamics in a finite electric field

In Ref. [47] a variational energy functional was introduced in order to describe the metastable state induced by the presence of a finite electric field $\mathcal{E}$ for a system obeying periodic boundary conditions. When the field $\mathcal{E}$ is directed along x, this energy functional can be written as:

$$E^{\mathcal{E}}[\{\psi_i\}] = E^{(0)}[\{\psi_i\}] - \mathcal{E} \cdot V \cdot P[\{\psi_i\}], \tag{1.7}$$

where V is the volume of the unit cell. In the following, for simplicity, we restrict the discussion of the method to cubic unit cells. In Eq. (1.7), $E^{(0)}[\{\psi_i\}]$ is the energy functional in the absence of an electric field and $P[\{\psi_i\}]$ the polarization along the direction of $\mathcal{E}$, as

defined by Resta [58]:

$$P[\{\psi_i\}] = -\frac{1}{V}\frac{L}{\pi}\operatorname{Im}\Big(\ln\det Q[\{\psi_i\}]\Big), \tag{1.8}$$

where L is the periodicity of the cell and $Q[\{\psi_i\}]$ a matrix calculated for the set of doubly occupied wave functions $\{\psi_i\}$:

$$Q_{ij} = \langle\psi_i|e^{2\pi i x/L}|\psi_j\rangle. \tag{1.9}$$

The evolution of the ionic and electronic degrees of freedom in the presence of an electric field is then performed through a Car-Parrinello molecular dynamics [56], described by the following Lagrangian:

$$\mathcal{L} = \mu\sum_i\int d\mathbf{r}\left|\frac{d\psi_i(\mathbf{r})}{dt}\right|^2 + \frac{1}{2}\sum_I M_I\left(\frac{d\mathbf{R}_I}{dt}\right)^2 - E^{\mathcal{E}}[\{\psi_i\}] + \mathcal{E}\cdot P_{\text{ion}}, \tag{1.10}$$

where μ is the fictitious electron mass, $\mathbf{R}_I$ and M_I are the position and the mass of the Ith ion, respectively, and P_{ion} is the ionic polarization defined as:

$$P_{\text{ion}} = \sum_{I=1}^{N_{\text{ion}}} Z_I\cdot(\mathbf{R}_I\cdot\hat{\mathbf{x}}), \tag{1.11}$$

where Z_I is the core charge of the Ith ion and where $\hat{\mathbf{x}}$ is a unitary vector along the direction of the electric field. Consistently with the definition of the polarization [Eq. (1.8)], the wave functions ψ_i are taken at the Γ point of the Brillouin zone.

From the Lagrangian in Eq. (1.10) one can derive the following Euler-Lagrange equations of motion describing the evolution of the electronic and ionic degrees of freedom:

$$\mu\frac{d^2\psi_i}{dt^2} = -\frac{\delta E^{(0)}}{\delta\psi_i^*} + \mathcal{E}\cdot\frac{L}{\pi}\operatorname{Im}\sum_j(Q^{-1})_{ij}\psi_j + \sum_j\Lambda_{ij}\psi_j \tag{1.12}$$

$$M_I\frac{d^2\mathbf{R}_I}{dt^2} = -\frac{\partial E^{(0)}}{\partial\mathbf{R}_I} + \mathcal{E}Z_I\hat{\mathbf{x}}, \tag{1.13}$$

where Λ_{ij} are the Lagrange multipliers used to ensure the orthonormality constraints of the electron wave functions:

$$\langle\psi_i|\psi_j\rangle = \delta_{ij}, \tag{1.14}$$

and where the following relation is used to derive Eq. (1.12):

$$d(\ln\det Q) = \sum_{ij}(Q^{-1})_{ij}dQ_{ji}. \tag{1.15}$$

The additional computational cost of this finite electric field scheme with respect to a conventional Car-Parrinello scheme mainly stems from the inversion of the matrix Q defined in Eq. (1.9).

The range of values of electric field that can be applied, is limited by a critical field, approximatively equal to $\sim E_{\mathrm{gap}}/L$, where E_{gap} is the electronic band gap of the investigated material. For values beyond this critical field, an instability occurs such that the energy functional given in Eq. (1.7) can not be minimized [47, 37].

1.3 Conclusions

In this chapter, we briefly outlined the methods used throughout this thesis for the study of the glasses v-SiO$_2$, v-GeO$_2$, and v-GeSe$_2$. The first step of our investigation is the generation of model structures by means of classical molecular dynamics simulation. The second step is represented by a first-principle investigation of the vibrational properties of a selected set of models. This step includes the calculation of coupling matrix elements required for the infrared and Raman spectra. To do this, we take advantage of a finite electric field scheme recently developed within the framework of density functional calculations subject to periodic boundary conditions. As a reference example, we apply this procedure to the case of v-SiO$_2$ in the next chapter.

Chapter 2

Vibrational spectra of v-SiO$_2$

In this chapter, we address the vibrational spectra of vitreous silica within a density functional framework. We extend previously published results for vitreous silica by comparing different model structures, one of which generated in this work, and by showing the effect of their differences in the vibrational spectra. At the same time, we here provide the reader with the definitions and the theoretical background that is used in the next chapters.

We start our investigation by analyzing the structural properties of the model structure generated in this work and by comparing them with those of models previously studied in Refs. [59, 48]. In real space, we give the bond-length, bond-angle distributions, pair correlation functions of all the models. In reciprocal space, we compare the calculated neutron and x-ray structure factors to corresponding experimental data. We also give, for future reference, the partial structure factors both in the Faber-Ziman and Bhatia-Thornthon formulations. Moreover, we investigate the origin of the first sharp diffraction peak (FSDP) by carrying out a decomposition in terms of intra- and intertetrahedral terms. Next, we address the vibrational properties. The vibrational eigenmodes are not only analyzed in terms of silicon and oxygen weights but also in terms of stretching, bending and rocking motions [60]. We then turn to the dielectric properties. We present the real and imaginary parts of the dielectric function and we compare them to experimental results. For the imaginary part, we give a comparison between the models and we discuss the relation with medium-range properties. We also calculate dielectric constants. Furthermore, we address the dynamical Born charges, the relevant coupling factors in the infrared spectra, and show for all the models, a clear relation between the oxygen dynamical Born charges and the local structural environment. Our study devotes particular attention to the Raman spectra, because of their sensitivity to medium-range structural properties. Our analysis clearly illustrates the dependence of the Raman spectra on the intertetrahedral angle. In particular, the assignment of the D_1 and D_2 peaks to four- and three-membered

rings is here further supported through projections on ring vibrations. In the final part of our study, we focus on the Raman coupling factors and derive therefrom optimal bond-polarizability parameters.

This chapter is organized as follows. In Sec. 2.1, we outline the generation procedures that gave rise to the model structures of v-SiO$_2$ used in this work. Next, we address the structural properties of v-SiO$_2$ in real space (Sec. 2.2) and reciprocal space (Sec. 2.3), focusing on the largest of these model structures. Sections 2.4, 2.4.1 are devoted to vibrational modes, and in particular we present our analyses of the vibrational density of states. Section 2.5 is dedicated to the dynamic structure factor and to the inelastic neutron spectrum. Section 2.6 contains the infrared properties, including the dielectric function, the static dielectric constant, and the dynamical Born charges. Section 2.7 addresses the Raman spectra. In particular, we focus on the relation between the Raman spectra and the intertetrahedral angle distribution, on the origin of the features D_1 and D_2, and on the derivation of optimal bond polarizability parameters. The conclusions of this chapter are given in Section 2.8.

2.1   Models of vitreous silica

The use of multiple models constitutes a way to achieve a good level of statistical representation of structural features in v-SiO$_2$ [61]. Thus for discussing the structural and vibrational properties of v-SiO$_2$ we consider a set of three models (Models I, II, and III). Models I and II were generated by a combined use of classical and first-principles molecular dynamics [52, 48], whereas Model III was obtained within a fully first-principles scheme [59]. The combined use of classical and first-principles molecular dynamics, in the case of vitreous silica and germania, allows one to quickly obtain model structures with structural and vibrational properties of comparable quality with respect to those structures generated within a fully first-principles scheme [62, 37].

As a starting point for the generation of Model I, we selected a model structure of v-SiO$_2$ among those previously generated in Ref. [52] by classical molecular dynamics [8, 40]. We then performed a structural optimization of this model through damped first-principle molecular dynamics [56, 63]. Model I was generated at the experimental density of 2.2 g/cm^3, with a double size (144 atoms) with respect to Models II and III, with a Si-O-Si angle distribution in better agreement with experiment (Tab. 2.1), and with a low content of three-membered rings (cf. Sec. 2.2.2).

In this chapter, we performed electronic and structural relaxations using first principles methodologies [56, 63], as provided in the QUANTUM-ESPRESSO package [64]. The exchange and correlation energy was accounted for through local density approximation
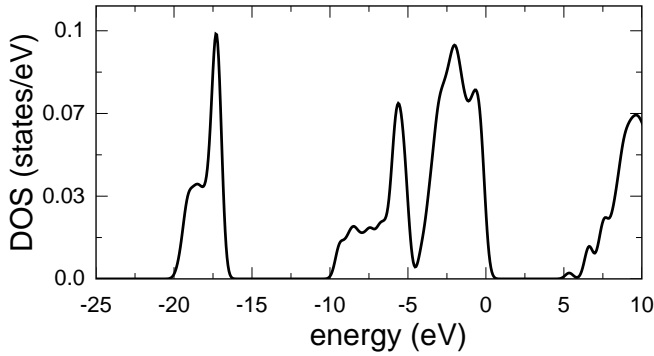
Figure 2.1: Electronic density of states (DOS) for Model I of v-SiO$_2$. The highest occupied states are aligned at 0 eV. A Gaussian broadening of 0.25 eV is used.

(LDA) to density functional theory. Plane wave basis sets with energy cutoffs of 25 Ry and 200 Ry were used to expand the electron wave functions and the electron density, respectively. Core valence interactions were accounted for by a normconserving pseudopotential for Si (Ref. [65]) and an ultrasoft one for O [66]. The wave functions were expanded at the sole Γ point of the Brillouin zone, as justified by the large size and the large band gap of our systems.

The electronic density of states of Model I is presented in Fig. 2.1. The origin of the bands in terms of atomic orbitals is similar to the case of α-quartz SiO$_2$ [67]: the lowest band arises from O-2s states, the low-energy side of the central band results from the bonds between Si-sp^3 and O-2p orbitals. The high-energy side of this central band consists of O-2p nonbonding orbitals, which define the top of the valence band. The low-energy part of the conduction band mainly consists of Si orbitals with antibonding character [67]. The calculated band gap (5.3 eV) significantly underestimates the experimental value ($\sim$ 9 eV, Ref. [68]), as usual in density functional schemes. The present electronic density of states is consistent with previous calculations for α-quartz SiO$_2$ and v-SiO$_2$ [67, 59].

2.2 Real-space properties

For the structural properties, we here analyse in a more detailed manner, the model generated in this work, i.e Model I, and keep the other two models for comparisons that can be helpful in understanding the improvements achieved by Model I. In Fig. 2.2(a) we show the bond-length distributions of our models. All three models show very similar average bond lengths ($\sim$ 1.6 Å) in good agreement with experimental estimates [14]. The bond-length distribution of Model I looks more Gaussian than those of Models II and III, as a consequence of the larger size and therefore of the larger statistics of bonds. The spread of the bond-length distribution is smaller for Model III, that was generated through a fully *ab initio* procedure [59], indicating that its structure has undergone a better relaxation. In

Table 2.1: Structural properties of Models I, II, and III of vitreous SiO$_2$: the number of atoms (N), the average Si-O-Si angle, the average O-Si-O angle, and the average bond length (d_{SiO}). The respective standard deviations are given in parentheses. Experimental estimates for the angles and the bond lengths are taken from Ref. [14].

	N	d_{SiO} (Å)	$\angle$ O-Si-O	$\angle$ Si-O-Si
Model I	144	1.600 (0.015)	109.4° (4.3°)	148.2° (13.4°)
Model II	72	1.614 (0.020)	109.5° (6.4°)	152.6° (10.9°)
Model III	72	1.594 (0.014)	109.5° (5.3°)	136.9° (14.2°)
Expt.		1.605	109.47°	148.3°

Fig. 2.2(b), we show the O-Si-O angle distribution for our models. In all the models, the O-Si-O angle is very close to the value corresponding to the ideal tetrahedral geometry and to the experimental estimate (109.47°) [14]. The width of the distribution of Model II is slightly larger than in the other two models, witnessing some residual strain in the tetrahedra. In Fig. 2.2(c), we show the Si-O-Si bond-angle distributions of Models I, II and III. Models I and II are characterized by similar distributions. The average values of the Si-O-Si bond-angle distributions are reported in Table 2.1. The lowest average value is found for Model III. The Si-O-Si bond-angle distribution in Model III peaks at $\sim 130°$ that is typical for three-membered rings (see Sec. 2.2.2). The Si-O-Si bond-angle is a key parameter for the description of a network of corner-sharing tetrahedra. Indeed its distribution gives information on the medium-range order of the network, since it is related to the way the tetrahedra are arranged.
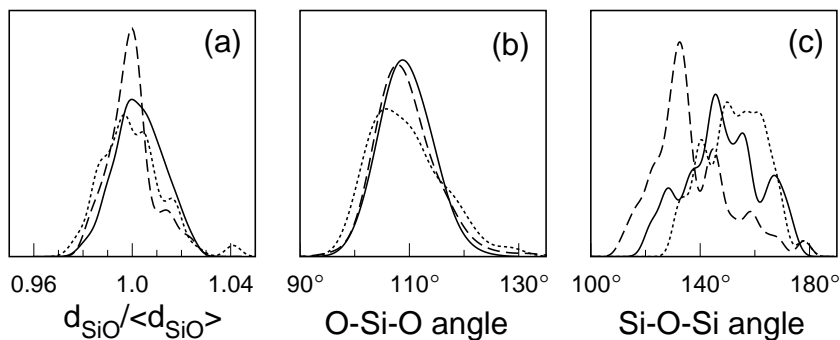

Figure 2.2: (a) Bond-length Si-O, (b) O-Si-O angle and (c) Si-O-Si bond-angle distributions of Model I (solid), II (dotted) and III (dashed) of vitreous silica. Gaussian broadenings of 0.005 Å and 2.5° are used.

2.2.1 Pair correlation functions

In a binary system, the partial pair correlation function $g_{\alpha\beta}(r)$ gives the ratio between the density of atoms of species β at a distance r from an atom of species α and the average density ρ_β of atoms of species β [69]:

$$g_{\alpha\beta}(r) = \frac{1}{N_\alpha \rho_\beta} \sum_{\alpha,\beta} \delta(r - |\mathbf{R}_{\alpha J} - \mathbf{R}_{\beta I}|), \tag{2.1}$$

where N_α corresponds to the number of atoms of species α.

We calculate partial pair correlation functions in the harmonic approximation using the vibrational eigenmodes $\boldsymbol{\xi}^n$ and frequencies ω_n (cf. Sec. 2.4). At 300 K, this has been found to be a good approximation for oxide glasses [70, 71]. With respect to the alternative approach based on averaging over molecular dynamics trajectories in which the ionic motion is treated classically, this formulation offers the advantage of including the zero-point motion in the description [70, 71].

In our calculation, we replace the δ functions in Eq. (2.1) with Gaussian functions with a variance σ^2 given by [70]

$$\sigma^2 = \langle (\mathbf{d} \cdot (\mathbf{u}_{\beta I} - \mathbf{u}_{\alpha J}))^2 \rangle, \tag{2.2}$$

where $\mathbf{u}_I$ is the displacement of the Ith atom with respect to the equilibrium position $\mathbf{R}_I$, and $\mathbf{d}$ is a unitary vector along the direction of $\mathbf{R}_{\alpha J} - \mathbf{R}_{\beta I}$. The brackets $\langle \ldots \rangle$ indicate a thermal average obtained as follows [70]:

$$\langle u_{Ii} u_{Jj} \rangle = \sum_n \frac{\hbar}{\omega_n} \frac{\xi_{Ii}^n}{\sqrt{M_I}} \frac{\xi_{Jj}^n}{\sqrt{M_J}} \left[n_{\mathrm{B}}(\hbar\omega_n) + \frac{1}{2} \right] \tag{2.3}$$

where the indices i and j label the Cartesian directions, M_I corresponds to the mass of the Ith atom, and the temperature dependence enters through the Boson occupation number $n_{\mathrm{B}}(E) = [\exp E/k_{\mathrm{B}}T - 1]^{-1}$, where k_{B} is the Boltzmann factor. In Fig. 2.3, we give the pair-correlation functions, $g_{\mathrm{SiO}}(r)$, $g_{\mathrm{SiSi}}(r)$, and $g_{\mathrm{OO}}(r)$, corresponding to Model I, calculated at room temperature. The first peak of $g_{\mathrm{SiO}}(r)$ is located at 1.59 Å and agrees closely with the Si-O bond length (Table 2.1). From a spherical integration of the first peak in $g_{\mathrm{SiO}}(r)$ we derive an average coordination number of 4.0. Similarly the spherical integration of the first peaks in $g_{\mathrm{SiSi}}(r)$ and $g_{\mathrm{OO}}(r)$ yelds values of 4.0 and 6.3, respectively. These values for the average coordination numbers are clearly a consequence of the existence of the tetrahedral unit SiO_4 and of the fact that the network is composed of cornersharing tetrahedra, so that on average each Si is surrounded by the four Si atoms of the nearest-neighbor tetrahedra. The first peaks of $g_{\mathrm{SiSi}}(r)$ and $g_{\mathrm{OO}}(r)$ correspond to Si-Si and O-O distances of 3.08 Å and 2.59 Å, respectively. In Fig. 2.4 we show the comparison between the Si-Si pair-correlation functions calculated at room temperature for our models. The first peak position varies according to the Si-O-Si angle distribution [Fig. 2.2(c)].
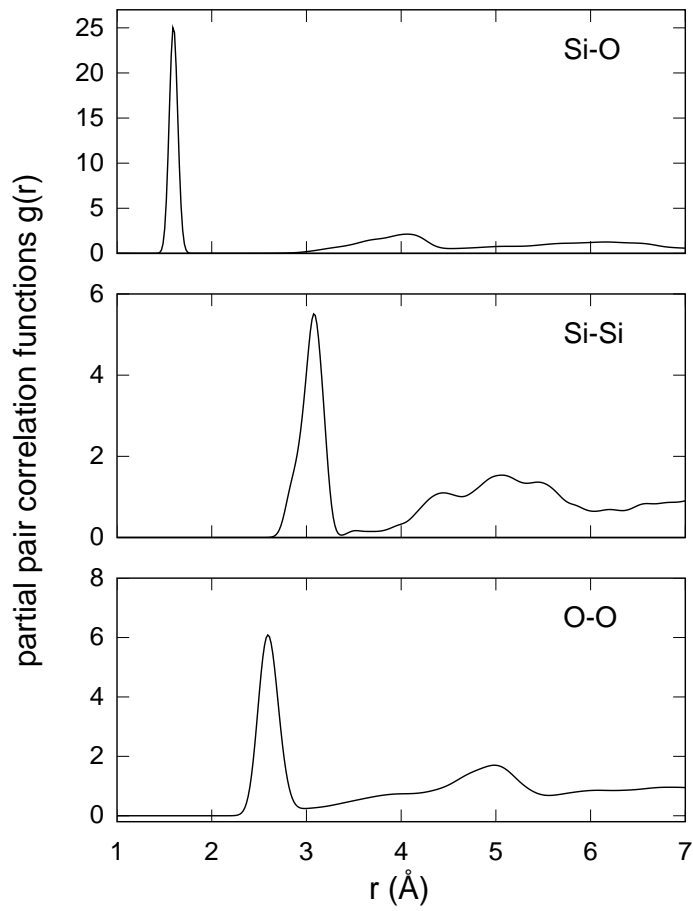
Figure 2.3: Pair-correlation functions $g_{\mathrm{SiO}}(r)$, $g_{\mathrm{SiSi}}(r)$, and $g_{\mathrm{OO}}(r)$ calculated in the harmonic approximation for Model I of v-SiO$_2$ at room temperature.

2.2.2   Ring statistics in XO$_2$ glasses

Vitreous SiO$_2$ and GeO$_2$ can be thought as random networks where the basic topological units are the XO$_4$ (X=Ge,Si) tetrahedra [24]. These units are connected to form ring-like
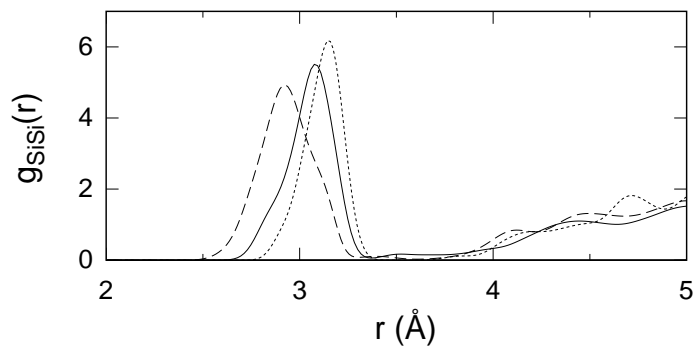

Figure 2.4: $g_{\mathrm{SiSi}}(r)$ calculated in the harmonic approximation for Model I (solid), Model II (dotted), and Model III (dashed).

structures that give rise to the network. Therefore, one practical way to characterize the connectivity of the network, a medium-range order property, is that of looking at the *ring statistics* [15]. The ring statistics are obtained by taking every pair of vertices on each topological unit in turn and then finding the smallest sized ring, expressed as a number of topological units, in which they are both contained. In this way, we can find the average number of m-membered rings $M(m)$ per topological unit. Given a topological unit with n connections the total number of rings per topological unit is well defined $N_u = n(n-1)/2$. Clearly, the number of $m-$membered rings per topological unit, $M(m)$, must fullfill to the following relation:

$$\sum_m M(m) = N_u. \tag{2.4}$$

In the case of XO_4 tetrahedra $N_u = 6$, therefore there are six rings passing through each topological unit in the network. Since for each $m-$membered ring the intertetrahedral bond-angle has an average that depends on the order m, the ring statistics are related to the X-O-X angle distribution. In particular the presence of many three-membered rings can lower remarkably the average intertetrahedral angle.

The ring statistics of our three models of v-SiO_2 are shown in Fig. 2.5. For all the models, five- and six-membered rings are the most frequent. The fact that the network of vitreous silica contains a large number of six-membered rings can be understood by considering the phase diagram of silica. At zero pressure, the crystalline phase that is obtained when the system is cooled from the liquid phase is β-cristobalite [72], which has only rings of size six. It can be expected that the local structure of the amorphous network will be similar to the crystalline network next to the liquid phase. Therefore in the amorphous phase we expect that rings of size six are among the most frequent. Figure 2.5 shows that this is indeed the case. In all our models, eight-membered and larger sized rings are rare. We register differences among the models for the small sized rings, the three- and four-membered rings, the concentration of which significantly varies among the models.

Model I shows a single three-membered ring and ten four-membered rings. The sum of bond angles inside the three-membered ring amounts to $698°$, slightly less than the ideal value of $720°$. In Model II, three-membered rings are absent, while there is a single four-membered ring. Model III shows five three-membered rings and two four-membered rings [21].

In Table 2.2 we give the concentration of O atoms belonging to three- and four-membered rings in our models of v-SiO_2 and theoretical estimates from Ref. [4]. The concentration of O in three-membered rings is close to the theoretical estimate only in Model II, while in Models I and II it is from ten to hundred times larger. All our models, then show concen-
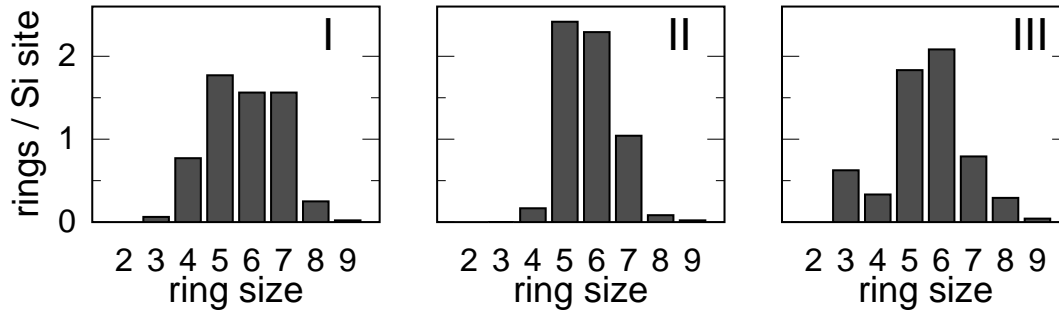
Figure 2.5: Ring statistics of Models I, II and III of vitreous silica.

tration values of O in four-membered rings from twenty to hundred times larger than the theoretical estimate. We remark here that for the scope of our study of v-SiO$_2$ (and also for the other glasses we consider in this thesis) we are interested in models substantially differing in their ring statistics, so that we can learn how the differences are reflected in the structural and vibrational properties. Finally, a model containing $\sim$1000 atoms would be necessary to approach the theoretical estimate of O in three-membered rings, but the computational cost of *ab initio* calculations would be excessively high.

Table 2.2: Concentration of O atoms belonging to three- and four-membered rings in our models of v-SiO$_2$ and theoretical estimates from Ref. [4].

	Model I	Model II	Model III	Theory Ref. [4]
O$_{3R}$	3%	0%	31%	0.22%
O$_{4R}$	42%	8.3%	17%	0.36%

2.3   Reciprocal-space properties

To avoid Fourier transformations, direct comparisons between diffraction data and model structures are preferably performed in reciprocal space. Following Waseda [69], we express the total structure factor as a function of the exchanged momentum Q:

$$S(Q) = \sum_{\alpha,\beta} (c_\alpha c_\beta)^{1/2} \frac{f_\alpha(Q) f_\beta(Q)}{\langle f^2(Q) \rangle} S_{\alpha\beta}(Q), \tag{2.5}$$

$$\langle f^2(Q) \rangle = \sum_{\alpha} c_\alpha f_\alpha^2(Q), \tag{2.6}$$

where $c_\alpha = N_\alpha/N$ and f_α are atomic scattering factors and $S_{\alpha\beta}(Q)$ are the partial structure factors in the Ashcroft-Langreth formulation:

$$S_{\alpha\beta}(Q) = \frac{1}{\sqrt{N_\alpha N_\beta}} \left\{ \langle \sum_{J=1}^{N_\alpha} \sum_{K=1}^{N_\beta} e^{-i\mathbf{Q}\cdot(\mathbf{R}_{\alpha J} - \mathbf{R}_{\beta K})} \rangle - \delta_{\mathbf{Q},0} \right\}. \tag{2.7}$$

where the brackets $\langle \ldots \rangle$ indicate a thermal average. For isotropic materials, the structure factors only depend on the modulus of $\mathbf{Q}$, and are obtained by a spherical average [73].

Adopting the harmonic approximation, the thermal average can be calculated by means of Eq. (2.3). The partial structure factors then simplify to

$$S_{\alpha\beta}(Q) = \frac{1}{\sqrt{N_\alpha N_\beta}} \left\{ \sum_{JK} e^{-W_{JK}(\mathbf{Q})} e^{i\mathbf{Q}\cdot(\mathbf{R}_{\alpha J} - \mathbf{R}_{\beta K})} - \delta_{\mathbf{Q},0} \right\}, \tag{2.8}$$

where the exponents in the Debye-Waller factors are given by

$$W_{JK}(Q) = \frac{1}{2} \langle \{\mathbf{Q} \cdot (\mathbf{u}_J - \mathbf{u}_K)\}^2 \rangle. \tag{2.9}$$

In neutron diffraction, the interactions between the incoming neutrons and the nuclei are described by the neutron scattering lengths b_α: $f_\alpha(Q) = b_\alpha$. In our calculations, we took the neutron scattering lengths $b_{\text{Si}} = 4.149$ fm and $b_{\text{O}} = 5.805$ fm [74]. The calculation of $S(Q)$ corresponds to the average over a discrete set of $\mathbf{Q}$ vectors of modulus Q. Only $\mathbf{Q}$ vectors compatible with the periodicity of the simulation cell are retained. Therefore, the result corresponds to the infinitely repeated model [27].

We show in Fig. 2.6(a) the comparison between the neutron structure factors of Model I and the experimental data taken from Ref. [75]. An overall good agreement is registered with the experiment. The other two models show comparisons with experiment of similar quality [59, 48].

Following Waseda [69], the x-ray structure factor is also given by Eq. (2.5), where the $f_\alpha(Q)$ now stand for the atomic x-ray scattering factors [76]. Figure 2.6(b) shows the comparison between the x-ray structure factors of Model I and the experimental data taken from Ref. [77]. The agreement with experimental data is of similar quality to that registered for the neutron structure factor [Fig. 2.6(a)]. In the range of $Q \leq 5$ Å^{-1}, the x-ray structure factor differs markedly with respect to the neutron structure factor. In particular, in the x-ray structure factor the FSDP shows an increased intensity, and no feature is registered corresponding to the second peak in the neutron structure factor (~ 2.7 Å^{-1}). This can be understood by means of the partial structure factors (See 2.3.1): the linear combination of them that is used to calculate the x-ray structure factor is such that the peak at ~ 2.7 Å^{-1} almost disappears.
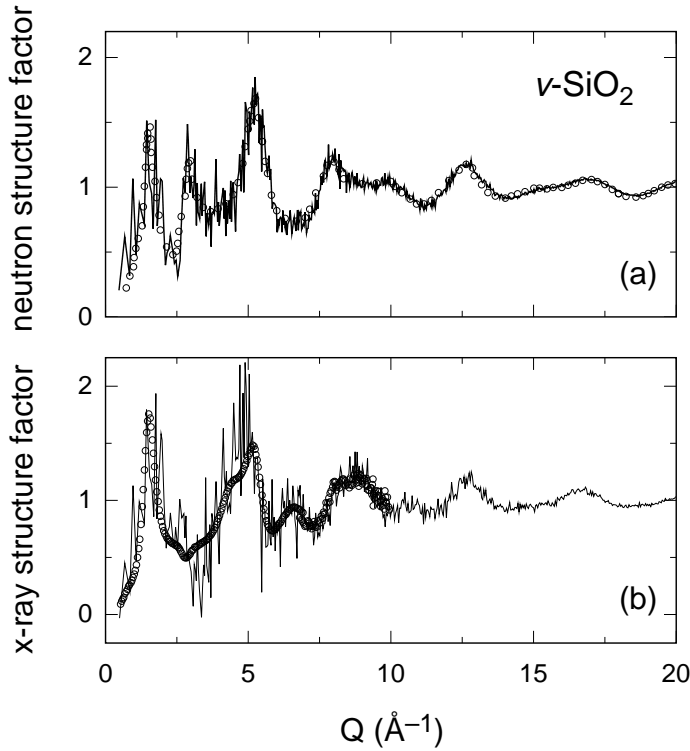
Figure 2.6:   (a) Calculated total neutron structure factor (solid) for Model I of v-SiO$_2$ at room temperature, compared with its experimental counterpart (circles) [75]; (b) Calculated x-ray structure factor at room temperature (solid) for Model I of v-SiO$_2$, compared with its experimental counterpart (circles) [77].

2.3.1 Partial structure factors

The partial structure factors of vitreous silica have so far not been obtained experimentally. Nevertheless, for future reference we here give these functions both in the Faber-Ziman [69] and Bhatia-Thornton formulations [78]. The Faber-Ziman formulation of the partial structure factors is related to the common Ashcroft-Langreth form ($S_{\alpha\beta}(Q)$) through the following relations [69]:

$$S_{\alpha\alpha}^{\text{FZ}}(Q) \ = \ [S_{\alpha\alpha}(Q) - c_\beta]/c_\alpha \tag{2.10}$$

$$S_{\beta\beta}^{\text{FZ}}(Q) \ = \ [S_{\beta\beta}(Q) - c_\alpha]/c_\beta \tag{2.11}$$

$$S_{\alpha\beta}^{\text{FZ}}(Q) \ = \ S_{\alpha\beta}(Q)/(c_\alpha c_\beta)^{1/2} + 1, \tag{2.12}$$

where α and β indicate Si and O species, respectively. In Fig. 2.7 we show the calculated Faber-Ziman partial structure factors for Model I of v-SiO$_2$ at room temperature. The $S_{\text{SiSi}}^{\text{FZ}}(Q)$ and $S_{\text{SiO}}^{\text{FZ}}(Q)$ partial structure factors allow us to relate the origin of the FSDP in the total structure factor [Fig. 2.6] to Si-Si and Si-O correlations, but not to O-O since the $S_{\text{OO}}^{\text{FZ}}(Q)$ shows negligible weight in the FSDP region.

The partial structure factors in the formalism of Bhatia and Thornton can be obtained from $S_{\alpha\beta}(Q)$ by a linear transformation [69]:

$$S_{\text{NN}}(Q) \ = \ c_\alpha S_{\alpha\alpha}(Q) + c_\beta S_{\beta\beta}(Q) + \frac{2}{\sqrt{c_\alpha c_\beta}} S_{\alpha\beta}(Q) \tag{2.13}$$
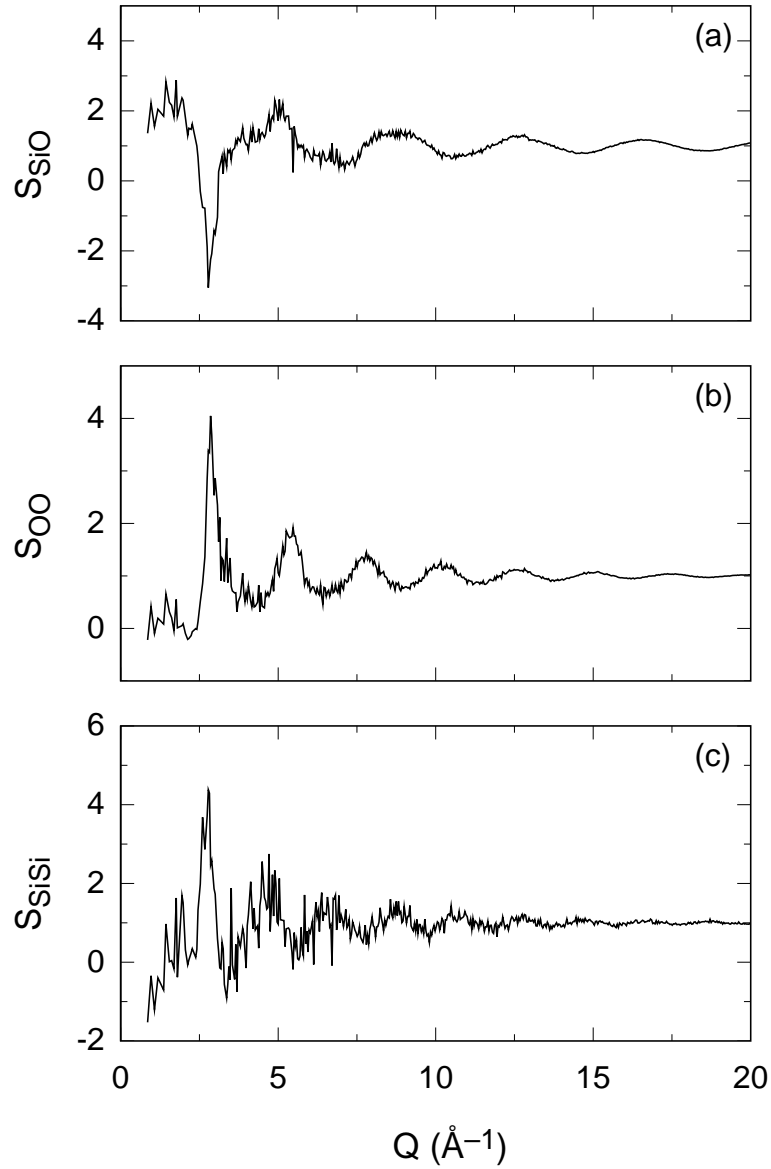
Figure 2.7: Calculated Faber-Ziman partial structure factors for Model I of v-SiO$_2$ at room temperature: (a) $S_{\text{SiO}}(Q)$, (b) $S_{\text{OO}}(Q)$, and (c) $S_{\text{SiSi}}(Q)$.

$$S_{\text{CC}}(Q) = c_\alpha c_\beta \left[c_\beta S_{\alpha\alpha} + c_\alpha S_{\beta\beta} - \frac{2}{\sqrt{c_\alpha c_\beta}} S_{\alpha\beta}(Q) \right] \tag{2.14}$$

$$S_{\text{NC}}(Q) = c_\alpha c_\beta \left[S_{\alpha\alpha} - S_{\beta\beta} + \frac{c_\beta - c_\alpha}{\sqrt{c_\alpha c_\beta}} S_{\alpha\beta}(Q) \right]. \tag{2.15}$$

In Fig. 2.8 we show the Bhatia-Thornton partial structure factors calculated for Model I. We note that the $S_{\text{NN}}(Q)$ is very similar to the neutron total structure factor. This can be understood by comparing Eq. (2.5) and Eq. (2.13) and by taking into account the fact that O and Si have quite similar scattering lengths. In the limit $Q \rightarrow \infty$, the number-number partial structure factor $S_{\text{NN}}(Q)$ tends to unity [Eq. (2.13)]. In the concentration-
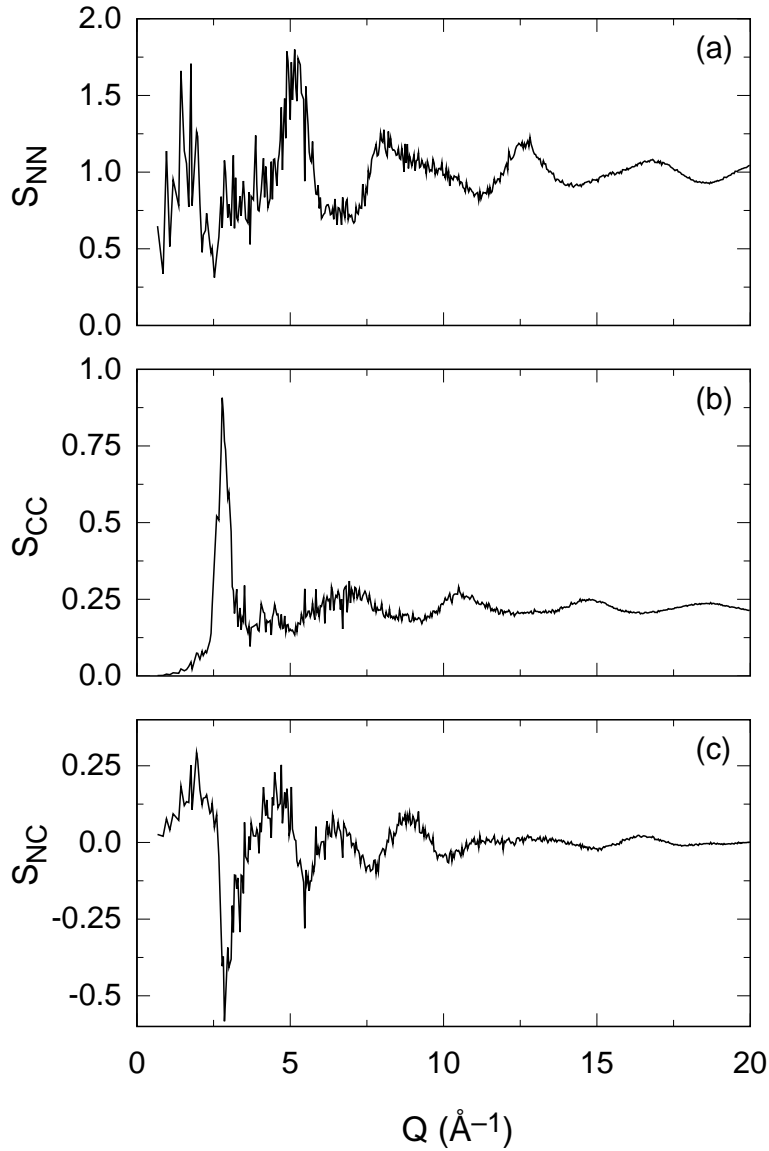
Figure 2.8: Calculated Bhatia-Thornton partial structure factors for Model I of v-SiO$_2$ at room temperature: (a) $S_{NN}(Q)$, (b) $S_{CC}(Q)$, and (c) $S_{NC}(Q)$.

concentration structure factor $S_{CC}(Q)$ the dominant peak is located at ~ 2.7 Å^{-1}. We do not register any clear trace of the FSDP, in agreement with previous calculations [59]. For large Q vectors, the $S_{CC}(Q)$ and $S_{NC}(Q)$ tend to $c_\alpha c_\beta = 2/9$ and zero, respectively [Eqs. (2.14) and (2.15)].

2.3.2   An analysis of the FSDP in vitreous silica

We hereafter present an analysis of the FSDP in terms of intratetrahedral correlations ("self-term" of the tetrahedron) and intertetrahedral correlations. The decomposition is obtained by splitting the sums over the atoms in Eq. (2.5) into two terms. The self-term includes, for each tetrahedron, only the O–O and O–Si correlations of O and Si atoms within the tetrahedron. Instead the intertetrahedral term, contains all the O–O, Si–O, Si–Si correlations of atoms belonging to distinct tetrahedra. The two terms, the intra- and the intertetrahedral term, clearly have to sum up to give back the total structure factor.

In Fig. 2.9 we show the decomposition of the neutron structure factor $S(Q)$ of Model I. The maximum in the total $S(Q)$ is located at 1.53 Å^{-1}, in close agreement with the experimental position 1.55 Å^{-1}. For $Q \geq 2.2$ Å^{-1}, the intratetrahedral term closely follows the total structure factor apart from small discrepancies that tend to disappear for increasing Q values [79]. In this range of Q vectors, the intertetrahedral term is oscillating around zero, and it vanishes as Q increases. For $Q \leq 2.2$ Å^{-1}, the intratetrahedral term decreases and presents a minimum at $Q \sim 2.0$ Å^{-1}, and then increases again for $0 < Q \leq 1.8$ Å^{-1}. The intertetrahedral term, instead, shows a maximum at ~ 1.8 Å^{-1} and decreases quickly for $0 < Q \leq 1.8$ Å^{-1}. This decomposition shows how the FSDP in silica arises from the competition of two terms one related to the basic tetrahedral unit and the other related to medium-range order as described by the intertetrahedral term [79].

In Fig. 2.10, we carry out the same decomposition into intra- and intertetrahedral correlations for the $S_{CC}(Q)$. As seen for the total $S(Q)$, the behavior for $Q \geq 3.0$ Å^{-1} is mainly given by the intratetrahedral term, while for lower Q values it is the intertetrahedral term that is dominant. Moreover, the decomposition shows that the two terms compensate for $Q \leq 2$ Å^{-1}, leaving no trace of the FSDP in the total $S_{CC}(Q)$. However, there is a clear trace of the FSDP in the $S_{CC}(Q)$ of our Model I of v-GeO$_2$ (cf. Sec. 3.2.3). This suggests
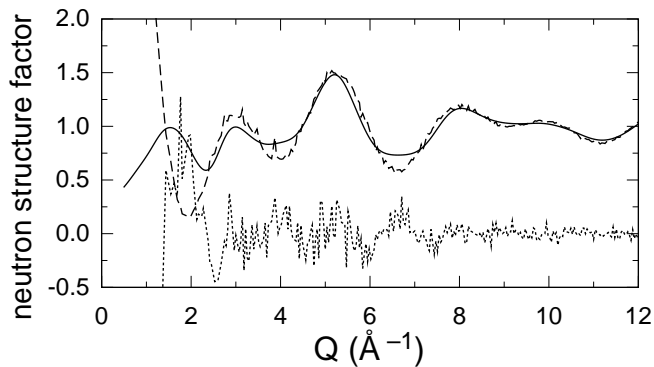

Figure 2.9: Theoretical total neutron structure factor (solid) for Model I of v-SiO$_2$ at room temperature, and its decomposition in intratetrahedral (dashed) and intertetrahedral terms (dotted line). For clarity, we applied a smoothening procedure to the total structure factor. A Gaussian broadening of 0.25 Å^{-1} was used (cf. App. A).
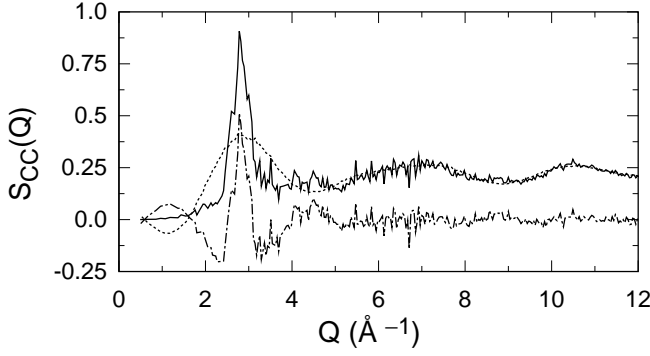
Figure 2.10: Concentration-concentration structure factor in the Bhatia-Thornthon formalism (solid) for Model I of v-SiO$_2$ at room temperature, and its decomposition into intratetrahedral (dotted line) and intertetrahedral terms (dot-dashed line).

that the absence of a FSDP in the $S_{\text{CC}}(Q)$ is not an intrinsic characteristic of chemically ordered random networks, such as vitreous silica or germania [26, 80].

2.4 Vibrational frequencies and eigenmodes

In this section, we calculate the vibrational modes of our models of vitreous silica and analyse them through the vibrational density of states. The analytical part of the dynamical matrix is expressed using a similar notation as in Ref. [81]:

$$D_{IiJj} = \frac{1}{\sqrt{M_I M_J}} \frac{\partial^2 E_{\text{tot}}}{\partial R_{Ii} \partial R_{Jj}} = -\frac{1}{\sqrt{M_I M_J}} \frac{\partial F_{Jj}}{\partial R_{Ii}}, \qquad (2.16)$$

where E_{tot} is the total energy of the system and M_I the mass of the Ith atom. Upper and lower case indices are used to indicate the atoms and the three Cartesian directions, respectively. We obtain the dynamical matrix in Eq. (2.16) by taking finite differences of the atomic forces $\mathbf{F}_J$ [35]. Atomic displacements of ± 0.1 bohr are used in these calculations. The full dynamical matrix also includes a nonanalytical matrix, $\mathcal{D}^{\mathbf{q}}_{IiJj}$, accounting for vibrational excitations longitudinal to the normalized direction $\mathbf{q}$ along which the vibrational momentum is exchanged [82]:

$$D^{\mathbf{q}}_{IiJj} = D_{IiJj} + \mathcal{D}^{\mathbf{q}}_{IiJj}, \qquad (2.17)$$

where:

$$\mathcal{D}^{\mathbf{q}}_{IiJj} = \frac{1}{\sqrt{M_I M_J}} \frac{4\pi}{\epsilon_\infty V} \left(\sum_k Z^*_{I,ki} \cdot q_k \right) \left(\sum_h Z^*_{J,hj} \cdot q_h \right), \qquad (2.18)$$

where V indicates the volume of the periodic simulation cell. In Eq. (2.18), the high-frequency dielectric tensor of our system is assumed to be isotropic [83]. The tensors $Z^*_{I,ik}$ entering in Eq. (2.18) are the Born effective charge tensors. These are defined as the induced polarization P^{el}_i along the direction i by a unitary displacement of the Ith atom in direction k [84]:

$$Z^*_{I,ik} = V \frac{\partial P^{\text{el}}_i}{\partial R_{Ik}} = -\frac{\partial^2 E_{\text{tot}}}{\partial \mathcal{E}_i \partial R_{Ik}} = \frac{\partial F_{Ik}}{\partial \mathcal{E}_i}, \qquad (2.19)$$

where the last equality gives an alternative definition of the Born effective charge tensors in terms of the atomic forces $\mathbf{F}_I$. We obtain the tensors[1] $Z^*_{I,ik}$ by taking finite differences of atomic forces $\mathbf{F}_I$ with respect to the electric field:

$$Z^*_{I,ik} = \frac{\Delta F_{Ik}}{\Delta \mathcal{E}_i}, \tag{2.20}$$

where we make use of the possibility of applying a finite electric field (Sec. 1.2.1).

For a given choice of $\mathbf{q}$, the frequencies ω_n and the corresponding normalized eigenmodes $\boldsymbol{\xi}^n_I$ are obtained by diagonalizing the dynamical matrix. The associated atomic displacements are given by:

$$\mathbf{u}^n_I = \frac{1}{\sqrt{M_I}} \boldsymbol{\xi}^n_I. \tag{2.21}$$

The index n labeling the vibrational modes runs from 1 to $3N$, where N is the total number of atoms in the model.

2.4.1 Vibrational density of states

The vibrational density of states (v-DOS) underlies all the vibrational spectra. We focus in this section on the analysis of the v-DOS in terms of the vibrational eigenmodes, before addressing the infrared and Raman spectra. The v-DOS $Z(\omega)$ is expressed as

$$Z(\omega) = \frac{1}{3N} \sum_n \delta(\omega - \omega_n), \tag{2.22}$$

in terms of the vibrational frequencies ω_n.

In Fig. 2.11(a), the v-DOS is decomposed according to the weights of the two species: $Z(\omega) = \sum_\alpha Z_\alpha(\omega)$. The partial density of states $Z_\alpha(\omega)$ is defined by:

$$Z_\alpha(\omega) = \frac{1}{3N} \sum_I^{N_\alpha} \sum_n |\boldsymbol{\xi}^n_I|^2 \delta(\omega - \omega_n) \tag{2.23}$$

$\boldsymbol{\xi}^n$ being the normalized eigenvector corresponding to the frequency ω_n. Figure 2.11(a) shows that the Si weight is dominant in the range of the peak at $\sim$800 cm^{-1}, while the O weight dominates in the low band below 500 cm^{-1} and above 1000 cm^{-1}.

We further decomposed the oxygen contribution to the v-DOS according to three orthogonal directions defining the local environment [60] of the O atoms [Fig. 2.11(b)]. The principal directions associated to the Si-O-Si bridge define the rocking, bending and stretching directions, respectively [35]. The lowest vibrational band ($\leq$ 425 cm^{-1}) prevalently features O rocking motions with a minor content of O bending motions, while the band extending from 425 to 900 cm^{-1} is mainly composed of O bending motions with a minor

---

[1]A more detailed analysis of the Born charge tensors will be given in Sec. 2.6.1.

content of O rocking motions. The decomposition in Fig. 2.11(b) shows that the vibrational modes above $\sim$900 cm^{-1} are mostly given by O stretching motions. The stretching contribution features a double peak [Fig. 2.13(a)] in the inelastic neutron spectrum [85]. To address this splitting, it is convenient to organize the stretching modes according to the irreducible representations of the tetrahedron A_1 and T_2 [35]. The A_1 mode corresponds to an in-phase motion of the four O atoms towards the central Si atom. In the T_2 modes, two O atoms move closer to the central Si atom, while the other two move away. By projecting on A_1 and T_2 representations, it was shown for Model III that this doublet stems from these distinct vibrational modes of the tetrahedra and that it should not be assigned to a longitudinal-optic/transverse-optic (LO-TO) effect [35]. In the inset of Fig. 2.11(b), we show the v-DOS of Model I after projection on the A_1 and T_2 representations. These two representations give rise to different peaks located at $\sim$1100 cm^{-1} and $\sim$1210 cm^{-1} corresponding to the experimental doublet.
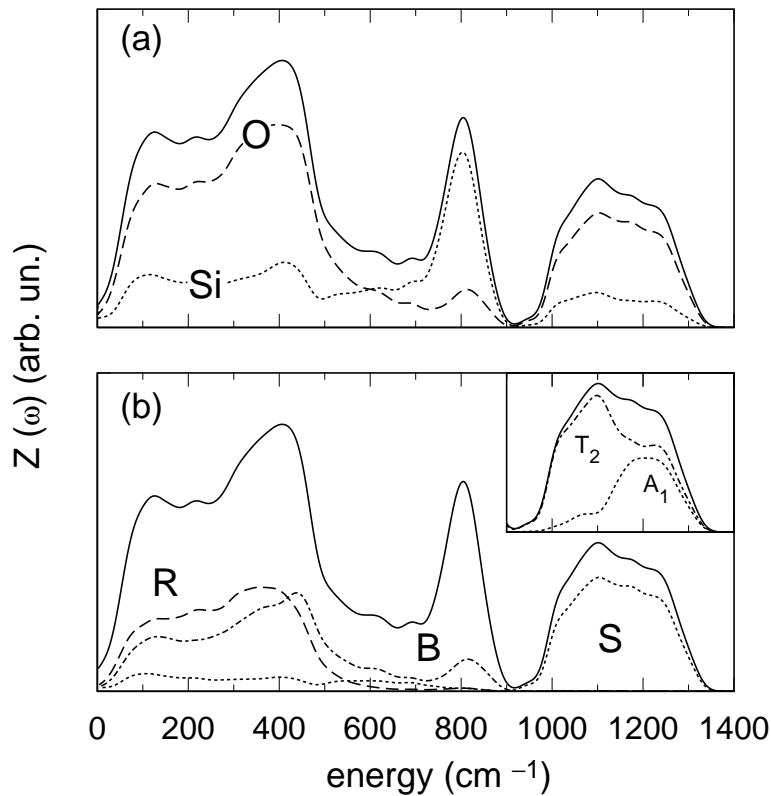

Figure 2.11: Vibrational density of states $Z(\omega)$ of Model I (solid) and its decompositions. In (a), $Z(\omega)$ is first decomposed into O and Si weights. In (b), the O weight is further decomposed according to the O motion along the rocking (R, dashed), bending (B, dot-dashed) and stretching (S, dotted) directions. Inset: Projection on symmetry-adapted modes of the SiO$_4$ tetrahedra: T$_2$ (dashed) and A$_1$ (dotted). A Gaussian broadening of 19 cm^{-1} is used.

2.5 Dynamic structure factor and inelastic neutron scattering spectrum

Since Si and O have negligible incoherent scattering cross sections, the one-phonon neutron-scattering function is given by [74, 86]:

$$S(\mathbf{Q}, E) = \frac{1}{N\langle b^2 \rangle} \sum_{II'} b_I b_{I'} e^{-(W_I + W_{I'})} e^{i\mathbf{Q} \cdot (\mathbf{R}_{I'} - \mathbf{R}_I)} \tag{2.24}$$

$$\times \sum_n \hbar \frac{(\mathbf{Q} \cdot \mathbf{e}_I^n)(\mathbf{Q} \cdot \mathbf{e}_{I'}^n)}{2(M_I M_{I'})^{1/2} \omega_n} [n(\hbar\omega_n) + 1] \, \delta(E - \hbar\omega_n). \tag{2.25}$$

where the W_I are the exponent of the Debye-Waller factors which for an isotropic amorphous system are given by

$$W_I(Q) = Q^2 \langle \mathbf{u}_I^2 \rangle / 6. \tag{2.26}$$

In Fig. 2.12, we carry out a comparison between the experimental inelastic dynamic structure factor in the Boson peak[2] region [87] and our theoretical calculations for the $S(Q, E)$. The comparison shows that our theoretical $S(Q, E)$ is in fair agreement with the experi-
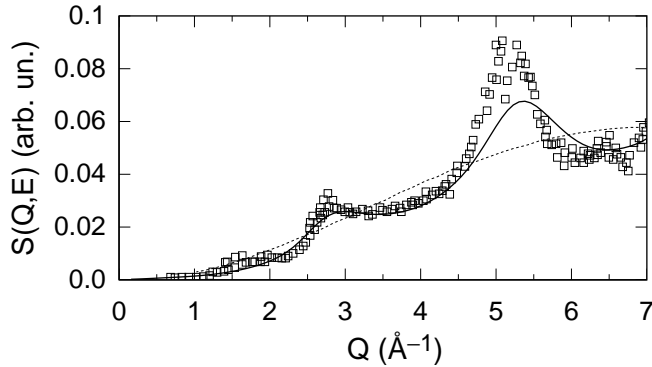

Figure 2.12: Comparison between the experimental inelastic dynamic structure factor in the Boson peak region, from 2 to 6 meV, [87] (squares) and our theoretical calculation (solid). The scattering function in the incoherent approximation from Ref. [87] (dashed) is also shown.

ments, thereby confirming the reliability of the calculated vibrational modes of our Model I of vitreous silica.

A commonly used approximation of the scattering function is the incoherent approximation [74]. This approximation assumes that one can describe the scattering function in terms of an average atom which scatters only incoherently. This assumption leads to the following formulation of the scattering function:

$$S_{inc}(Q, E) = e^{-2\bar{W}} \frac{\hbar^2 Q^2}{2\bar{M} E} [n(E) + 1] Z(E). \tag{2.27}$$

---

[2]The modes in the lower part of the density of states are of particular interest due to the existence of a broad structure-less band in the range 20–100 cm^{-1}, observed in both inelastic neutron scattering and first order Raman scattering (Refs. [89], [90]). This feature is commonly called the Boson peak, and its origin arises from an excess of modes with respect to the usual crystal-like density of states at low-energies.

In this approximation, the oscillations in the scattering function disappear. However, the intensity and the dependence on Q are well approximated (Fig. 2.12).

A generalized density of states can be defined as

$$G(Q, E) = e^{2\bar{W}} \frac{2\bar{m}E}{\hbar^2 Q^2} \frac{1}{n(E) + 1} S(Q, E),$$ (2.28)

where $\bar{m}^{-1} = \sum_I M_I^{-1}/N$ and $\bar{W} = Q^2 \langle \mathbf{u}^2 \rangle / 6$. By averaging the generalized density of states $G(Q, E)$ over Q, we obtain an effective neutron density of states $G(E)$:

$$G(E) = \frac{\int_{Q_1}^{Q_2} G(Q, E)dQ}{Q_2 - Q_1},$$ (2.29)

where Q_1, Q_2 have to be taken from the investigated experimental Q-range. In Fig. 2.13(a), we show the calculated effective neutron density of states for Model I of v-SiO$_2$, compared to experimental results from Refs. [85] and [88]. Overall we register an excellent agreement. We also show for comparison, in Fig. 2.13(b), the neutron density of states of Models II and III [48, 59]. In the low band, we note that Models II and III feature a lower number of modes. This might be related to the fact that they have a smaller size than Model I. We note also that in the spectrum of Model I, the position of the Si peak at 106 meV [Fig. 2.13(a)], is better reproduced with respect to the corresponding peaks in Models II and III [Fig. 2.13(b)]. This might be a consequence of the observed differences between the models for Si-Si correlations [Fig. 2.4], or in other words, the Si-O-Si intertetrahedral angle distribution.

2.6 Infrared spectra

2.6.1 Born charge tensors

The coupling between the atomic displacements and the electric field is described by the Born effective charge tensors Z^* [91]. As previously mentioned in Sec. 2.4, we calculated these tensors by taking finite differences of atomic forces $\mathbf{F}_I$ with respect to the electric field [47, 48]:

$$Z^*_{I,jk} = \frac{\partial F_{Ij}}{\partial \mathcal{E}_k}.$$ (2.30)

where I labels the atom and j, k run over Cartesian directions. We calculated the charge tensors Z^* for all Si and O atoms in Model I. Because of the local tetrahedral symmetry around the Si atoms, the average Z^* tensors for the Si atoms are essentially isotropic. For these atoms, we calculated an average isotropic charge of 3.3 with a standard deviation of 0.1. We represent the O tensor within a local reference set based on the orientation of the Si-O-Si bond (cf. Sec. 3.3). We take the x direction along the bisector of Si-O-Si angle, the
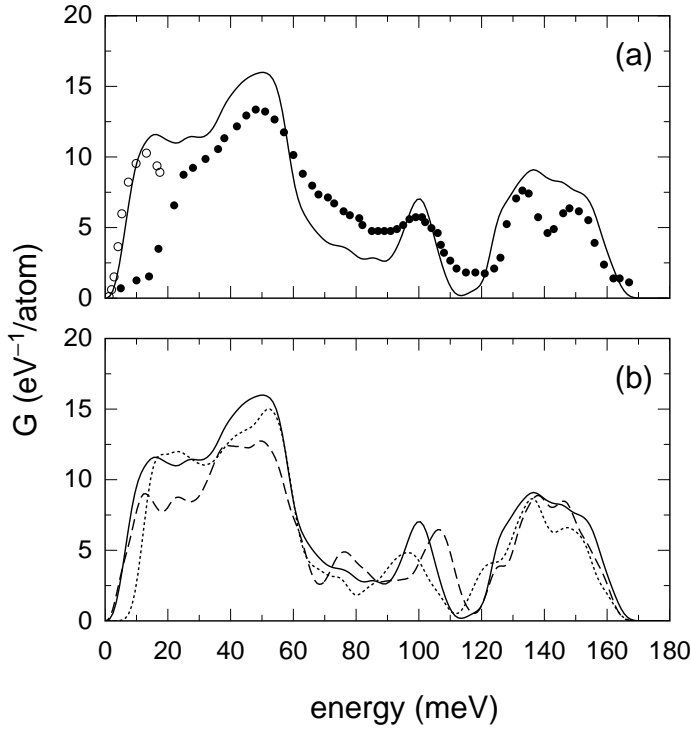
Figure 2.13: (a) Calculated effective neutron density of states for Model I of v-SiO$_2$ (solid), compared to experimental results at $T = 33$ K from Ref. [85] (closed symbols). Experimental data from Ref. [88] are also shown (open symbols). The experimental Q-range (6 to 13 Å^{-1}) and a Gaussian broadening of 2.5 meV were used in the calculation of the theoretical spectrum of Model I. (b) We also show for comparison the neutron densities of states of Models II (dotted) and III (dashed) [48, 35].

y direction normal to the plane of the Si-O-Si bridge, and the z direction orthogonal to the previous two. In this reference system, the average Z^* for O atoms reads:

$$Z_{\mathrm{O}}^* = \left(\begin{array}{ccc} -1.10 & -0.01 & 0.00 \\ -0.01 & -1.04 & 0.00 \\ 0.00 & 0.00 & -2.80 \end{array} \right). \tag{2.31}$$

This average tensor is almost diagonal, with diagonal values typical for O bridge structures [92, 3]. In particular, for the displacements along the stretching direction (z direction) the coupling is noticeably stronger.

We report in Table 2.3 the average dynamical charge tensors of our models of vitreous silica for O (Z_{O}^*) and Si (Z_{Si}^*). Small differences appear between the models that are a consequence of the different bond-angle and bond-length distributions.

In Fig. 2.14, we correlate the isotropic O Born charge with the corresponding Si-O-Si angle. The Born charge is found to decrease with increasing bond angle [3]. The trend is the same for all the three models with a similar spreading of data. In particular, we remark that differences in the intertetrahedral angular distribution (or ring-statitistics) do not give rise to deviations from the main trend.

Table 2.3: High frequency (ϵ_∞) and static dielectric constants (ϵ_0) for Models I to III of vitreous SiO$_2$. Average isotropic Born charge for O (Z_O^*) and Si (Z_{Si}^*), together with the standard deviations of their respective distributions (in parentheses). For Models II and III, published values are taken from Refs [59], [35], and [48]. Experimental values are taken from Refs. [93] and [94].

	ϵ_∞	ϵ_0	Z_O^*	Z_{Si}^*
Model I	2.1	3.8	-1.649 (0.062)	3.298 (0.106)
Model II	2.0	3.8	-1.696 (0.046)	3.392 (0.079)
Model III	2.0	3.6	-1.588 (0.078)	3.177 (0.121)
Expt.	2.1	3.8		

2.6.2 Dielectric constant and dielectric function

We calculated for our models of v-SiO$_2$, the high-frequency dielectric tensors ϵ_∞ that is related to the dielectric susceptibility [47, 48]:

$$(\epsilon_\infty)_{ij} = \delta_{ij} + 4\pi\chi_{ij} \tag{2.32}$$

$$\chi_{ij} = \frac{\partial^2 E}{\partial \mathcal{E}_i \partial \mathcal{E}_j} = \frac{\partial P_i^{el}}{\partial \mathcal{E}_j}. \tag{2.33}$$

The dielectric tensor calculated for Model I is almost isotropic, as expected for an amorphous system [83]. From the isotropic part of the dielectric tensor $\epsilon_\infty = \mathrm{Tr}(\epsilon_\infty)/3$, we obtained an average dielectric constant of 2.1, in very good agreement with the experimental value of 2.1 (Ref. [93]).

In the following, we describe the coupling to invidual vibrational modes. It is therefore convenient to introduce the oscillator strengths $\mathcal{F}^n$:

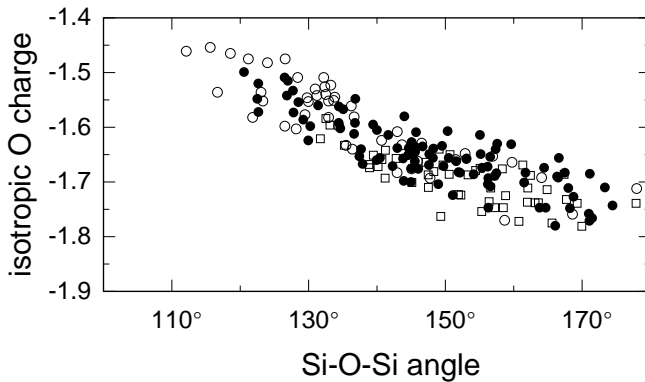$$\mathcal{F}_j^n = \sum_{Ik} Z_{I,jk}^* \frac{\xi_{Ik}^n}{\sqrt{M_I}}. \tag{2.34}$$

Figure 2.14: Isotropic oxygen Born charge vs Si-O-Si angle for our three models of v-SiO$_2$: Model I (disks), Model II (open squares), Model III (circles).
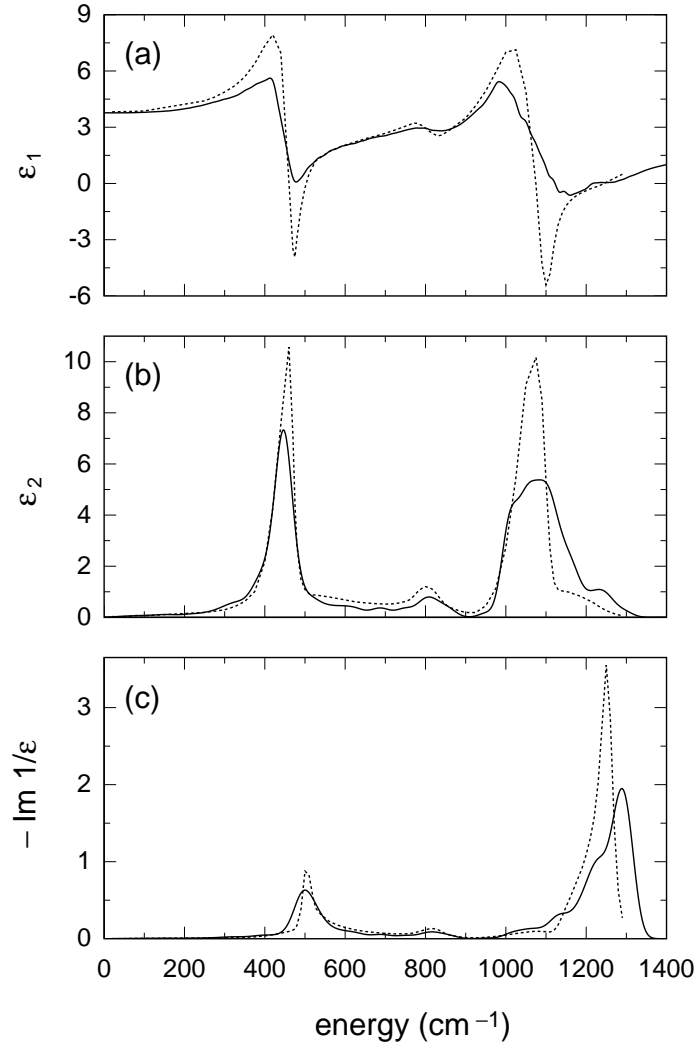
Figure 2.15: Real (a) and imaginary parts (b) of the dielectric function and (c) energy loss function for Model I of v-SiO$_2$ (solid) compared to experimental data [93] (dotted). Lorentzian and Gaussian broadenings of 19 cm^{-1} are used for the real and imaginary parts, respectively.

We evaluated the static dielectric constant using the calculated oscillator strengths and vibrational frequencies [3]:

$$\epsilon_0 = \epsilon_\infty + \frac{4\pi}{3V} \sum_n \frac{|\mathcal{F}^n|^2}{\omega_n^2}, \tag{2.35}$$

where V is the volume of the periodic simulation cell. For Model I, we obtained $\epsilon_0 = 3.8$, in excellent agreement with the experimental value $\epsilon_0^{\text{expt}} = 3.8$ [94].

The real and imaginary parts of the dielectric response function, $\epsilon_1(\omega)$ and $\epsilon_2(\omega)$, are given by [95, 3]:

$$\epsilon_1(\omega) = \epsilon_\infty - \frac{4\pi}{3V} \sum_n \frac{|\mathcal{F}^n|^2}{\omega^2 - \omega_n^2}, \tag{2.36}$$

$$\epsilon_2(\omega) \quad = \quad \frac{4\pi^2}{3V} \sum_n \frac{|\boldsymbol{\mathcal{F}}^n|^2}{2\omega_n} \delta(\omega - \omega_n). \tag{2.37}$$

The dielectric function described above gives access to all the dielectric properties. In particular, the energy loss function is obtained as $-\text{Im}[1/\epsilon(\omega)]$. However, it was found convenient to access the latter function by a direct calculation [95, 48]:

$$-\text{Im}\left[\frac{1}{\epsilon(\omega)}\right] = \frac{4\pi^2}{V(\epsilon_\infty)^2} \sum_n \frac{(\mathbf{q} \cdot \boldsymbol{\mathcal{F}}^n)^2}{2\omega_n} \delta(\omega - \omega_n). \tag{2.38}$$

For isotropic systems, the energy loss function in Eq. (2.38) can be averaged over all directions $\mathbf{q}$. Here, we used the three Cartesian directions for this average.

In Figure 2.15, we show the real and imaginary parts of the dielectric function calculated for Model I together with the experimental result [93]. The agreement with experiment is of the same quality as for Models II and III (Refs. [3, 48]). In Fig. 2.16, we show the comparison between the imaginary part of the dielectric functions of Models I, II and III. The three models give spectra with a similar overall shape. This similarity stems from the common short-range order which dominates the infrared spectra [4, 96]. However, in the central band ranging between 400 cm^{-1} and 700 cm^{-1}, and also in the high frequency band ranging between 1000 cm^{-1} and 1200 cm^{-1}, we observe minor differences between the calculated spectra. Since these bands arise from O bending and O stretching modes, respectively, these differences reflect the differences in the Si-O-Si angle and Si-O bond-length distributions. The function ϵ_2 of Model I appears to give a better global agreement with experiment than those of Models II and III, particularly in the central part of the spectrum. Indeed, the spectra of the latter two models feature spurious peaks in the range 700–900 cm^{-1} that are absent in the experimental spectrum (Fig. 2.16 and 2.15). However, the high frequency peak at ~1100 is wider in Models I and II than in Model III. This fact should be attributed to the better relaxation of the atomic configuration of Model III [59] with respect to those of Models I and II [48].
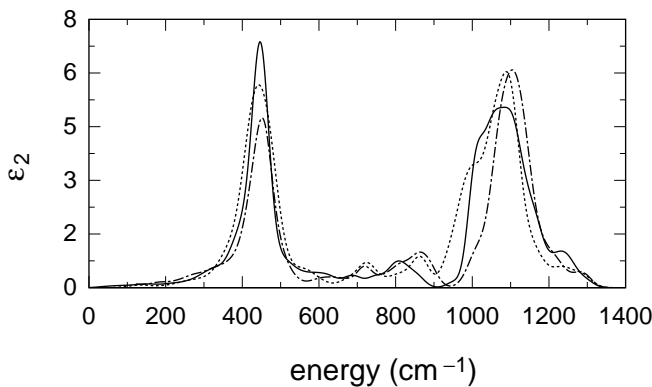

Figure 2.16: Imaginary parts of the dielectric function of our models of v-SiO$_2$, Model I (solid), Model II (dashed), Model III (dot-dashed). Data for Model II and III are taken from Refs. [48] and [3]. A Gaussian broadening of 19 cm^{-1} is used.

2.7   Raman scattering

In a first-order Stokes process of Raman scattering, an incoming photon of frequency Ω_L and polarization $\hat{e}_L$ is scattered to an outgoing photon of frequency Ω_S and polarization $\hat{e}_S$ and a vibrational excitation of frequency $\omega_n = \Omega_L - \Omega_S$. The Raman cross section is given by [6]:

$$\frac{d^2\sigma}{d\Omega\, dE} \sim \sum_n |\hat{e}_S \cdot \boldsymbol{\mathcal{R}}^n \cdot \hat{e}_L|^2 \frac{\hbar}{2\omega_n} [n(\omega_n) + 1]\, \delta(E - \hbar\omega_n), \tag{2.39}$$

where E is the exchanged energy, and $n(\omega_n)$ is the Boson factor

$$n(\omega_n) = \frac{1}{\exp(\hbar\omega_n/k_B T) - 1}. \tag{2.40}$$

The second rank tensors $\boldsymbol{\mathcal{R}}^n$ are the Raman susceptibilities associated to the normal mode n:

$$\mathcal{R}^n_{ij} = \sqrt{V} \sum_{Ik} \frac{\partial \chi_{ij}}{\partial R_{Ik}} \frac{\xi^n_{Ik}}{\sqrt{M_I}}, \tag{2.41}$$

where the derivatives of the dielectric polarizability tensor χ_{ij} can be expressed as

$$\frac{\partial \chi_{ij}}{\partial R_{Ik}} = \frac{1}{V} \frac{\partial^2 F^{\mathcal{E}}_{Ik}}{\partial \mathcal{E}_i \partial \mathcal{E}_j}\bigg|_0. \tag{2.42}$$

The $F^{\mathcal{E}}_{Ik}$ indicate the components of the atomic forces on atom I in the presence of an electric field $\mathcal{E}$. Often the experimental Raman cross section is given in a reduced form, where one omits of the bosonic factor:

$$\frac{d^2\sigma}{d\Omega\, dE}\bigg|_{\text{red}} = \frac{d^2\sigma}{d\Omega\, dE} \cdot \frac{\omega}{n(\omega) + 1}. \tag{2.43}$$

We calculated the tensors $\partial \chi_{ij}/\partial R_{Ik}$ of Model I by taking finite differences of atomic forces. We obtained the diagonal terms $\partial \chi_{ii}/\partial R_{Ik}$, by considering values for the electric field of ± 0.0025 and ± 0.005 a.u., and by using the following formula for second-order numerical derivatives of a one-variable function f:

$$f''(0) \simeq \frac{1}{12h^2}\left[-f(-2h) + 16f(-h) - 30f(0) + 16f(h) - f(2h)\right]. \tag{2.44}$$

From the Taylor development of $F^{\mathcal{E}}$ (we droped the indices Ik) it is possible to find a numerical finite-differences scheme [97] to access the off-diagonal ($i \neq j$) terms of $\partial \chi_{ij}/\partial R_{Ik}$:

$$F(\mathcal{E}_i, \mathcal{E}_j) = F(0,0) + \frac{\partial F}{\partial \mathcal{E}_i}\bigg|_0 \mathcal{E}_i + \frac{\partial F}{\partial \mathcal{E}_j}\bigg|_0 \mathcal{E}_j + \frac{1}{2}\frac{\partial^2 F}{\partial \mathcal{E}_i^2}\bigg|_0 \mathcal{E}_i^2 + \frac{1}{2}\frac{\partial^2 F}{\partial \mathcal{E}_j^2}\bigg|_0 \mathcal{E}_j^2 + \frac{\partial^2 F}{\partial \mathcal{E}_j \partial \mathcal{E}_j}\bigg|_0 \mathcal{E}_i \mathcal{E}_j + ...$$
$$\tag{2.45}$$

By defining a $\mathcal{E}_i = \mathcal{E}_j = h$, the mixed term $\partial^2 F/\partial \mathcal{E}_i \partial \mathcal{E}_j$ is given by:

$$\frac{\partial^2 F}{\partial \mathcal{E}_i \partial \mathcal{E}_j}\bigg|_0 \simeq \frac{1}{4h^2}\left[F(h,h) + F(-h,-h) - F(-h,h) - F(h,-h)\right] \tag{2.46}$$

In order to compute the mixed term, we make use of the possibility of applying simultaneously finite fields along two different Cartesian directions, currently implemented in the CPV code [64]. We applied electric fields of intensity $\pm$ 0.001768 and $\pm$ 0.003536 a.u. along the three different couples of Cartesian directions, and used Eq. (2.44) for computing the derivative $\partial^2 F/\partial \mathcal{E}^2$. In this way, we could obtain all the tensors $\partial \chi_{ij}/\partial R_{Ik}$ by 25 selfconsistent minimizations of the electric-field dependent energy functional. No sensible variation of the calculated spectra is found if second-order derivatives (2.44) are calculated with a three-point formula.

2.7.1 Details of the calculations of Raman spectrum

The computation of the Raman spectrum basically requires the knowledge of the eigenmodes of the system and of the third derivatives of the energy with respect to the electric field and the positions. Once that these quantities are available, it is possible to calculate the Raman susceptibilities $\mathcal{R}_{ij}^k$ [Eq. (2.41)].

The calculation of the contribution of the kth vibrational mode to the Raman spectra, requires taking the average of the tensors $\mathcal{R}_{ij}^k$ over all possible directions [6, 98] because of the isotropic nature of disordered solids. This average can be expressed by means of the trace a and the anisotropy τ of the tensor $\mathcal{R}_{ij}^k$. The latter quantities are defined as (in the following we drop the index k for clarity):

$$
\begin{aligned}
a &= (\mathcal{R}_{11} + \mathcal{R}_{22} + \mathcal{R}_{33})/3 \\
\tau^2 &= [(\mathcal{R}_{11} - \mathcal{R}_{22})^2 + (\mathcal{R}_{22} - \mathcal{R}_{33})^2 + (\mathcal{R}_{33} - \mathcal{R}_{11})^2 \\
&\quad + 6\,(\mathcal{R}_{11}^2 + \mathcal{R}_{22}^2 + \mathcal{R}_{33}^2)]/2
\end{aligned}
$$

Then, the intensity of the HH Raman spectrum associated to the k mode is given by:

$$
I_{\text{HH}} = a^2 + \frac{4\tau^2}{45}. \tag{2.47}
$$

In Raman spectroscopy, it is customary to define the depolarization ratio:

$$
\rho_{\text{dep}} = \frac{3\tau^2}{45a^2 + 4\tau^2} \tag{2.48}
$$

that links the HV and HH spectra in the following way:

$$
I_{\text{HV}} = I_{\text{HH}} \cdot \rho_{\text{dep}}. \tag{2.49}
$$

The final HH (HV) spectrum is obtained by applying a Gaussian broadening, as explained in Appendix A, to the mode intensities I_{HH}^k (I_{HV}^k). The broadening is applied in order to take into account both the experimental width of the Raman lines and the finite size of our models.

2.7.2   Raman spectra of v-SiO$_2$

In Fig. 2.17(a) and (b), we report both the reduced and non-reduced HH and HV Raman spectra of Model I of v-SiO$_2$ compared to experimental data taken from Refs. [99] and [100]. Overall we register a good agreement with experimental data both for the reduced and non-reduced spectra. The small differences between experiment and theory appearing in the reduced spectra, below ~ 400 cm^{-1} are emphasized in the non-reduced spectra, due to the Boson factor [(Eq. 2.40]. The lower band of the non-reduced HV spectrum clearly features a broad peak in the Boson peak region at ~ 50 cm^{-1} [Fig. 2.17(b)]. In Models II and III this feature is unresolved and instead spurious features occur at ~ 150 cm^{-1} (not shown). Thus, Model I appears to give the best description of the lower frequency region of the Raman spectra.

2.7.3   Dependence of HH Raman spectrum on Si-O-Si angle

It has been seen in Refs. [4, 48] that the HH Raman spectrum of v-SiO$_2$ shows a strong dependence on the medium-range order through the Si-O-Si bond angle distribution. The HH Raman spectrum of vitreous silica is dominated by the coupling to O bending motions. A further analysis revealed that the tensors $\partial\boldsymbol{\chi}/\partial\mathbf{R}$ associated to these motions are almost isotropic. Identifying the bisector direction of the Si-O-Si bond angle by $\mathbf{e}^b$, we express the coupling factor for each O atom in terms of a volume-independent scalar:

$$f_I = \frac{1}{3}V\,\mathrm{Tr}\left(\sum_k \frac{\partial\boldsymbol{\chi}}{\partial R_{Ik}}\mathbf{e}^b_{Ik}\right).\tag{2.50}$$

Figure 2.18(b) shows that, for Model I, the HH Raman spectrum below 925 cm^{-1} is reproduced up to 89% when only the isotropic part of the coupling to O bending motions is accounted for.

The coupling factors f_I associated to the O atoms show a clear a correlation with the corresponding Si-O-Si bond angle θ_I [Fig. 2.18(a)]. The observed dependence is expressed by the relation [4]

$$f_I = (\alpha/3)\cos(\theta_I/2),\tag{2.51}$$

which holds for the bond-polarizability model [101] for a system of regular tetrahedral units. A one-parameter least-squared fit of the coupling factors calculated in Model I, gives a value of 40.1 bohr^2 for the parameter α. This value is in agreement with previous calculations [4] which derived a value of 46.5 bohr^2 from the analysis of Model III. The small difference could arise from the different methods applied to compute the derivatives of the Raman susceptibilities [83].
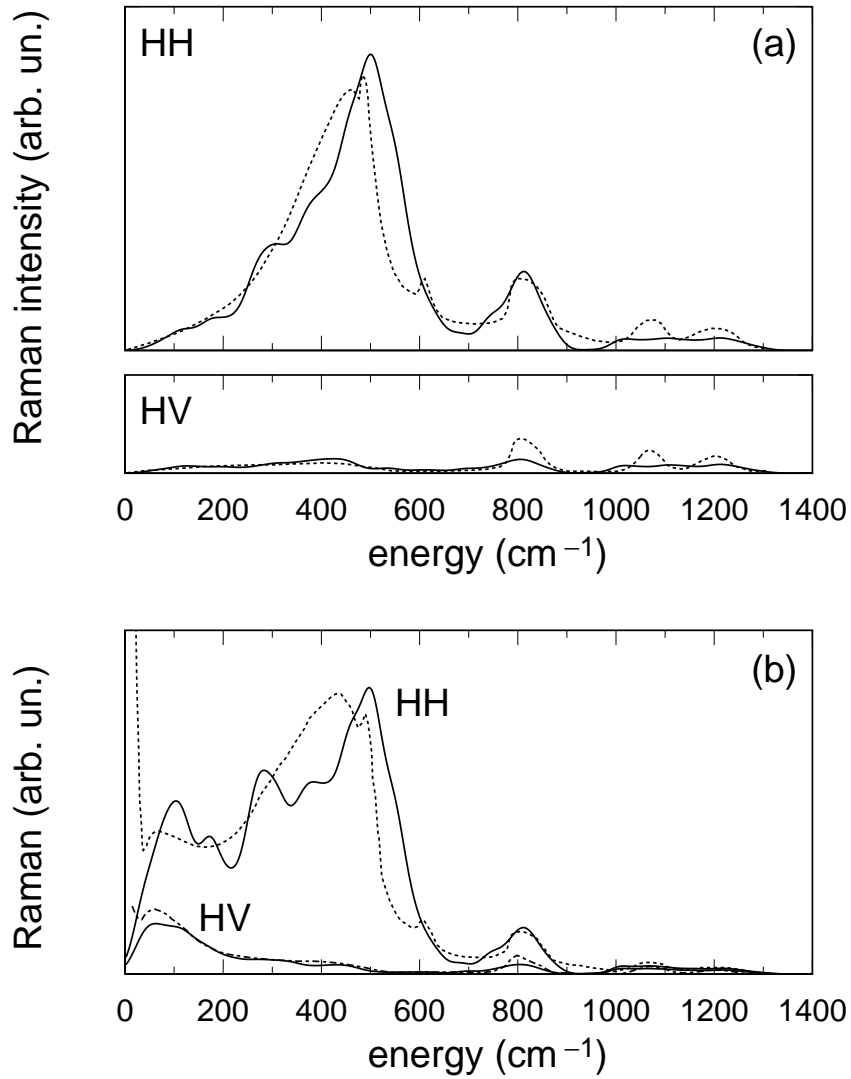
Figure 2.17: (a) Calculated HH and HV reduced Raman spectra of Model I (solid) compared with the experimental data of Ref. [99] (dotted). (b) HH and HV non-reduced Raman spectra of Model I (solid) compared with the experimental data of Ref. [100] (dotted). A Gaussian broadening of 19 cm^{-1} is used.
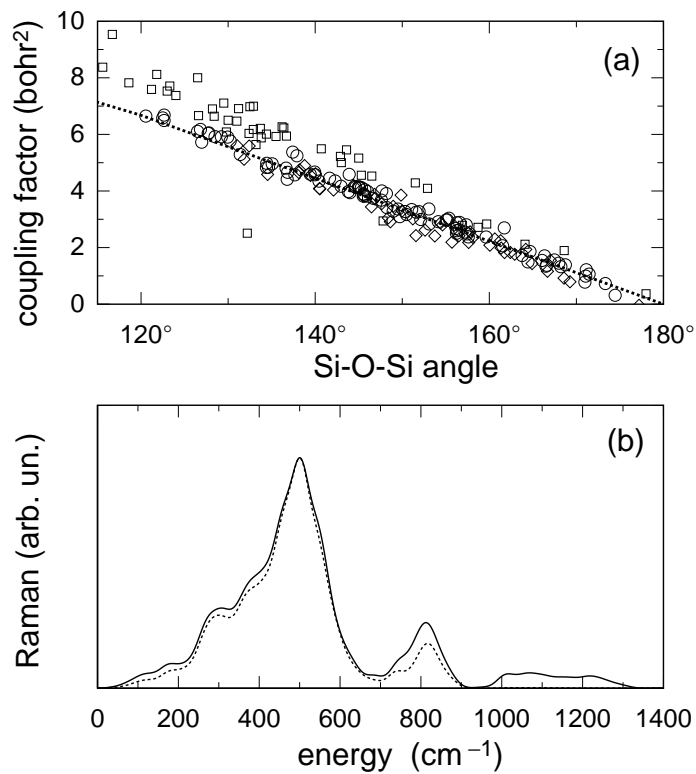
Figure 2.18: (a) Raman coupling factors f_I vs Si-O-Si angle, calculated for O atoms in Model I (circles), Model II (diamonds), Model III (squares). Raman derivatives $\partial\chi/\partial\mathbf{R}$ in Model III were computed through a perturbative approach [4]. (b) Model I: HH Raman spectrum (solid) together with the intensity obtained by retaining only the isotropic part of the Raman couplings associated to oxygen bending motions (dotted).

In Fig. 2.19, we show the reduced HH Raman spectra of our models of v-SiO$_2$. The three spectra show large differences especially in the range 300–700 cm^{-1}, i.e. for the bending band. The Raman spectra of Fig. 2.19 mainly reflect the differences in the corresponding Si-O-Si distributions and ring-statistics (Figs. 2.2 and 2.5). The relation between the latter, in the case of small rings, and the spectra will be further investigated in the next section.
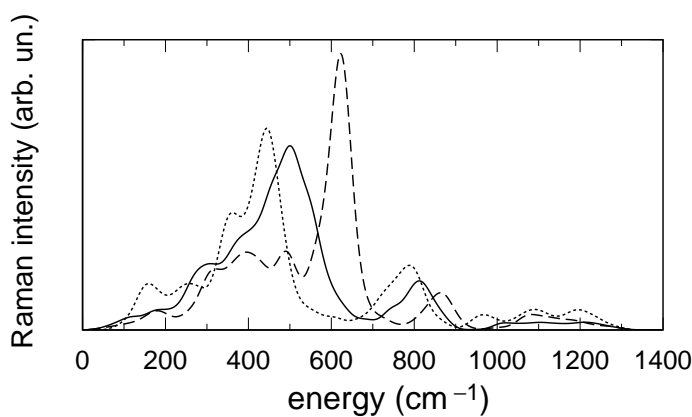

Figure 2.19: Calculated reduced HH Raman spectra of Model I (solid) Model II (dotted) and III (dashed). The results for Model II and III are taken from Refs. [48] and [4], respectively. A Gaussian broadening of 19 cm^{-1} is used.

2.7.4 Raman defect lines and small rings

The Raman spectrum of v-SiO$_2$ shows two particularly sharp lines, D_1 and D_2, which appear in addition to broader bands [19]. A first-principles investigation [21] has definitely assigned the origin of these lines to localized vibrations in small rings, as proposed by Galeener [99]. From the intensities of these lines, an estimate of the concentration of three- and four-membered rings in v-SiO$_2$ could be derived [4]. A recent analysis applied to v-B$_2$O$_3$ has analogously succeeded in giving an estimate of the fraction of B atoms in boroxol rings [5].

Three-membered rings in vitreous silica can be considered as some type of "structural defect", characterized by their own vibrational modes which can be excited independently from the rest of the network [102]. As a consequence of this, recent investigations in v-SiO$_2$ carried out through femtosecond spectroscopy have shown that the time-domain response is dominated by the D_1 and D_2 modes [103].

A previous study has shown that the principal peak at $\sim$620 cm^{-1} in the spectrum of Model III (Fig. 2.19) arises from the breathing vibration of oxygen atoms in three-membered rings (Refs. [21] and [4]). Consistent with this assignment, the HH Raman spectrum of Model II, where three-membered rings are absent, does not show any feature at about $\sim$600 cm^{-1}. However, the spectrum of Model I does not show either any feature in that range, despite it has one three-membered ring. Nevertheless, the contribution due to the breathing motion of oxygen atoms in the single three-membered ring in Model I shows a Raman peak at $\sim$ 610 cm^{-1}, in close correspondence to the position of the D_2 Raman line [Fig. 2.20(a)]. The fact that this feature does not show up in the total spectrum is probably due to the structural distortions in the ring. Indeed this ring shows a lower degree of planarity with respect to three-membered rings in Model III [21].

In Model I the concentration of four-membered rings is relatively high. In fact, $\sim$42% of the O atoms belong to such rings. This concentration is much larger than the estimate derived from the experimental D_1 line (0.36 %) [4] and affects the shape of the total HH Raman spectrum. Indeed, the main peak at $\sim$ 500 cm^{-1} mainly arise from the oxygen bending motion in four-membered rings, as shown in Fig. 2.20(b). The peak of the projection on bending modes is located at $\sim$510 cm^{-1} in good agreement with the experimental position of the D_1 line ($\sim$495 cm^{-1}).

2.7.5 Bond polarizability model

The bond polarizability model [101] has successfully been applied to the calculation of Raman intensities in a large variety of systems [6]. In particular, the bond polarizability
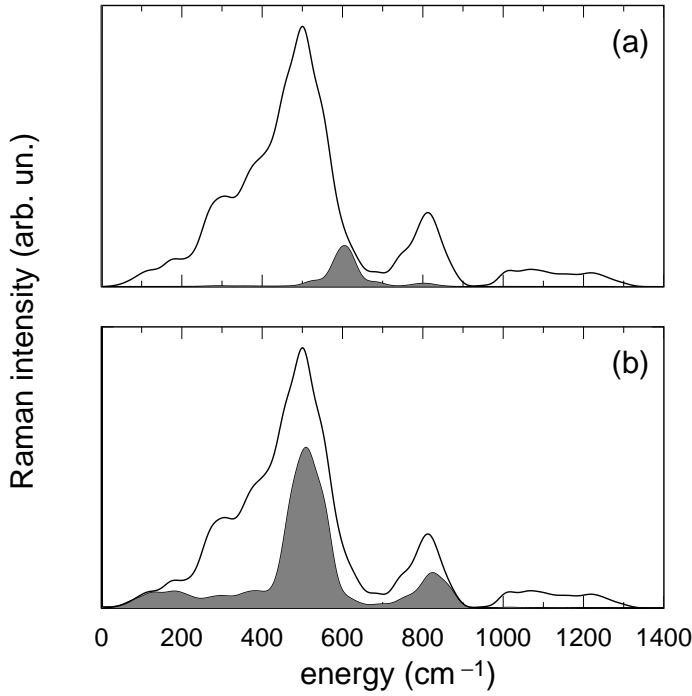
Figure 2.20: HH Raman spectrum for Model I (solid) in which the contribution is highlighted due to the breathing motion of oxygen atoms within the three-membered ring (a) and (b) due to the bending motion of oxygen atoms in four-membered rings. A Gaussian broadening of 19 cm^{-1} was used.

model has been shown to give a reliable description of the Raman intensities in SiO$_2$ (Refs. [46] and [104]). Subsequently it was also applied to study the Raman spectra of normal and compressed v-SiO$_2$ [105]. For future reference, we derive in this section optimal bond-polarizability parameters from our first-principles calculation of the tensors $\partial\boldsymbol{\chi}/\partial\boldsymbol{R}$.

In the bond polarizability model, the polarizability is described in terms of bond contributions:

$$\alpha_{ij} = \frac{1}{3}\left(2\alpha_p + \alpha_l\right)\delta_{ij} + \left(\alpha_l - \alpha_p\right)\left(\frac{R_i R_j}{R^2} - \frac{1}{3}\delta_{ij}\right), \tag{2.52}$$

where $\mathbf{R} = \mathbf{R}_J - \mathbf{R}_I$ is a vector which defines the direction and the distance of a pair of nearest neighbor atoms at sites $\mathbf{R}_I$ and $\mathbf{R}_J$. The parameters α_l and α_p correspond to the longitudinal and perpendicular bond polarizability, respectively. The bond polarizability model further assumes that the bond polarizabilities α_l and α_p only depend on the length of the bond. Thus, the derivative of the bond polarizability with respect to the displacement of the atom J reads:

$$\begin{aligned}
\frac{\partial\alpha_{ij}}{\partial R_{Jk}} &= \frac{1}{3}\left(2\alpha_p' + \alpha_l'\right)\delta_{ij}\hat{R}_k + \\
&\quad + \left(\alpha_l' - \alpha_p'\right)\left(\hat{R}_i\hat{R}_j - \frac{1}{3}\delta_{ij}\right)\hat{R}_k + \\
&\quad + \frac{\left(\alpha_l - \alpha_p\right)}{R}\left(\delta_{ik}\hat{R}_j + \delta_{jk}\hat{R}_i - 2\hat{R}_i\hat{R}_j\hat{R}_k\right),
\end{aligned} \tag{2.53}$$

where $\hat{\mathbf{R}}$ is a unit vector along $\mathbf{R}$, and α_l' and α_p' are the derivatives of the bond polarizabilities with respect to the bond length. Therefore, when only one type of bond occurs,

the bond polarizability model is completely defined by three parameters:

$$\alpha = 2\alpha'_p + \alpha'_l, \quad \beta = \alpha'_l - \alpha'_p, \quad \gamma = (\alpha_l - \alpha_p)/R. \tag{2.54}$$

We then obtain the tensor $\partial\boldsymbol{\chi}/\partial\boldsymbol{R}$ which appears in Eq. (2.42) by dividing the tensor $\partial\boldsymbol{\alpha}/\partial\boldsymbol{R}$ by the volume V.

	α	β	γ
Model I	40.1	8.5	2.0
Model II	41.2	8.9	2.1
Model III	46.5	10.3	2.2

Table 2.4: Parameters (expressed in bohr^2) of the bond polarizability model as derived from Models I, II, and III.
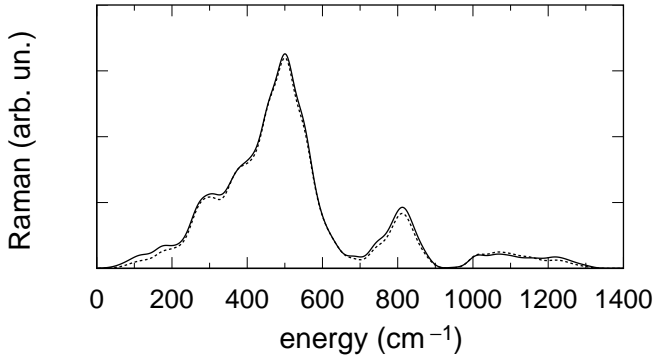

Figure 2.21: Reduced HH Raman spectrum of Model I calculated with full *ab initio* Raman tensors (solid) and with bond polarizability Raman tensors. A Gaussian broadening of 19 cm^{-1} is used.

We determined optimal parameters as follows. First, we fixed the parameter α which is responsible for the principal Raman peak, as described in Sec. 3.5.1. We obtained the other parameters by minimizing the sum of squared differences between the components of the tensor $\partial\boldsymbol{\chi}/\partial\boldsymbol{R}$ calculated within the bond polarizability model and within our first-principles scheme. This results in the parameters for v-SiO$_2$ summarized in Table 2.4.

It is interesting to compare these values with those obtained for α-quartz following a similar optimization scheme [46]:

$$\alpha = 45.5, \quad \beta = 11.6, \quad \gamma = 3.3, \tag{2.55}$$

expressed in the same units as the values for v-SiO$_2$. The comparison between the absolute values of these parameters clearly indicates that the derivatives of the polarizability for the Si-O bond in vitreous silica are very close to those for the Si-O bond in α-quartz. The ratios β/α, γ/α are very similar for the two forms of SiO$_2$ indicating that the disorder plays a minor role in the response of the Si-O bond. In Figure 2.21, we show the performance of the bond polarizability model in reproducing the *ab initio* Raman spectrum of Model I.

2.8 Conclusions

In this chapter we analysed the structural and vibrational properties of three models of v-SiO$_2$, one of which was generated in this work (Model I). This chapter aims in part at introducing the reader to the typical analysis that can nowadays be performed in the field of the first-principles modeling of vitreous materials. Moreover we illustrate a method to calculate the pair correlation functions that simply requires the knowledge of the vibrational modes, the scattering length of the atom species, and the atomic positions. This method has the advantage to include the zero point fluctuations. We also provide in this chapter an analysis of the FSDP in the total structure factor and in the concentration-concentration structure factor which consists in a decomposition according to intra- and intertetrahedral terms. Furthermore, we consider the x-ray structure factor of Model I and compare it to experimental data and to neutron structure factor. The HH Raman spectrum of Model I shows an overall good agreement with experimental data, as good as Model II and slightly better than Model III.

The comparisons between the three models help us to extend our understanding of the relationship between the features in the infrared and Raman spectra and the model structure. In particular, differences between the three models appearing in the bond-length distribution (or in the Si-O-Si angular distribution) are reflected in the imaginary part of the dielectric function and in the HH Raman spectrum. For the latter, the comparisons between our models clearly illustrate the dramatic effect of the concentration of three-membered rings.

The comparison between several selected models turns out to be a powerful tool to investigate and assign the features of the vibrational spectra. Guided by this general statement, we will proceed in a similar way, in our investigations on v-GeO$_2$ and v-GeSe$_2$, and generate in the first step, a set of models differing by some structural property, like the ring-statistics or the intertetrahedral angle distribution.

Chapter 3

Vibrational spectra of v-GeO$_2$

In this chapter, we address the vibrational spectra of vitreous germania within a density functional framework. We started our investigation by generating four model structures of v-GeO$_2$ and by analyzing their structural properties. We carry out detailed comparisons with experiment by considering the total neutron and pair correlation function, the total neutron and x-ray structure factor, and partial structure factors both in the Faber-Ziman and Bhatia-Thornthon formulations. Next, we address the vibrational properties. The vibrational eigenmodes are not only analyzed in terms of germanium and oxygen weights but also in terms of stretching, bending and rocking motions [60]. The vibrational density of states is compared to the inelastic neutron spectrum finding the same kind of correspondence as for vitreous silica [35, 36]. We then turn to the dielectric properties. We give the real and imaginary part of the dielectric function and the energy loss function and compare them with experimental results when available. In particular, we also calculated the static dielectric constant. Furthermore, we address the dynamical Born charges, the relevant coupling factors in the infrared spectra, and show a clear relation between the oxygen dynamical Born charges and the local structural environment. Particular attention is dedicated to the Raman spectra, because of their sensitivity to medium-range structural properties. The generated model structures show various Ge-O-Ge bond-angle distributions and ring statistics. This allow us to illustrate the dependence of the Raman spectra on these medium-range structural properties. In particular, we support the assignment of the X_2 shoulder to three-membered rings through projections on ring vibrations. We also investigate the origin of the X_1 shoulder on the opposite side of the main Raman peak. We find that the underlying eigenmodes correspond to bond-bending motions in the Ge-O-Ge bridge, leading us to suggest that this feature results from diffuse network motions rather than from vibrations localized within specific structural subunits. In the final part of our study, we focus on the Raman coupling factors and derive therefrom optimal bond-

polarizability parameters.

This chapter is organized as follows. In Sec. 3.1, we outline the generation procedures that gave rise to the model structures of v-GeO$_2$ used in this work. In Sec. 3.2, we address the structural properties of v-GeO$_2$ focusing on the largest of these model structures. Section 3.3 is devoted to the analysis of the vibrational properties, including the vibrational density of states and the inelastic neutron spectrum. Section 3.4 contains the infrared properties, including the dielectric function, the static dielectric constant and the dynamical Born charges. Section 3.5 addresses the Raman spectra. In particular, we focus on the relation between the Raman spectra and the intertetrahedral angle distribution, on the origin of the features X_1 and X_2, and on the derivation of optimal bond polarizability parameters. The conclusions are given in Section 3.6.

3.1   Models generation

All the models of v-GeO$_2$ generated in this work are subject to periodic boundary conditions, have cubic simulation cells, and have the experimental density ($\sim$3.65 g/cm^{-3}) [17]. The analysis is mainly based on a structural model of 168 atoms, hereafter referred to as Model I. For comparison, we also generated three smaller models, containing either 72 (Models II and III) or 36 atoms (Model IV). These models show different structural properties as reflected by their intertetrahedral angular distributions and ring statistics [15].

Model I was generated according to the following procedure. First, we carried out classical molecular dynamics [8] of SiO$_2$ at 2.7 g/cm^3 corresponding to the experimental packing density of tetrahedra in v-GeO$_2$. The system was first heated up to a temperature of 3500 K and thermalized for a period of 50 ps. Then, we quenched the temperature to 300 K at a rate of -13 K/ps by scaling the velocities. After a subsequent thermalization of 25 ps, we obtained a disordered structure consisting of a chemically ordered network of corner-sharing tetrahedra. We then transformed the obtained structure to a model of v-GeO$_2$ by rescaling the simulation cell by the Ge-O/Si-O bond length ratio and by further optimizing the atomic positions through damped first-principle molecular dynamics [56, 63].

We generated Model II according to a similar procedure. However, in this case, the classical molecular dynamics of SiO$_2$ was carried out at the experimental density of silica [8]. The model was then transformed by rescaling the simulation cell to the experimental density of v-GeO$_2$. The structural properties were finally adjusted through a final first-principles relaxation.

Model III was generated by replacing Si with Ge in a model structure of v-SiO$_2$, generated previously by first-principles molecular dynamics [59]. We obtained a model of
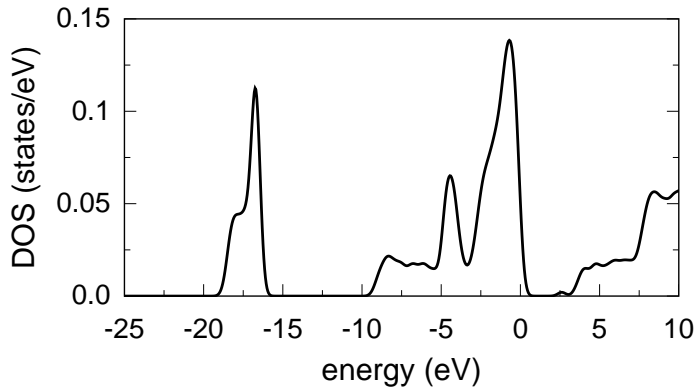
Figure 3.1: Electronic density of states (DOS) for Model I of v-GeO$_2$. The highest occupied states are aligned at 0 eV. A Gaussian broadening of 0.25 eV is used.

v-GeO$_2$ by rescaling the simulation cell and by carrying out a first-principles relaxation as for Model II. Model IV was generated in the same way as Model II, but with a smaller number of atoms.

In this chapter, we performed electronic and structural relaxations using first principles methodologies [56, 63], as provided in the QUANTUM-ESPRESSO package [64]. The exchange and correlation energy was accounted for through a generalized gradient approximation (GGA) [106] to density functional theory. Plane wave basis sets with energy cutoffs of 25 Ry and 250 Ry were used to expand the electron wave functions and the electron density, respectively. Core valence interactions were accounted for by a norm-conserving pseudopotential for Ge (Ref. [107]) and an ultrasoft one for O [66]. The wave functions were expanded at the sole Γ point of the Brillouin zone, as justified by the large size and the large band gap of our systems.

The electronic density of states of Model I is presented in Fig. 3.1. The origin of the bands in terms of atomic orbitals is similar to the case of SiO$_2$ [67]: the lowest band arises from O-2s states, the low-energy side of the central band results from the bonds between Ge-sp^3 and O-2p orbitals. The high-energy side of this central band consists of O-2p lone pairs, which define the top of the valence band. The low-energy part of the conduction band mainly consists of Ge orbitals. The calculated band gap (2.6 eV) significantly underestimates the experimental value (5.6 eV, Ref. [108]), as usual in density functional schemes. The present electronic density of states is consistent with previous calculations for α-quartz GeO$_2$ and v-GeO$_2$ [109].

For all our models, we obtained the normalized vibrational modes $\boldsymbol{\xi}^n$ and frequencies ω_n through the diagonalization of the dynamical matrix (cf. Sec. 2.4). The dynamical matrices were calculated numerically by taking finite differences of the atomic forces [35]. Atomic displacements of ± 0.1 bohr were used in these calculations.
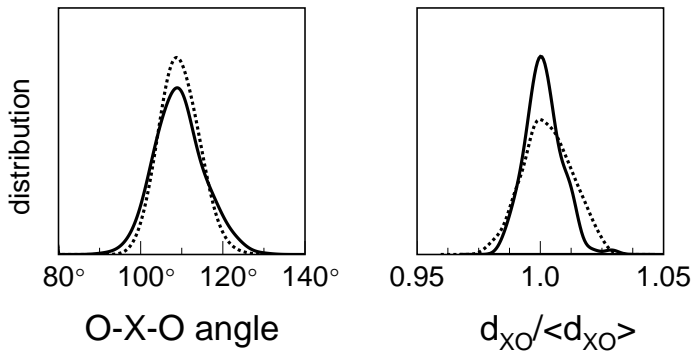
Figure 3.2: Distribution of the O-X-O angle and of the bond length d_{XO} (X = Ge, Si) for Model I of v-GeO$_2$ (solid) and for Model I of v-SiO$_2$ (Sec. 2.1). The bond lengths are rescaled with respect to their average value. Gaussian broadenings of $2.5°$ and 0.005 Å are used.
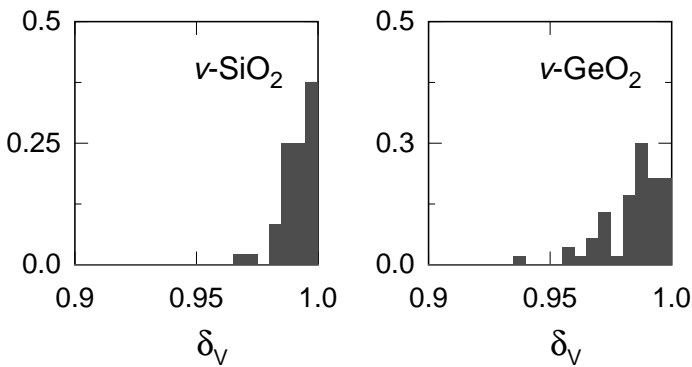

Figure 3.3: The distribution of the distortion parameter δ_V is given for the same models considered in Fig. 3.2. We found a spread of 0.011 and 0.020 for v-SiO$_2$ and v-GeO$_2$, respectively.

3.2 Structural properties

3.2.1 Real-space properties

Short-range order

We analysed the short-range order in Model I by focusing on the structural properties of the basic structural unit corresponding to the GeO$_4$ tetrahedron. The Ge-O bond-length and the O-Ge-O bond-angle distributions are shown in Figs. 3.2 and 3.3. The mean values of these distributions are reported in Table 3.1, together with the corresponding values of the other three models. The bond length in these models ($\sim$1.78 Å) is slightly longer than the experimental value (1.74 Å, Ref. [17]), an effect that should be attributed to our setup for the description of the electronic structure [37] (cf. App. B). The O-Ge-O angle distribution of Model I is centered around the tetrahedral angle with a standard deviation of $\sim 6°$. The O-Ge-O angle distribution of the other models show the same mean value. The standard deviations are also similar, except for Model III which evidently suffers from the absence of a thermalization step in the generation procedure.

Table 3.1: Structural properties of our models of vitreous GeO$_2$: the number of atoms (N), the average Ge-O-Ge angle, the average O-Ge-O angle, and the average bond length (d_{GeO}). The respective standard deviations are given in parentheses. Experimental estimates for the angles and the bond lengths are taken from Refs. [14] and [110], respectively.

	N	$\angle$ Ge-O-Ge	$\angle$ O-Ge-O	d_{GeO} (Å)
Model I	168	135.0° (10.6°)	109.4° (5.8°)	1.780 (0.014)
Model II	72	127.0° (12.3°)	109.4° (5.7°)	1.770 (0.015)
Model III	72	121.3° (9.9°)	109.5° (8.9°)	1.775 (0.020)
Model IV	36	130.2° (10.9°)	109.4° (6.4°)	1.771 (0.011)
Expt.		133°	109.4°	1.73

To address the degree of distortion in the GeO$_4$ tetrahedra, we compared the bond-length and bond-angle distributions in Fig. 3.2 with those of the Model I of v-SiO$_2$ (Sec. 2.1). This comparison shows that the relative bond-length distribution in v-GeO$_2$ and v-SiO$_2$ is similar. However, the bond-angle distribution of v-GeO$_2$ is noticeably broader than that of v-SiO$_2$, indicating that the tetrahedra in the former case show a larger departure from the ideal geometry. This property is conveniently illustrated by introducing the distortion parameter δ_V. This parameter is defined for each tetrahedron as the ratio between its volume and the volume of the ideal tetrahedron with the same average bond-length. In our models of v-GeO$_2$, the ratio δ_V is always found to be smaller than 1.0. We found that the distribution of δ_V for v-GeO$_2$ is significantly broader than the corresponding distribution for v-SiO$_2$ (Fig. 3.3).

Medium-range order

In this section, we analyze structural properties on length scales beyond that of the single tetrahedron. We describe the connectivity between tetrahedra by focusing on the Ge-O-Ge bond-angle distribution and the ring statistics [15].

As shown in Fig. 3.4, the Ge-O-Ge angle distribution differs markedly from one model to the other. In particular, the distribution of Model I shows an average value of $135°$ and a standard deviation of $10.6°$, in good agreement with parameters extracted from diffraction data ($133°$, $8.3°$) [14]. The other models show distributions with lower mean values, ranging between $120°$ and $130°$. The main parameters of these distributions are summarized in Table 3.1.

Figure 3.5 shows the ring statistics for our model structures. The four model structures agree in indicating the six-membered ring as the dominant ring size. However, significant
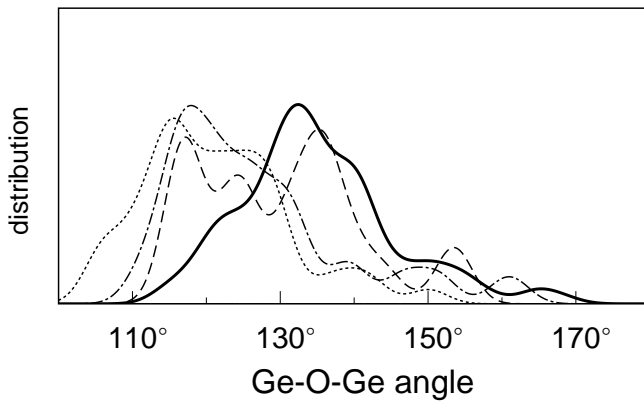
Figure 3.4: Distribution of the Ge-O-Ge intertetrahedral angle for our four models of v-GeO$_2$: Model I (solid), Model II (dot-dashed), Model III (dotted), and Model IV (dashed). A Gaussian broadening of 2.5° is used.

differences between the models occur for smaller ring sizes. It is particularly interesting to focus on three-membered rings, the smallest ring size found in our models. Model I contains four three-membered rings. Model II and Model III have two and five of such rings, respectively. No three-membered ring is found in Model IV. The three-membered rings are quasi-planar, as can be inferred from the sum Σ over all bond angles in the ring. In Model I, Σ averages to 696°, only slightly lower than the ideal value of 720°. In the smaller Models II and III, Σ averages to 687.2° and 691.7°, respectively, only slightly lower than for Model I. The planarity in three-membered rings is driven by the fact that the average Ge-O-Ge angles in such rings (123° in Model I) is considerably lower than the average Ge-O-Ge in v-GeO$_2$ (133°, Ref. [14]). In the planar configuration, these angles are maximized [99].

It is also worthy of note that models with similar Ge-O-Ge angle distributions do not necessarily show similar ring statistics. Model II and Model III show very similar Ge-O-Ge angle distributions, with a large weight in the range between 110° and 130°. However, their ring statistics differ markedly for three- and four-membered rings (Fig. 3.5). On the other hand, Model I and Model II share similar ring statistics, but their Ge-O-Ge angle distributions show considerably different parameters (Table 3.1).

Pair correlation functions

In Fig. 3.6, we give the pair-correlation functions, $g_{\text{GeO}}(r)$, $g_{\text{GeGe}}(r)$, and $g_{\text{OO}}(r)$, calculated for Model I as explained in Sec. 2.2.1. The first peak of $g_{\text{GeO}}(r)$ is located at 1.77 Å and agrees closely with the Ge-O bond length (Table 3.1). From a spherical integration of $g_{\text{GeO}}(r)$ up to its first minimum at 2.25 Å [69], we derive an average coordination number of 4.01, consistent with the absence of coordination defects in our model. The first peaks of $g_{\text{GeGe}}(r)$ and $g_{\text{OO}}(r)$ correspond to Ge-Ge and O-O distances of 3.25 Å and 2.88 Å, respectively.
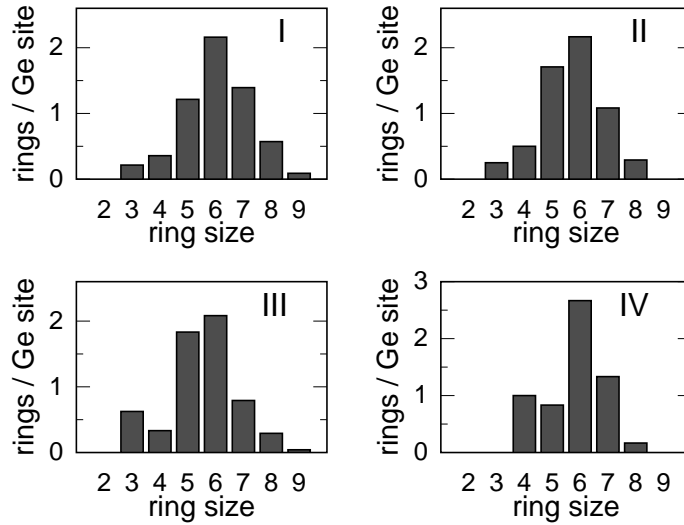
Figure 3.5: Ring statistics of our four models of v-GeO$_2$ according to the minimal path analysis [15].

The ratio between the positions of the first peaks in $g_{\mathrm{GeO}}(r)$ and $g_{\mathrm{OO}}(r)$ gives another measure of the degree of distortion. For Model I, this ratio is 0.6154, in good agreement with the experimental value of 0.6141 estimated from neutron diffraction [111]. For comparison, this ratio is equal to $\sqrt{3/8} \simeq 0.6124$ for the ideal tetrahedron.

Neutron diffraction data are often presented in the form of the neutron total correlation function $T_{\mathrm{N}}(r)$, which can be expressed in terms of the pair correlation functions [17]:

$$T_{\mathrm{N}}(r) = 4\pi\rho\,r \cdot \sum_{\alpha\beta} c_\alpha c_\beta b_\alpha b_\beta\, g_{\alpha\beta}(r), \tag{3.1}$$

where $c_\alpha = N_\alpha/N$ and b_α are the concentration and the neutron scattering length of species α, and ρ is the number density of the sample. For comparison with experiments, it is necessary to take into account the experimental resolution in real space, expressed by the reduced neutron peak function $P(r)$ [17]:

$$T'_{\mathrm{N}}(r) = N_{\mathrm{uc}} \cdot \int_0^\infty T_{\mathrm{N}}(x) \left\{ P(r-x) - P(r+x) \right\} dx, \tag{3.2}$$

where N_{uc} is the number of atoms in the unit of composition ($N_{\mathrm{uc}} = 3$ for GeO$_2$). Figure 3.6(b) gives $T_{\mathrm{N}}(r)$ calculated for Model I. The first peak of $T_{\mathrm{N}}(r)$ corresponds to the first peak of $g_{\mathrm{GeO}}(r)$ and is located at 1.77 Å. The second and third peaks of $T_{\mathrm{N}}(r)$ correspond to the first peaks in $g_{\mathrm{OO}}(r)$ and $g_{\mathrm{GeGe}}(r)$ and are found at 2.92 Å and 3.27 Å, respectively, slightly shifted with respect to the partial pair correlation functions because of the multiplicative factor r in Eq. (3.1). As shown in Fig. 3.6(b), $T_{\mathrm{N}}(r)$ and $T'_{\mathrm{N}}(r)$ are essentially indistinguishable beyond the first narrow peak located at 1.77 Å. The experimental broadening introduced by the peak function causes the first peak to decrease to half its height,
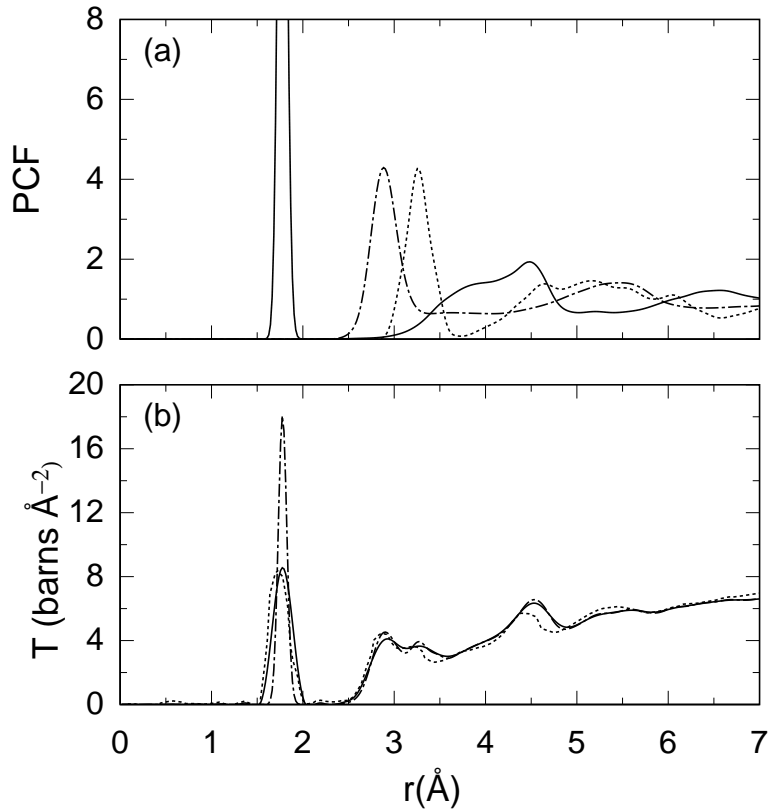
Figure 3.6:   (a) Pair-correlation functions (PCF) $g_{\mathrm{GeO}}(r)$ (solid), $g_{\mathrm{GeGe}}(r)$ (dotted), and $g_{\mathrm{OO}}(r)$ (dot-dashed), calculated in the harmonic approximation for v-GeO$_2$ (Model I). (b) Theoretical neutron total correlation function $T_{\mathrm{N}}(r)$ (dot-dashed). Its counterpart $T'_{\mathrm{N}}(r)$ (solid) accounts for the experimental resolution and permits comparison with experiment (dotted) [112].

which is essential to find good agreement with the experimental correlation function [112].

3.2.2   Reciprocal-space properties

Total structure factor

We calculated the total neutron structure factor of Model I through Eq. (2.5) with neutron scattering lengths of $b_{\mathrm{Ge}} = 8.1929$ fm and $b_{\mathrm{O}} = 5.805$ fm [113]. In Fig. 3.7(a) we compare the calculated neutron static structure factor $S(Q)$ of Model I with experiment [114]. Because of the slight overestimation ($\sim$ 2%) of the Ge-O bond length in the simulation (cf. Table 3.1), we compare the experimental and theoretical structure factors by plotting them vs the adimensional scattering vector Qd_{GeO}. We find overall excellent agreement. In particular, Model I describes well the first sharp diffraction peak that is generally taken as a signature of intermediate range order [115, 116]. Our structural model can also be compared with x-ray diffraction data [115]. The x-ray structure factor is calculated by using Eq. (2.5).

We note that the use of Eq. (2.5) for x-ray diffraction implies the approximation that the electron density results from a superposition of electron densities of isolated atoms. In Fig. 3.7(b), we compare the x-ray structure factor calculated for Model I with its experimental counterpart [117]. As for the neutron structure factor, theoretical and experimental peak positions are in good agreement. In particular, the first sharp diffraction peak and the peak at $Qd_{GeO} \sim 4.5$ show a stronger intensity than in the neutron structure factor [cf. Fig. 3.7(a)], in accord with the experimental trend [115]. This behavior results from the important contribution of Ge-Ge correlations, which carry a larger weight in the x-ray structure factor. Incidentally, this behavior is quite different in vitreous silica, where the corresponding peak at ~ 2.5 Å^{-1} in the x-ray structure factor is very weak as it is shown in Fig. 2.6(b). This is because Si-Si correlations in the x-ray structure factor of v-SiO$_2$ are weaker than the corresponding Ge-Ge correlations. Finally we remark that the quality of the agreement with the experimental x-ray data is very good, as much as with the neutron data, both for v-SiO$_2$ [Fig. 2.6(b)] and v-GeO$_2$ [Fig. 3.7(b)].
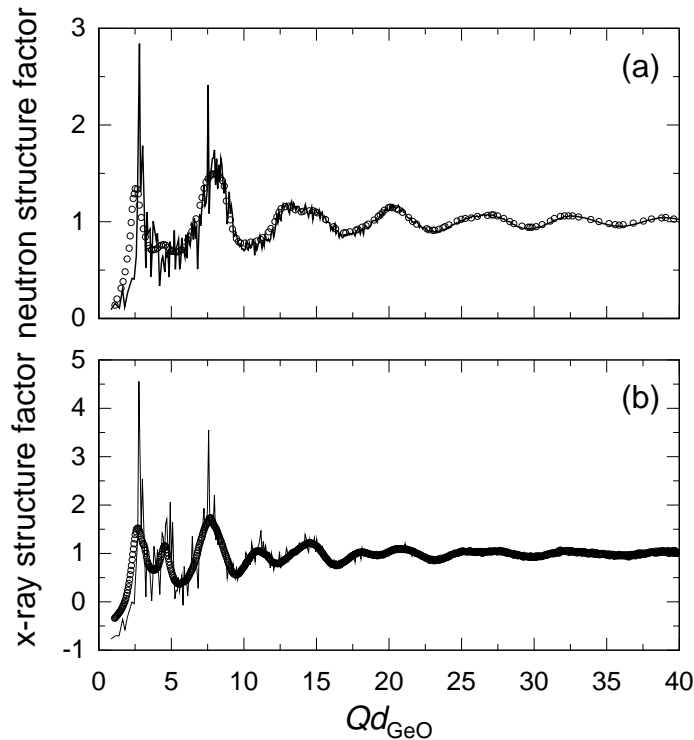

Figure 3.7: (a) Calculated (Model I, solid) and measured (circles) [114] neutron static structure factor of v-GeO$_2$ at room temperature. (b) Theoretical total x-ray structure factor (solid) for Model I of v-GeO$_2$, compared with its experimental counterpart (circles) [114]. The structure factors are given as a function of an adimensional scattering vector, scaled by the average Ge-O bond distance d_{GeO} ($d_{GeO}^{expt} = 1.73$ Å, $d_{GeO}^{theo} = 1.78$ Å).

Partial structure factors

Vitreous GeO$_2$ is a material for which all the partial structure factors have been obtained experimentally. In Fig. 3.8, we carry out the comparison between our theoretical results and available experimental data [117] in the Faber-Ziman formulation [Eqs. (2.10)–(2.12)]. The agreement between theory and experiment is very impressive. In particular, the first sharp diffraction peak is well reproduced in each of the partial strucutre factors.

In fundamental glass science, it is currently of interest [80] to understand the decomposition of the FSDP in partial structure factors according to the Bhatia-Thornton formulation (BT) [78]. The BT structure factors [Eqs. (2.13)–(2.15)] distinguish between fluctuations
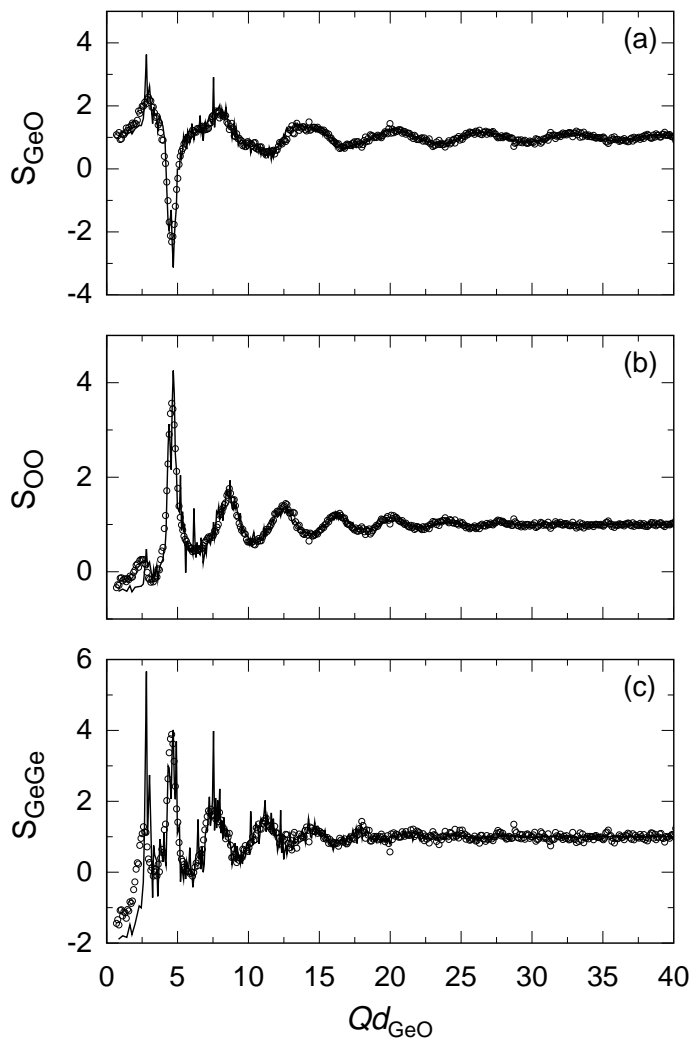
Figure 3.8: Theoretical Faber-Ziman partial structure factors (solid) for Model I of v-GeO$_2$, compared with experimental data (circles) of Ref. [117]: (a) $S_{\mathrm{GeO}}(Q)$, (b) $S_{\mathrm{OO}}(Q)$, and (c) $S_{\mathrm{GeGe}}(Q)$. The scattering vector is scaled as described in Fig. 3.7.

of number density and of concentration, resulting in the following partial structure factors: $S_{NN}(Q)$ (number-number), $S_{NC}(Q)$ (number-concentration), $S_{CC}(Q)$ (concentration-concentration). In this way, separate information is provided on topological and chemical order, through $S_{NN}(Q)$ and $S_{CC}(Q)$, respectively. In Fig. 3.9, the calculated BT structure factors are compared with corresponding experimental data [117]. The agreement between theory and experiment is excellent for all the three BT structure factors. Furthermore, in relation with an on-going debate in the literature [80, 118], it is interesting to note that both the theoretical and experimental results show the appearance of a small FSDP in the S_{CC}. The origin of this peak is not yet clarified. However, we remark that it is not related to the occurrence of coordination defects, since these are absent in our model.
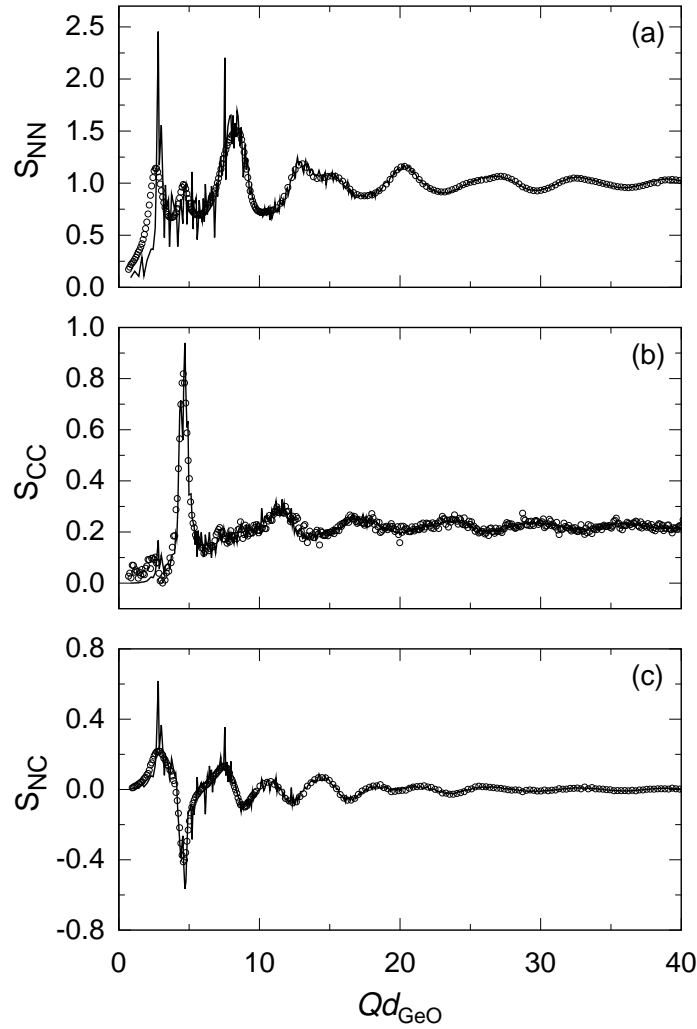

Figure 3.9: Theoretical Bhatia-Thornton partial structure factors (solid) for Model I of v-GeO$_2$, compared with experimental data (circles) of Ref. [117]: (a) $S_{NN}(Q)$, (b) $S_{CC}(Q)$, and (c) $S_{NC}(Q)$. The scattering vector is scaled as described in Fig. 3.7.

We also compared our theoretical results with the experimental data in Ref. [110] (not shown). This comparison shows a less impressive agreement, particularly in the region of the first sharp diffraction peak.

3.2.3   The FSDP in the total structure factor and in the S_{CC}

We here apply to the case of v-GeO$_2$ the same analysis of the FSDP in terms of intra- and intertetrahedral correlations, carried out in Chapter 2 for v-SiO$_2$. In Fig. 3.10, we show the decomposition of the neutron structure factor $S(Q)$ of Model I. The maximum in the total $S(Q)$ is located at 1.58 Å^{-1}, in close agreement with the experimental position $\sim$1.6 Å^{-1}. For $Q \geq 3$ Å^{-1}, the intratetrahedral term follows closely the total structure factor apart from small discrepancies that tend to disappear for increasing Q values [79]. In this range of Q vectors, the intertetrahedral term is oscillating around zero, and it vanishes as Q increase. For $Q \leq 3$ Å^{-1}, the intratetrahedral term decreases and presents a minimum at $Q \sim 1.8$ Å^{-1} and then diverges for small Q vectors. The intertetrahedral term, instead, shows a maximum at the FSDP position $\sim$1.58 Å^{-1} and it decreases quickly for $0 < Q \leq 1.8$ Å^{-1}. This decomposition shows how the FSDP in vitreous germania arises from the competition of two terms one related to the basic tetrahedral unit and the other related to medium-range order contained into the intertetrahedral term. We carried out the same
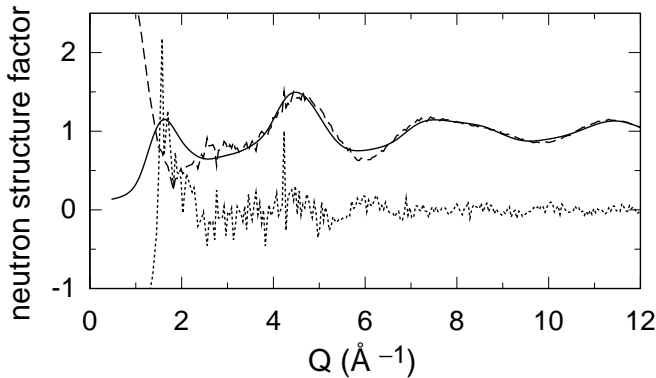

Figure 3.10: Theoretical total neutron structure factor calculated for Model I of v-GeO$_2$ (solid) at room temperature, and its decomposition into intratetrahedral (dashed) and intertetrahedral terms (dotted). For clarity, we applied a smoothening procedure to the total structure factor. A Gaussian broadening of 0.25 Å^{-1} is used (cf. App. A).

decomposition in intra- and intertetrahedral correlations for the $S_{\mathrm{CC}}(Q)$ (Fig. 3.11). As seen for the total $S(Q)$, the behavior for $Q \geq 3$ Å^{-1} is mainly given by the intratetrahedral term, while for lower Q values it is the intertetrahedral term that is dominant. Unlike the case of v-SiO$_2$, this decomposition shows that the two terms do not sum up identically to zero in the range of $Q \leq 2$ Å^{-1}. In particular a trace of the FSDP is visible in both the total $S_{\mathrm{CC}}(Q)$ and in the intertetrahedral term, while there is no signature of it in the intratetrahedral term.

We further analyse the intertetrahedral term by considering the correlations between

each individual tetrahedron and the rest of the network. In this way we get information on the dependence of the FSDP on the local environment of a tetrahedron. In Fig. 3.12 we show the distribution of the contributions to FSDP intensity given by individual tetrahedra. The distribution shows a Gaussian-like shape, therefore the appearence of the FSDP in the $S_{CC}(Q)$ results from the average over all tetrahedra, rather than from specific tetrahedra located in special environment.
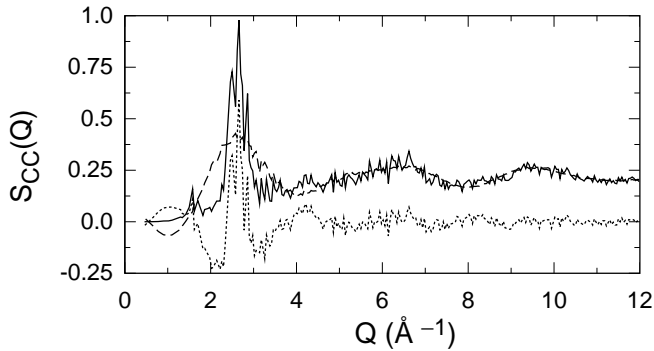

Figure 3.11: Concentration-concentration structure factor in the Bhatia-Thornthon formalism calculated for Model I of v-GeO$_2$ (solid) at room temperature, and its decomposition into intra-tetrahedral (dashed) and inter-tetrahedral terms (dotted).
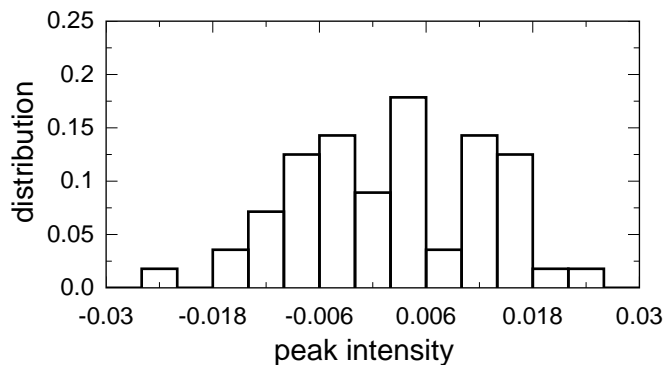

Figure 3.12: Distribution of the contributions to FSDP intensity of the inter-tetrahedral $S_{CC}(Q)$ given by individual tetrahedra.

3.3   Vibrational properties

We perform in this section the analysis of the v-DOS in terms of the vibrational eigenmodes. In Fig. 3.13, the v-DOS is decomposed according to the weights of the O and Ge species [Eq. (2.23)]. Figure 3.13(a) shows that the ratio between the O and Ge weights is close to the concentration ratio in the range 150-700 cm^{-1}. Below 150 cm^{-1} this ratio approaches 1:1, while it increases to 5:1 above 700 cm^{-1}. This implies that the motions of the two species are strongly correlated up to 700 cm^{-1}, particularly below 150 cm^{-1}. At variance, the correlation above 700 cm^{-1} is significantly weaker, since the contribution of the heavier Ge atoms becomes less important in the high-frequency range. At variance with

the case of v-SiO$_2$ which shows a peak with dominant cation weight at $\approx$800 cm^{-1}, such a peak does not occur in the v-DOS of v-GeO$_2$. This should be related to the higher Ge mass which causes a shift of this band to lower frequencies thereby favoring the interaction with O modes.
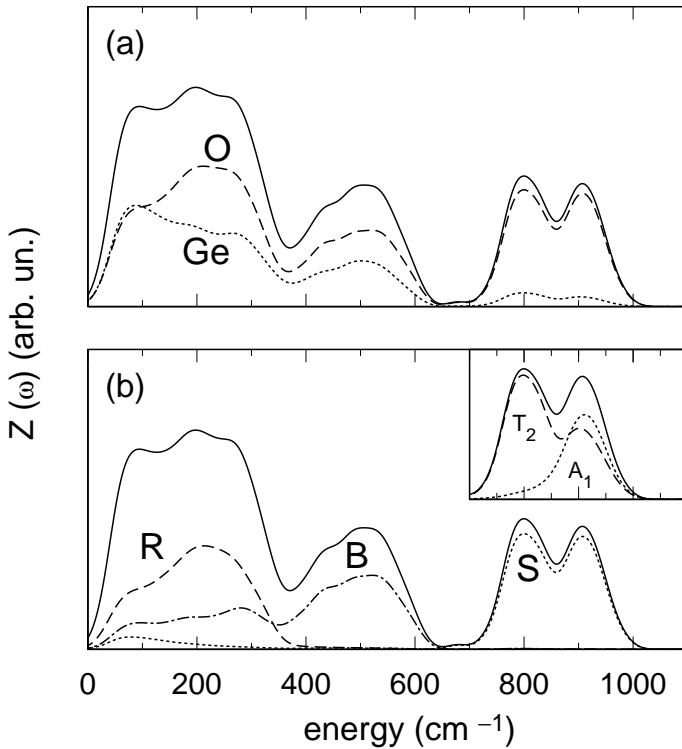

Figure 3.13: Vibrational density of states $Z(\omega)$ (solid) and its decompositions. In (a), $Z(\omega)$ is first decomposed into O and Ge weights. In (b), the O weight is further decomposed according to the O motion along the rocking (R, dashed), bending (B, dot-dashed) and stretching (S, dotted) directions. Inset: Projection on symmetry-adapted modes of the GeO$_4$ tetrahedra: T$_2$ (dashed) and A$_1$ (dotted). A Gaussian broadening of 19 cm^{-1} is used.

We further decomposed the oxygen contribution to the v-DOS according to three orthogonal directions defining the local environment of the O atoms [Fig. 3.13(b)] [60]. The principal directions associated to the Ge-O-Ge bridge define the rocking, bending and stretching directions, respectively [35]. The lowest vibrational band ($<$ 380 cm^{-1}) prevalently features O rocking motions, while the band extending from 380 to 700 cm^{-1} is mainly composed of O bending motions. The decomposition in Fig. 3.13(b) shows that the vibrational modes above $\sim$700 cm^{-1} are mostly given by O stretching motions. The stretching contribution features a double peak, very similar to vitreous silica [85]. To address this splitting, it is convenient to organize the stretching modes according to the irriducible representations of the tetrahedron A_1 and T_2 [35]. The A_1 mode corresponds to an in-phase motion of the four O atoms towards the central Ge atom. In the T_2 modes, two O atoms move closer to the central Ge atom, while the other two move away. By projecting on A_1 and T_2 representations, we show that also for v-GeO$_2$ this doublet stems from distinct vibrational modes of the tetrahedra (Fig. 3.13, inset). Therefore, the origin of this splitting should not be assigned to a longitudinal-optic/transverse-optic (LO-TO)

effect [35].

In Fig. 3.14 we show the inelastic dynamic structure factor compared to the experimental results of Ref. [87]. We register an overall good agreement, with the theoretical result reproducing the oscillations of the experimental curve, although with a smaller amplitude. This might arise from finite-size limitations of our model. We show also in in Fig. 3.14 the incoherent approximation from Ref. [87] together with the theoretical curve (solid) obtained for Model I and calculated by Eq. (2.27).
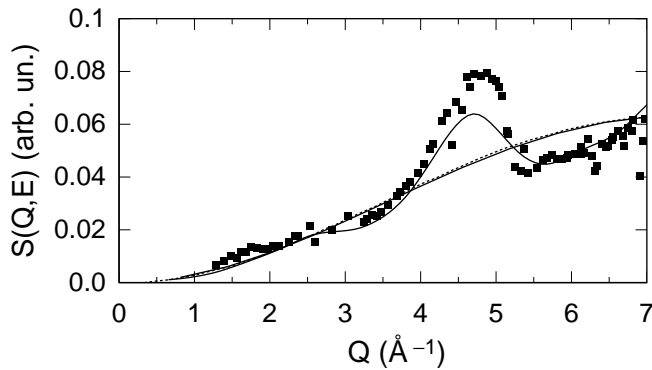

Figure 3.14: Comparison of the experimental inelastic dynamic structure factor in the Boson peak region (2 to 6 meV, squares) [87] and our theoretical calculation (solid). The incoherent approximation from Ref. [87] is also shown and compared to the theoretical curve (solid) obtained for Model I.

Experimental access to the v-DOS is nontrivial. The experimental spectrum which most closely resembles the v-DOS is the inelastic neutron spectrum [85, 74].

In Fig. 3.15, the calculated neutron vibrational density of states is compared to available experimental data [90, 20]. Overall, the comparison is very satisfactory with the theoretical spectrum showing all the salient experimental features. However, the calculated frequencies appear to systematically underestimate the measured ones, an effect that should be attributed to our DFT setup (cf. Appendix B).

We also compare the theoretical inelastic neutron spectrum to the actual v-DOS (Fig. 3.16). The comparison shows that the two spectra differ only slightly. The main differences concern the intensities in the low and high frequency bands, below 300 cm^{-1} and above 700 cm^{-1}, respectively.

The vibrational frequencies and modes also give access to the vibrational amplitudes [70]. For our model of v-GeO$_2$ and for a temperature of 300 K, we obtained mean square displacements for O and Ge atoms of 0.26 and 0.16 Å, respectively. These values are slightly higher than found for v-SiO$_2$ (0.21 Å for O and 0.14 Å for Si, cf. Ref. [70]) and reflect the higher density of soft phonon modes in v-GeO$_2$. For the fluctuations of Ge-O bond lengths at 300 K, we found 0.045 Å. This is very close to an experimental estimate obtained from neutron diffraction (0.042 Å, Ref. [111]), indicating that structural disorder only marginally affects the fluctuations of the Ge-O bond-length.
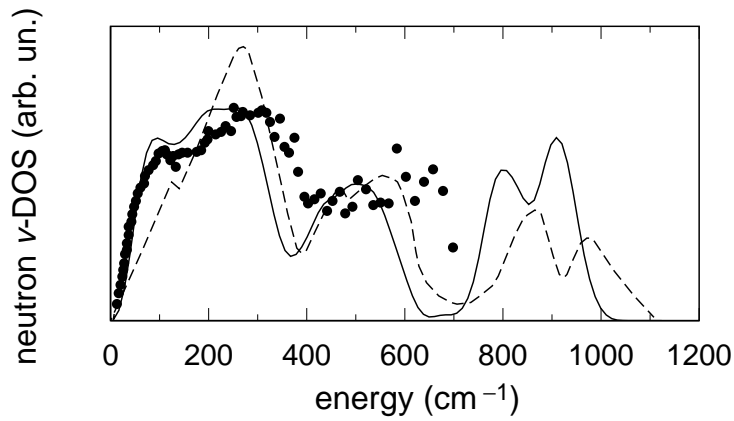
Figure 3.15: Calculated (Model I, solid) neutron vibrational density of states (v-DOS) of v-GeO$_2$ at room temperature, compared to corresponding experimental data from Refs. [90] (disks) and [20] (dashed). The experimental data were scaled with respect to the calculated curve: the former to match the height of the highest peak, while the latter to show the same integrated area. In the calculation of the spectrum [35], we used transferred momenta in the range 0.5–4.5 Å^{-1} [90].
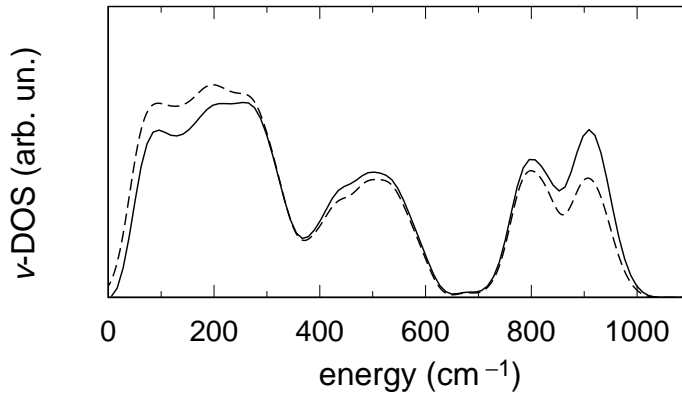

Figure 3.16: Calculated neutron vibrational density of states (v-DOS) of v-GeO$_2$ (solid) at room temperature compared to the actual v-DOS (dashed). In the calculation of the neutron spectrum [35], we used transferred momenta [90] in the range 0.5–4.5 Å^{-1}.

3.4 Infrared Spectra

3.4.1 Born charge tensors

The Born charge tensors Z^* were calculated for all O and Ge atoms in Model I. Because of the local tetrahedral symmetry around the Ge atoms, the average Z^* tensors for the Ge atoms are essentially isotropic. For these atoms, we calculated an average isotropic charge of 3.44 with a standard deviation of 0.14. We represent the O tensor within a local reference set based on the orientation of the Ge-O-Ge bond. We take the x direction along
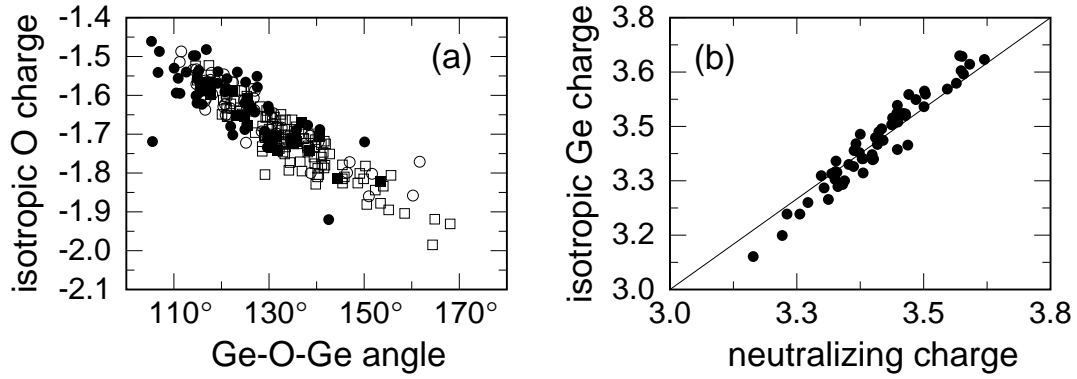
Figure 3.17: (a) Isotropic oxygen Born charge vs Ge-O-Ge angle for our four models of v-GeO$_2$: Model I (open squares), Model II (open disks), Model III (filled disks), and Model IV (filled squares). (b) local dynamical charge neutrality property in v-GeO$_2$: isotropic Ge charge vs neutralizing charge defined as half of the total charge of the O nearest neighbors of the germanium Ge.

the bisector of Ge-O-Ge angle, the y direction normal to the plane of the Ge-O-Ge bridge, and the z direction orthogonal to the previous two. The average Z^* for O atoms reads:

$$Z^*_{\mathrm{O}} = \begin{pmatrix} -1.12 & 0.00 & -0.02 \\ 0.00 & -1.05 & -0.03 \\ 0.00 & 0.01 & -2.99 \end{pmatrix}. \tag{3.3}$$

This average tensor is almost diagonal, with diagonal values typical for O bridge structures [92, 3]. In particular, for the displacements along the stretching direction (z direction) the coupling is noticeably stronger. This is related to the fact that such displacements involve a much larger charge transfer [119, 92]. The distribution of the isotropic Born charge has an average value of -1.72 and a width of 0.09. The properties of the isotropic Born charge distributions of our models are summarized through their averages and widths in Table 3.2. The differences between the models are consistent with their Ge-O-Ge bond-angle distributions (Fig. 3.4 and Table 3.1). In Fig. 3.17(a), we correlate the isotropic O Born charge with the corresponding Ge-O-Ge angle. The Born charge is found to decrease with increasing bond angle. A similar trend was also observed for v-SiO$_2$ [3]. The isotropic Ge Born charges also depend on the Ge-O-Ge bond-angles through a local dynamical charge neutrality property [Fig. 3.17(b)], which is found to be respected in v-GeO$_2$ to a similar extent as in v-SiO$_2$ [3].

3.4.2 Dielectric tensor

We calculated the high-frequency dielectric tensors ϵ_∞ [Eq. (2.32)] for our models of v-GeO$_2$ through second derivatives of the energy with respect to the electric fields [47, 48].

The dielectric tensor calculated for Model I is almost isotropic, as expected for an amorphous system [83]:

$$\boldsymbol{\epsilon}_\infty = \begin{pmatrix} 2.81 & -0.03 & 0.00 \\ -0.03 & 2.78 & -0.04 \\ 0.00 & -0.04 & 2.77 \end{pmatrix}. \tag{3.4}$$

From the isotropic part of the dielectric tensor $\epsilon_\infty = \mathrm{Tr}(\boldsymbol{\epsilon}_\infty)/3$, we obtained an average dielectric constant of 2.79, only slightly larger than the experimental value of 2.58 (Ref. [120]).

We evaluated the static dielectric constant using the calculated oscillator strengths and vibrational frequencies [Eq. (2.35)]. For Model I, we obtained $\epsilon_0 = 6.28$. For comparison, we report in Table 3.2 also the dielectric constants calculated for Models II to IV. The high-frequency dielectric constants of these other models is generally smaller than for Model I, because of finite-size effects associated to their smaller size [121].

Table 3.2: High frequency (ϵ_∞) and static dielectric constants (ϵ_0) for Models I to IV of vitreous GeO$_2$. Average isotropic Born charge for O (Z_O^*) and Ge (Z_Ge^*), together with the standard deviations of their respective distributions (in parentheses).

	ϵ_∞	ϵ_0	Z_O^*	Z_Ge^*
Model I	2.79	6.28	-1.72 (0.09)	3.44 (0.14)
Model II	2.53	6.65	-1.65 (0.09)	3.29 (0.12)
Model III	2.50	6.56	-1.61 (0.08)	3.21 (0.11)
Model IV	2.57	6.11	-1.68 (0.08)	3.36 (0.07)

3.4.3 Dielectric function

The real $\epsilon_1(\omega)$ and imaginary $\epsilon_2(\omega)$ parts of the dielectric response function and the energy loss function have been calculated as explained in Chapt. 2.

In Figure 3.18, we compare the calculated dielectric function ϵ_2 and the energy loss function $-\mathrm{Im}(1/\epsilon)$ of Model I with available experimental spectra [20], finding overall good agreement. In particular, the relative intensities of the three main peaks are well reproduced and their LO-TO splittings show fair agreement with experiment. The difference between calculated and measured peak frequencies is similar as for the neutron vibrational density of states (Fig. 3.15). We found longitudinal-optic/transverse-optic splittings of 62, 46, and 150 cm^{-1} for the three main peaks, in fair agreement with the experimental values of 69, 39, and 116 cm^{-1} [19, 20].
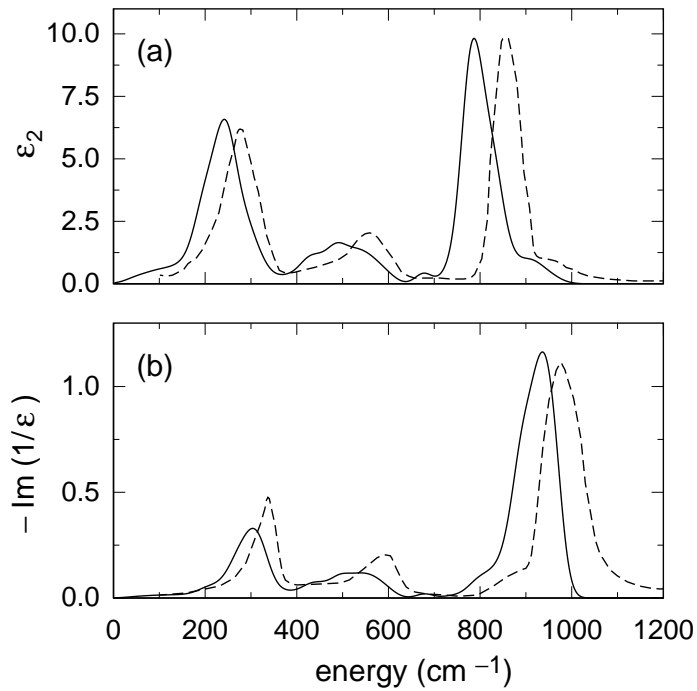
Figure 3.18:   Comparison between calculated (Model I, solid) and measured [20] (dashed) infrared spectra of v-GeO$_2$, for (a) the imaginary part of the dielectric function and (b) the energy loss function. A Gaussian broadening of 19 cm^{-1} was used.

In Fig. 3.19, we show the real and imaginary parts of the dielectric function calculated for Models I to IV. The four models give spectra with a similar overall shape. This similarity stems from the common short-range order which dominates the infrared spectra [4]. However, in the central band ranging between 400 cm^{-1} and 700 cm^{-1}, we observe minor differences between the models. In both ϵ_1 and ϵ_2, Model I gives features which are shifted towards lower frequencies by ~ 50 cm^{-1} with respect to those of Models II to IV. These features correspond to O bending modes and their frequencies decrease with increasing Ge-O-Ge bond angle [102]. Hence, information concerning the bond-angle distribution can be gained from the location of the peak at 550 cm^{-1} in the experimental ϵ_2. The frequency of this peak in Model I is found to slightly underestimate the experimental one, while all other models give higher frequencies. In consideration of the overall lower frequencies in our simulation [37], this result further indicates that the bond-angle distribution of Model I is more reliable than those of the other models.
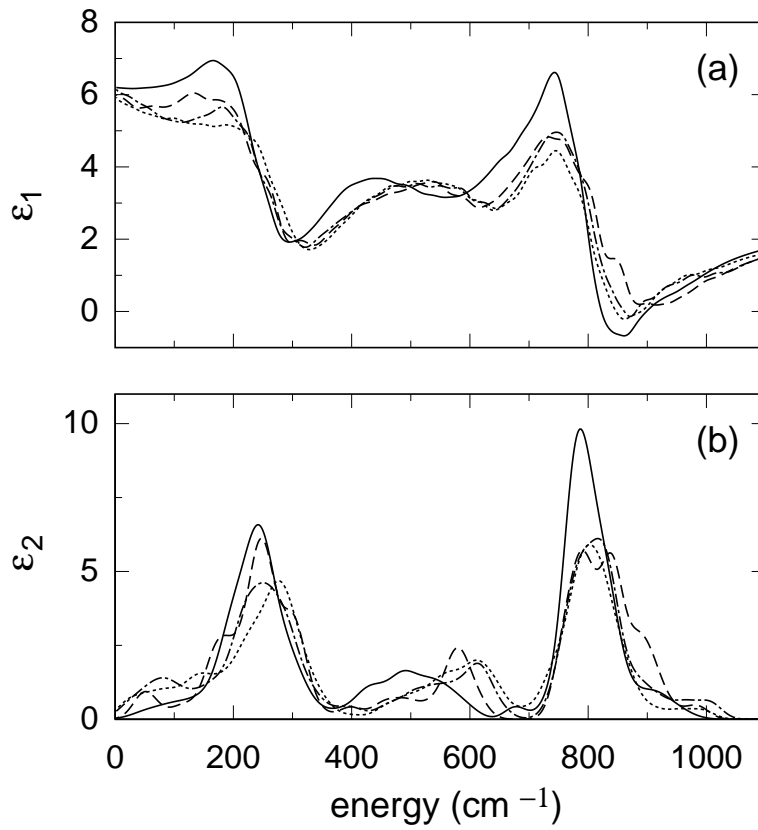
Figure 3.19: (a) Real and (b) imaginary parts of the dielectric function for our four models of v-GeO$_2$: Model I (solid), Model II (dot-dashed), Model III (dotted), and Model IV (dashed). A Lorentzian broadening of 25.7 cm^{-1} is used for the real part, a Gaussian broadening of 19 cm^{-1} is used for the imaginary part.

3.5   Raman scattering

We here calculate Raman spectra through the application of finite electric fields to our periodic model structure [47]. We evaluated the tensor χ_{ij} by numerically calculating second derivatives of the atomic forces with respect to the field. We used electric fields with intensities of $\mathcal{E} = 0, \pm 0.01$ a.u. A description of our methodology is given in Secs. 1.2.1 and 2.7.

Raman spectra were calculated for incoming and outgoing photons with parallel (HH) and perpendicular polarizations (HV) for our four models. We here focused on the reduced Raman spectra, which do not depend on the Bosonic occupation number and thus better highlight the dependence on the coupling tensors. In Fig. 3.20, we compare the reduced HH and HV Raman spectra of Model I with the respective experimental ones [20]. The agreement is excellent. An agreement of comparable quality is recorded for the nonreduced Raman spectra, shown in Fig. 3.21. Apart from an overall shift to lower frequencies [37], the theoretical spectra reproduce well the principal peak and the high frequency doublet. Furthermore, we note that the HH and HV Raman spectra in Fig. 3.20 are scaled by the same factor. Therefore, the comparison also shows that the ratio between the intregrated HH and HV intensities is closely reproduced in our simulation.
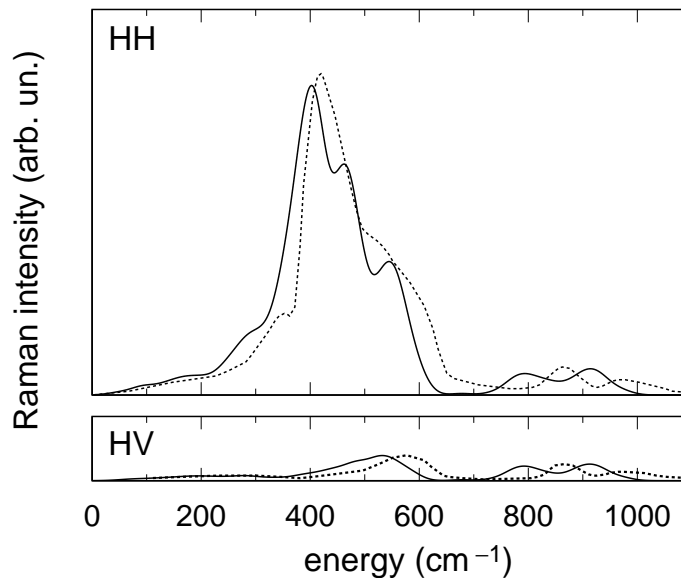

Figure 3.20:   Theoretical reduced HH and HV Raman spectra (solid) for Model I of v-GeO$_2$, compared to corresponding experimental spectra from Ref. [20] (dotted). The theoretical HH spectra is scaled to match the integrated intensity of the experimental spectrum. The same scaling factor is then applied to the HV spectrum. A Gaussian broadening of 19 cm^{-1} is used in the theoretical spectra.
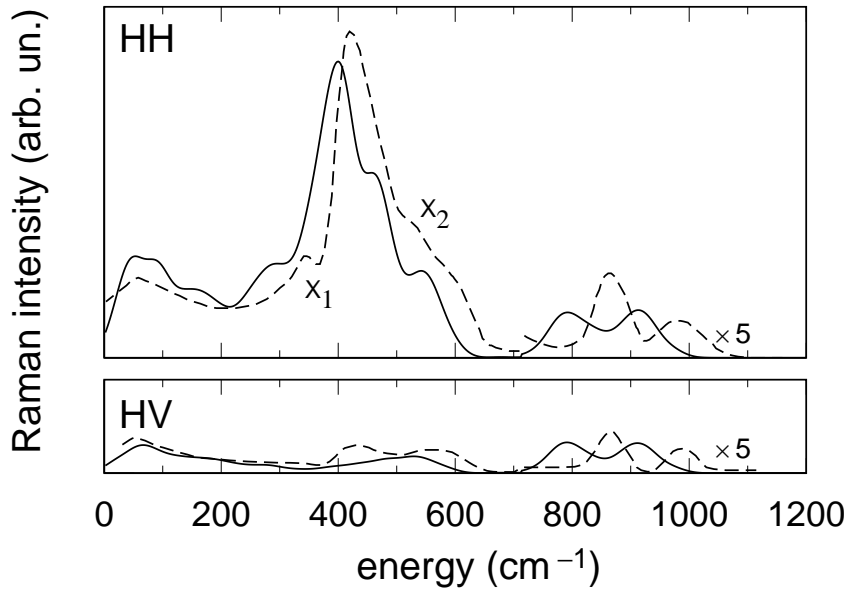
Figure 3.21: Calculated (solid) and measured (dashed, [22]) HH and HV Raman spectra of v-GeO$_2$. The calculated spectra are scaled to match the integrated intensity of the experimental HH spectrum. For clarity, the intensities in the high-frequency range were scaled by a factor of 5. A Gaussian broadening of 19 cm^{-1} was used.

3.5.1   Dependence of HH Raman spectrum on Ge-O-Ge angle

The HH Raman spectrum of v-GeO$_2$ shows a strong dependence on the intermediate range order through the Ge-O-Ge bond angle distribution, as observed previously for v-SiO$_2$ [Fig. 2.18]. Indeed, we find that the HH Raman spectrum is dominated by the coupling to O bending motions. A further analysis reveals that the tensors $\partial\chi/\partial\mathbf{R}$ associated to these motions are almost isotropic. Figure 3.22 shows that the HH Raman spectrum below 700 cm^{-1} is reproduced up to 90% when only the isotropic part of the coupling to O bending motions is accounted for.

The coupling factors f_I [Eq. (2.50)] associated to the O bending motions in Model I show a clear a correlation with the corresponding Ge-O-Ge bond angle θ_I (Fig. 3.23). The observed dependence is consistent with the relation [4]:

$$f_I = (\alpha/3)\cos(\theta_I/2), \qquad\qquad (3.5)$$

which holds for the bond-polarizability model [101] for a system of regular tetrahedral units. A one-parameter least-squared fit gives a value of 101 bohr^2 for the parameter α.

In Fig. 3.24, we illustrate the dependence of the dominant coupling factor on the Ge-O-Ge angle by comparing the HH Raman spectra obtained for the different model structures. It is convenient to discuss these spectra on the basis of the bond-angle distributions given in Fig. 3.4. The spectrum of Model I shows the best agreement with experiment.
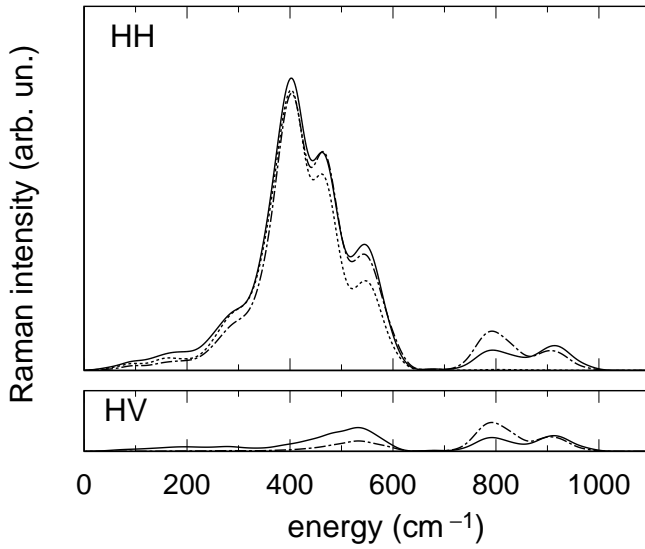
Figure 3.22: Reduced HH and HV Raman spectra (solid) compared to spectra obtained for specific approximations of the coupling tensors, for Model I of v-GeO$_2$. The dotted curve in the HH spectrum corresponds to retaining only the isotropic component of these tensors associated to oxygen bending motions. The dot-dashed curves correspond to the result obtained within the bond-polarizability model with optimal parameters.
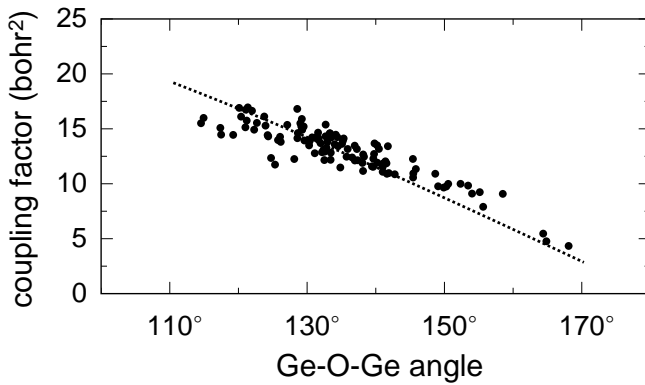

Figure 3.23: Coupling factor f_I vs Ge-O-Ge angle for all O atoms in Model I of v-GeO$_2$ (disks). The curve corresponds to the best fit with Eq. (3.5), obtained for $\alpha = 101$ bohr^2.

This provides support for its Ge-O-Ge bond-angle distribution which has a mean value at 135°. Experimental support for this mean value also comes from diffraction [14] and NMR experiments [122]. The other model structures show bond-angle distributions shifted to lower Ge-O-Ge angles, particularly for Models II and III. Correspondingly, the HH Raman intensity is enhanced in the frequency region between 500 cm^{-1} and 700 cm^{-1}, at higher frequencies than the main peak in Model I, consistent with the relation between bond angle and bending frequency [102]. We note the peculiar behavior in the frequency region around 500 cm^{-1}, where the intensity varies considerably according to the considered model. We defer the discussion of this behavior to Sec. 3.5.2.

3.5.2 Raman shoulders and small rings

In the previous chapter we discussed the Raman spectra of v-SiO$_2$. In particular, in Sec. 2.7.4, we focused on the relation between the two sharp lines D_1 and D_2, and the con-
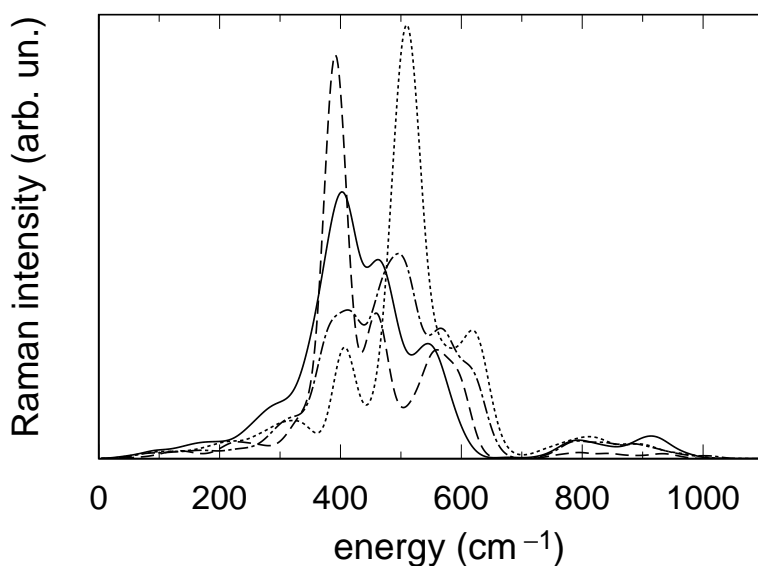
Figure 3.24: HH Raman spectra for our four models of v-GeO$_2$: Model I (solid), Model II (dot-dashed), Model III (dotted), and Model IV (dashed). A Gaussian broadening of $19\,\text{cm}^{-1}$ is used.

centration of small membered rings in vitreous silica. In this section we focus on the role played by small rings in the HH Raman spectrum of vitreous germania. Despite the structural similarity between v-SiO$_2$ and v-GeO$_2$, the HH Raman spectrum of the latter glass does not show any sharp feature. This contrasts with the higher packing density of tetrahedral units and with the lower average bond angle on the O atoms which both suggest a higher concentration of small rings in v-GeO$_2$ [37]. However, the Raman spectrum is characterized by two shoulders known as X_1 and X_2 occurring on either side of the main Raman peak. In analogy with the D_1 and D_2 lines, the X_2 shoulder has tentatively been assigned to three- or four-membered rings on the basis of its behavior under isotopic substitution [22] and neutron bombardment [100]. This assignment received support from calculations on a Bethe-lattice cluster [23]. However, the nature of X_1 has remained more elusive. Isotopic substitution experiments indicate that the vibrations contributing to X_1 mainly involve Ge motion with a modest admixture of O motion [22].

In order to identify the contribution of three-membered rings to the HH Raman spectrum, we projected the vibrational eigenmodes onto O breathing motions in these rings, prior to the calculation of the Raman intensities. For Model I, the Raman projection obtained in this way gives a broad peak in the range from 500 to 550 cm^{-1} [Fig. 3.25(a)]. Similar projections carried out for the other model structures also fall in this frequency range [Fig. 3.25(b)]. The three spectra in Fig. 3.25(b) show a shoulder or second peak close to 600 cm^{-1}. This effect is associated to the overestimated spread of the Ge-O-Ge angles in

the three-membered rings (typical standard deviations between $5°$ and $7°$) and arises from the finite size of our models. Indeed, considering the most planar rings in each of our models, we found that the width of such projections narrows considerably [123], reducing in particular the weight close to 600 cm^{-1}. For our models, this suggests that the average peak position for a planar ring occurs at ≈ 500 cm^{-1}, in fair agreement with the position of the X_2 shoulder [37]. Furthermore, upon ^{16}O $\rightarrow$ ^{18}O substitution, the projection peak for three-membered rings is found to shift by about -26 cm^{-1}, in excellent accord with the experimental shift of -25 cm^{-1} [22, 37]. Hence, our analysis supports the assignment of the shoulder X_2 to oxygen breathing vibrations in three-membered rings.

The intensity of the X_2 shoulder conveys information concerning the concentration of three-membered rings in v-GeO$_2$. To derive an estimate of this concentration, it is instructive to compare the Raman intensities of our models in the frequency region at $\sim$500 cm^{-1} (Fig. 3.24). Model III and to a lesser extent Model II show strong peaks at these frequencies, which stand out with respect to the spectrum of Model I. This relates to the relatively higher concentrations of three-membered rings in these models. Correspondingly, Model IV, in which such rings are absent, shows a clear minimum in this frequency range of the spectrum. The ring statistics in Fig. 3.5 imply that 31% (13%) of the O atoms in Model III (II) belong to such rings, compared to a ratio of 11% in Model I. Comparison with experiment leads to the suggestion that the amount of O atoms belonging to three-membered rings in v-GeO$_2$ situates slightly above 10%. This value is considerably larger than the estimate advanced for v-SiO$_2$ ($\sim$0.22%, Ref. [4]) and indicates that the connectivities of tetrahedra in v-SiO$_2$ and v-GeO$_2$ differ substantially.

The vibrational response of vitreous GeO$_2$ has been recently investigated using an impulsive stimulated Raman scattering technique in the femtosecond regime [124]. The results of these investigations yield evidence for a weak vibrational mode ascribed to oxygen motion in three-membered planar ring structures, thereby confirming our assignment of the shoulder X_2.

To elucidate the origin of the feature X_1 appearing at 347 cm^{-1} in the Raman spectrum of v-GeO$_2$ [22, 23], we first enquired the role of four-membered rings by inspecting the corresponding Raman projections. However, as shown in Fig. 3.25(a), we found that these projections for Model I give their largest contribution in correspondence of the principal Raman peak, without any specific relation to X_1.

To get insight into the kind of vibrational motions involved in the frequency region of X_1, we considered the modes associated to the Ge-O-Ge bridge including the Ge motions. We focused on O bending motions which dominate the Raman spectrum in this frequency range (Fig. 3.22). Searching for associated Ge motions which give maximal Raman projections below 400 cm^{-1}, we found symmetric Ge modes approximately oriented along the
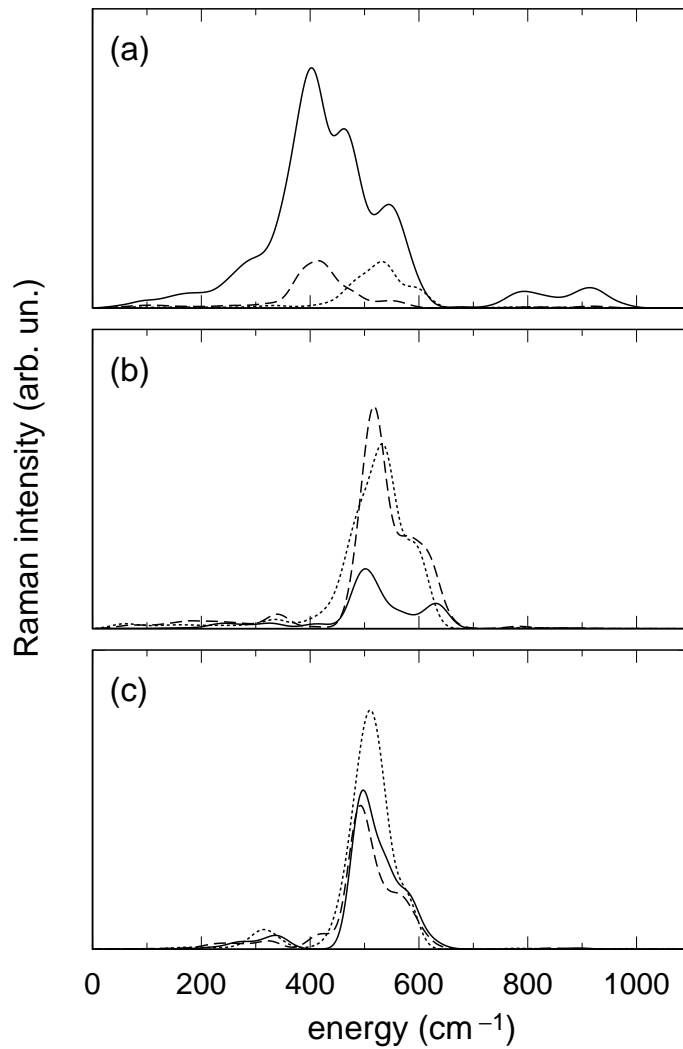
Figure 3.25:   (a) HH reduced Raman spectrum (solid) for Model I of v-GeO$_2$, together with HH Raman spectra obtained for vibrational eigenmodes projected on breathing O vibrations in three- (dotted) and four-membered rings (dashed). (b) Projections as in (a) for three-membered rings belonging to Model I (dotted), Model II (solid), and Model III (dashed). In Model IV these rings are absent. (c) Projections as in (b) but only for the most planar ring in each model. A Gaussian broadening of 19 cm^{-1} is used.
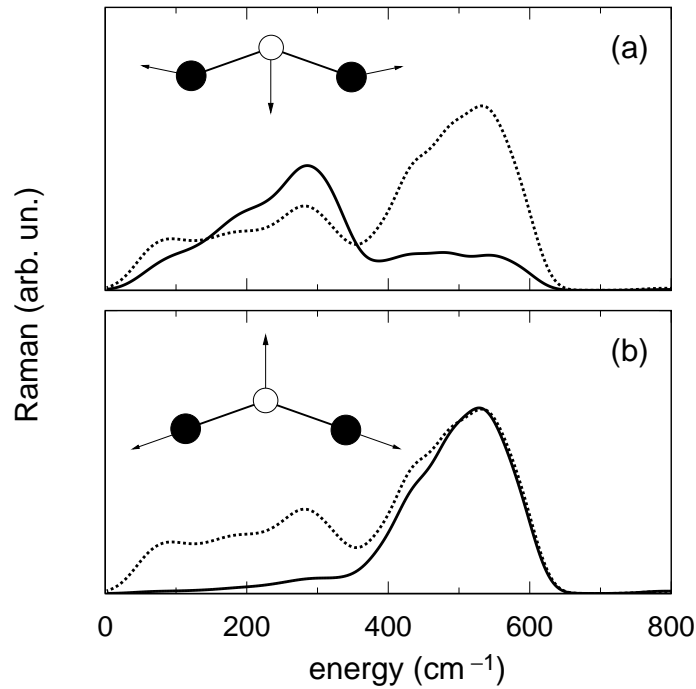
Figure 3.26: Average Raman intensity (solid) obtained for vibrational eigenmodes projected on specific motions of the Ge-O-Ge unit. The average is carried out over all units in Model I of v-GeO$_2$. The illustrated motions correspond to the choices which maximize the intensity in either the (a) low- (below $\sim$350 cm^{-1}) or (b) high frequency band (between 350 and 700 cm^{-1}), corresponding to the B_1 and B_2 motions discussed in the text. The relative weight of Ge and O motions in the B_1 and B_2 motions has been taken to correspond to the relative contribution of the two species in the respective frequency range of the v-DOS (Fig. 3.13). The dotted curve in both panels corresponds to a projection on O bending motions irrespective of the Ge motions.

Ge-Ge direction as depicted in Fig. 3.26 (B_1). The Raman projection averaged over all Ge-O-Ge bridges in Model I is shown in Fig. 3.26. This projection clearly yields an enhanced contribution for frequencies below 350 cm^{-1} in the range of the shoulder X_1. Upon ^{16}O $\rightarrow$ ^{18}O, the main peak of the B_1 mode is found to shift by -7 cm^{-1}, in good agreement with the experimental shift [22] of X_1 (-5 cm^{-1}). We therefore suggest that the X_1 shoulder originates from B_1 modes. Since the Ge-O-Ge bridges form the basic structure of the network, this analysis further suggests that X_1 does not result from vibrations localized on a structural subunit but rather corresponds to diffuse motions throughout the network.

We also searched for coupled O and Ge motions giving maximal projection on the high-frequency side of the bending band. This search yielded symmetric Ge motions oriented along the Ge-O as shown in Fig. 3.26 (B_2). The average Raman projection on B_2 modes gives a dominant contribution between 350 and 700 cm^{-1} with a peak at $\sim$530 cm^{-1}. We note that the breathing motions at the origin of the X_2 shoulder can be pictured as a superposition of B_2 modes localized within three-membered rings.

For comparison, we also show in Fig. 3.26 the average Raman projection on O bending motions irrespective of the associated Ge vibrations. This comparison clearly shows that the bending contribution results from two separate subbands, well represented by B_1 and B_2 vibrations. We also note that the average Raman projection on O bending motions does not differ significantly from the bending contribution to the v-DOS (Fig. 3.13), however focusing on Model I, we note that the HH Raman spectrum differs considerably from the v-DOS, especially below 700 cm^{-1} [102, 125]. In particular, the main Raman peak at 410 cm^{-1} does not occur in correspondence of a peak in the v-DOS. This peak falls very close to the dip at 350 cm^{-1} in the v-DOS, in overall good agreement with the experimental situation [125]. As remarked previously [125], the occurrence of a peak at the edge of the B_2 band is a result of correlations which considerably enhance the Raman intensity. Since the modes in the B_1 band contribute to the Raman spectrum through the same coupling mechanism, we expect that the Raman intensities at the upper edge of this band could also undergo similar enhancements. The spectrum resulting from the combination of these contributions would then give rise to peculiar X_1 shoulder at frequencies slightly lower than the dip in the v-DOS.

3.5.3   Parameters for the bond polarizability model

We determine optimal parameters following the same procedure as for v-SiO$_2$ (Chapt. 2). First, we fixed the parameter α which is responsible for the principal Raman peak, as described in Sec. 3.5.1. Focusing on Model I, the other parameters are then obtained by minimizing the sum of squared differences between the components of the tensor $\partial \boldsymbol{\chi}/\partial \boldsymbol{R}$ calculated within the bond polarizability model and within our first-principles scheme. This results in the following parameters for v-GeO$_2$ (expressed in bohr^2):

$$\alpha = 101.0, \quad \beta = 25.0, \quad \gamma = 1.4. \tag{3.6}$$

It is interesting to compare these values with those obtained for α-quartz following a similar optimization scheme [46]:

$$\alpha = 45.5, \quad \beta = 11.6, \quad \gamma = 3.3, \tag{3.7}$$

expressed in the same units as the values for v-GeO$_2$. The comparison between the absolute values of these parameters clearly indicates that the derivatives of the polarizability for the Ge-O bond are roughly twice as large as those for the Si-O bond. The ratio β/α is similar for the two oxides, whereas there is a more significant difference for γ/α. The latter is however less reliable because of the minor contribution of γ to the tensors $\partial \boldsymbol{\chi}/\partial \boldsymbol{R}$.

In Fig. 3.22, we compare the Raman spectra for Model I calculated within our first principles scheme and within the bond polarizability model with optimized parameters.

Overall, the bond polarizability model reproduces quite faithfully the Raman spectra. The residual differences reflect the limitations of the bond polarizability model. In particular, we found deviations of $\sim 8\%$ for the main Raman peak. This level of accord is consistent with the average deviations of $\sim15\%$ recorded for the bond polarizability model when applied to α-quartz [46].

3.6 Conclusions

In this chapter, we aimed at gaining structural information on a disordered network-forming material such as v-GeO$_2$ through the analysis of its vibrational spectra. We performed a comprehensive investigation involving inelastic neutron, infrared, and Raman spectra. Our approach goes beyond the simple vibrational density of states to model the specific coupling tensors involved in each of the analyzed spectra. To achieve a reliable degree of accuracy, our analysis is carried out within a fully consistent density functional scheme, involving the calculation of vibrational frequencies and eigenmodes, dynamical Born charge tensors, dielectric constants, and Raman coupling tensors.

The present application to v-GeO$_2$ shows that the information contained in the individual vibrational spectra might differ considerably. The inelastic neutron spectrum is shown to reproduce quite accurately the vibrational density of states. The infrared spectra are mainly dependent on the basic structural unit showing a weak dependence on their connectivity in the network. Indeed, various models with similar short-range properties give infrared spectra with only marginal differences. At variance, the Raman spectra is shown to sensitively depend on the intertetrahedral angle distribution, thereby conveying information on the connectivity of tetrahedra in the network. Our study shows that a Ge-O-Ge angular distribution with a mean value of 135° is consistent with the Raman spectrum, in accord with diffraction and NMR experiments. Furthermore, we assign the shoulder X_2 appearing in the Raman spectrum to three-membered rings and provide an estimate of their concentration. The shoulder X_1 is instead attributed to diffuse bending vibrations. Hence, this analysis clearly demonstrates that the combined consideration of various vibrational spectra provides an invaluable tool to reveal the properties of the underlying network structure.

Our approach starts with the generation of viable structural models. Through comparisons between experiment and theory it becomes possible to establish relations between specific features in the spectra and the underlying structures. Understanding the origin of specific features then leads to information on how the model structures should be ameliorated. Application of this methodology in an iterative manner could clearly establish a virtuous cycle in which model structures become progressively more realistic.

Chapter 4

Vibrational spectra of v-GeSe$_2$

In this chapter, we provide a comprehensive analysis of both the structural and vibrational properties of vitreous GeSe$_2$ using a density-funcitional approach. First, we generate model structures according to the two contending structural conceptions outlined in the introduction. For models of either kind of conception, the level of agreement with x-ray [126] and neutron diffraction data [25, 127] is rather similar, confirming the overall weak dependence of this kind of data on the detailed structural arrangements. Then, we address the vibrational properties and focus on the inelastic neutron, infrared, and Raman spectra for all constructed models. Through the comparison of different models, our investigation highlights the relation between the underlying structural arrangements and the principal features in the vibrational spectra. Furthermore, the comparison with experimental spectra gives insight into the atomic structure of vitreous GeSe$_2$. The generated models show important differences in the calculated vibrational spectra, especially for the infrared and Raman ones. This result indicates that the vibrational spectra can successfully be used to discriminate among models. One of the generated models shows overall good agreement with all the experimental vibrational spectra. The atomic structure of this model clearly favors the conception by which the network structure of v-GeSe$_2$ is mainly chemically ordered. The model that best reproduces the experimental vibrational spectra shows 95% of the Ge atoms in regular tetrahedral units. Moreover, our study provides a clear interpretation of the two principal peaks appearing in the Raman spectrum. In particular, the companion line is assigned to edge-sharing tetrahedra.

This chapter is organized as follows. In Sec. 4.1, we describe how we generated our model structures of v-GeSe$_2$. We also describe in this section the technical aspects of our electronic-structure calculations and give the electronic density of states of the largest of our model structures. In Sec. 4.2, we address the structural properties of v-GeSe$_2$ focusing on both real-space and reciprocal-space properties, which include the bond-length and

bond-angle distributions, the ring statistics, the pair correlation functions, the x-ray and neutron structure factors, and the partial structure factors. Section 4.3 is devoted to vibrational density of states, which is analysed in terms of Ge and Se weights, and then further in terms of rocking, bending, and stretching motions. The inelastic neutron spectrum is calculated and compared to experiment. Section 4.4 focuses on infrared properties, such as the dynamical Born charges and the dielectric constants. The dielectric functions are calculated and compared to their experimental counterparts. In Sec. 4.5, we address the Raman spectra focusing in particular on the origin of the dominant Raman doublet and on the role of Se-Se homopolar bonds. The conclusions are drawn in Section 4.6.

4.1   Models generation

We here generated three models of vitreous GeSe$_2$. Models I and II are intended to be representative of the structural conception in which a strong chemical order prevails. To obtain these models, we first carried out classical molecular dynamics using the interatomic potentials given by Vashishta *et al.* [7]. Through a quench from the melt, we generated disordered structures consisting of chemically ordered networks of corner-sharing tetrahedra, consistent with the literature [7]. The final step of the generation procedure consists in applying a damped first-principles molecular dynamics which further optimizes the structural geometry. The first-principles relaxation only slightly modified the structure achieved by classical molecular dynamics, affecting approximately 10% of the atoms. Typical modifications involve the creation of both over- and under coordinated atoms. This procedure led to the formation of homopolar Se–Se bonds, but the creation of Ge-Ge bonds was not observed. Other minor modifications involved a slight increase in the equilibrium bond lengths and a corresponding decrease in the intertetrahedral angles. These models contained 180 (Model I) and 120 atoms (Model II) in a periodically repeated cubic cell, at a density of 4.4 g/cm^3, close to the experimental density of v-GeSe$_2$ (4.2 g/cm^3, Ref. [17]).

Model III is representative of the structural conception that the structure in the vitreous state features a rich variety of nearest neighbor motifs, as found in first-principles molecular dynamics simulations of liquid GeSe$_2$ [26]. To generate Model III, we started from an atomic configuration of the equilibrated liquid [26, 27] by rescaling the coordinates to match the density of the amorphous. The liquid was cooled from 1100 to 600 K in 22 ps (10 ps at 1100 K, 7 ps at 900 K, and 5 ps at 600 K). The system was then annealed for other 22 ps at $T = 300$ K and finally quenched to $T = 0$ K.

In the present work, we performed electronic-structure calculations and molecular dynamics using first principles methodologies [56, 63], as provided in the QUANTUM-ESPRESSO package [64]. The electronic structure was treated within a generalized gradient
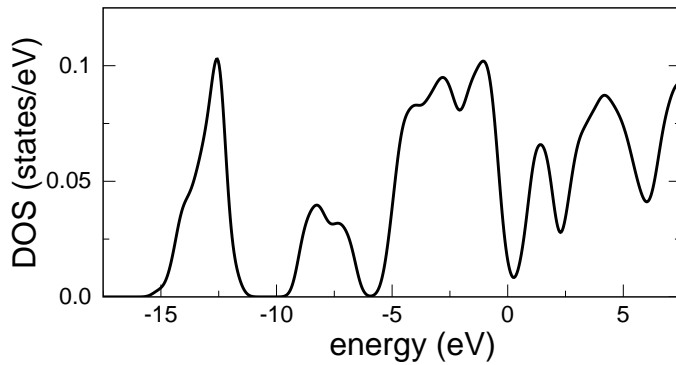
Figure 4.1: Electronic density of states (DOS) for Model I of v-GeSe$_2$. The highest occupied states are aligned at 0 eV. A Gaussian broadening of 0.25 eV is used.

approximation (GGA) [106] to density functional theory (DFT). Core-valence interactions were described through normconserving pseudopotentials for Ge and Se [107, 26]. For the electron wave functions and charge density, we used plane-wave basis sets defined by energy cutoffs of 15 Ry and 120 Ry, respectively [63]. The Brillouin zone was sampled at the Γ point.

We derived the vibrational frequencies and eigenmodes from the dynamical matrix, which was calculated numerically by taking finite differences of the atomic forces [35]. For accessing the infrared and Raman spectra, we took advantage from a recently developed scheme for applying a finite electric field in periodic cell calculations [47]. We obtained the relevant coupling tensors by numerically calculating first and second derivatives of the atomic forces with respect to the electric field [48]. We applied fields of ± 0.0005 a.u. To check the convergence of our finite-difference scheme, we also considered electric fields of ± 0.00025 a.u. but found negligible modifications to the calculated vibrational spectra.

We show in Fig. 4.1 the electronic density of states of Model I, which is representive of this vitreous material. The origin of the bands [128] is analoguous to the cases of SiO$_2$ (Ref. [129]) and of GeO$_2$ (Ref. [96]). The lowest band arises from Se $4s$ states. The low-energy side of the central band results from the Ge-Se bonds, formed by Ge sp^3 and Se $4p$ orbitals. The high-energy side of this central band, which defines the top of the valence band, consists of Se $4p$ lone pairs. The low-energy part of the conduction band mainly consists of antibonding states associated to the Ge-Se bond. The present results are consistent with the electronic density of states obtained for v-GeSe$_2$ within an approximate density-functional scheme [29] and with that obtained for model clusters of GeSe$_2$ [128]. The calculated energy separation between the highest occupied and lowest unoccupied Kohn-Sham levels (0.5 eV) is significantly smaller than the experimental optical gap (2.2 eV, Ref. [130]). An underestimation of the band gap is usual in density functional calculations. In the case of disordered systems, an additional difficulty in the comparison with experiment arises because of size limitations that prevent an accurate description of the
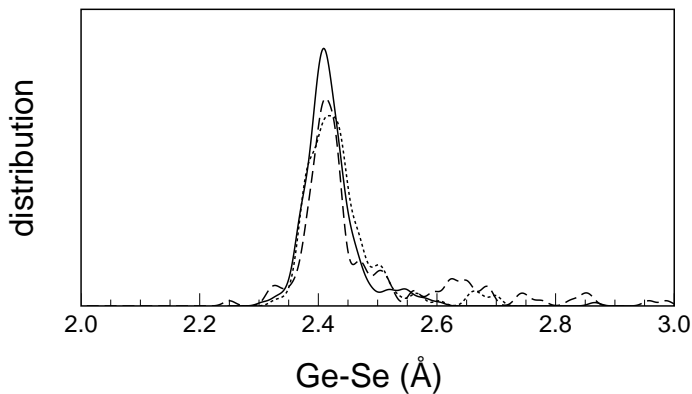
Figure 4.2: Distribution of Ge–Se bond lengths in Model I (solid), Model II (dotted), and Model III (dashed). A Gaussian broadening of 0.01 Å is used.
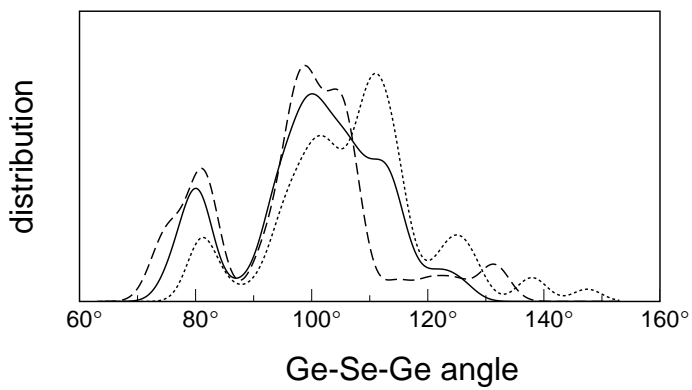

Figure 4.3: Distribution of the Ge-Se-Ge intertetrahedral angle for our models of v-GeSe$_2$: Model I (solid), Model II (dotted), and Model III (dashed). A Gaussian broadening of 2.5° is used.

band tails.

4.2   Structural properties

4.2.1   Real-space properties

In all our models, the average Ge-Se bond length is found to be slightly larger than the experimental one (cf. Table 4.1). The bond elongation should be attributed to a general tendency of first-principles GGA calculations [107]. In Fig. 4.2, we compare the Ge-Se bond-length distributions of our models. Model I shows the most narrow distribution with a peak at ~2.4 Å, while Models II and III have wider bond-length distributions characterized by tails extending up to 3.0 Å.

The structure of Model I mainly shows well defined tetrahedral units with an average Se-Ge-Se angle (109.1°) close to the ideal one and a standard deviation of 9.5°. The structure of Model II is also characterized by well defined tetrahedral units, but shows larger distortions presumably due to the smaller model size. In Model III, only 78% of the Ge atoms form tetrahedral units and the average Se-Ge-Se angle deviates more significantly

from the ideal tetrahedral angle.

We give in Fig. 4.3 the Ge-Se-Ge angle distributions for the twofold coordinated Se atoms in our models. For Models I and II this includes a very large fraction of the Se atoms (94% and 86%, respectively), consistent with the chemically ordered nature of these networks (Table 4.2). In Model III, this distribution only concerns 55% of the Se atoms (Table 4.2). This model indeed shows a large fraction of Se atoms in one-fold (21%) or threefold (20%) coordinated arrangements. The average angle in Models I and III is about $101°$ with standard deviations of $12.1°$ and $16.2°$, respectively. In Model II, the average angle is slightly larger ($107.8°$), but shows a similar standard deviation $12.7°$. The parameters characterizing the bond-length and bond-angle distributions of our models are summarized in Table 4.1.

The three Ge-Se-Ge angle distributions in Fig. 4.3 feature a distinct peak at $80°$ that corresponds to edge-sharing tetrahedra. Its intensity reflects the concentration of such units in the models and can be quantified in terms of the percentage of involved Ge atoms. For Models I, II, and III, this concentration amounts to 33%, 15%, and 55%, respectively. The concentration of edge-sharing tetrahedra in Model I is very close to the experimental estimate (34%, Ref. [25]) and to results previously obtained by Vashishta *et al.* (32%, Ref. [7]).

An atomic configuration involving edge-sharing tetrahedra gives rise to a four-atom ring in which Ge and Se atoms alternate. These rings are found to be quasi planar, with an average sum of bond angles ($357°$) very close to the ideal value for the perfectly planar ring ($360°$). In these rings, the average Ge-Se-Ge angle amounts to $80.2°$ (Fig. 4.3). The corresponding Ge-Se bond length averages to 2.41 Å with a standard deviation of 0.025 Å. Thus, the bond lengths in the rings do not differ significantly from the mean Ge-Se bond length (2.42 Å).

The ring statistics of our v-GeSe$_2$ models, calculated as in Ref. [26], are shown in Fig.

Table 4.1: Structural properties of our models of v-GeSe$_2$: number of atoms (N), average Ge-Se-Ge and Se-Ge-Se angles, and average bond length (d_{GeSe}). The respective standard deviations are given in parentheses. The experimental value for the bond length is taken from Ref. [25].

	N	$\angle$ Ge-Se-Ge	$\angle$ Se-Ge-Se	d_{GeSe} (Å)
Model I	180	$100.6°$ ($12.1°$)	$109.1°$ ($9.5°$)	2.42 (0.05)
Model II	120	$107.8°$ ($12.7°$)	$108.6°$ ($12.0°$)	2.44 (0.07)
Model III	120	$100.7°$ ($16.2°$)	$106.8°$ ($11.3°$)	2.47 (0.13)
Expt.				2.36

Table 4.2: Composition of first-neighbor shells of Ge and Se atoms expressed as a percentage in our models of v-GeSe$_2$. For each composition, the coordination is indicated by ℓ. For Ge-Se and Se-Se bonds, we used cutoff radii of 3.0 and 2.7 Å, respectively. Ge-Ge bonds do not occur in our models. We also quantify the amount of homopolar bonds and of edge-sharing tetrahedra (ES-T) in terms of percentages of the involved atoms. Experimental values are taken from Ref. [25].

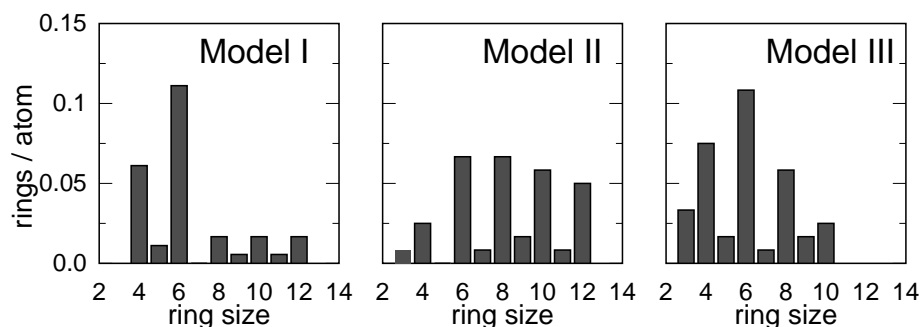|	Composition	ℓ	Model I	Model II	Model III	Expt.
Ge						
	Se$_3$	3	5	7	20	
	Se$_4$	4	95	93	78	
	Se$_5$	5	–	–	2	
Se						
	Ge	1	1	–	1	
	SeGe	2	3	8	20	
	Ge$_2$	2	92	86	55	
	Se$_2$	2	–	–	4	
	SeGe$_2$	3	2	–	–	
	Se$_2$Ge	3	–	1	–	
	Ge$_3$	3	2	5	20	
Se-Se			5	9	24	20
Ge-Ge			–	–	–	25
ES-T			33	15	55	34

Figure 4.4: Ring statistics of Models I, II and III of v-GeSe$_2$, calculated as in Ref. [26]. For simplicity, a common cutoff radius of 3.0 Å was used for Ge-Ge, Ge-Se, and Se-Se bonds.

4.4. The ring size indicates the number of atoms composing the ring. Odd size rings include homopolar bonds, a feature which is absent in chemically ordered materials such as v-SiO$_2$ and v-GeO$_2$ [21, 96]. The ring statistics of our models clearly show the predominance of even-membered rings. A higher concentration of odd-membered rings can be discerned for Model III. The six-atom rings always belong to the dominant ring sizes. The higher ring sizes are unfrequent in Model I, but occur in higher concentrations for Models II and III.

The occurrence of homopolar bonds in v-GeSe$_2$ has been observed experimentally [25, 127]. In Model I, the Se–Se homopolar bonds involve 5% of the Se atoms (Table 4.2), considerably less than found experimentally (20%) [25]. This difference should be assigned to the classical molecular dynamics part of our generation procedure, which does not allow for the formation of such homopolar bonds. Model II features similarly a low fraction (9%). At variance, the *ab initio* generation scheme used for Model III gives a fraction of 24%, only slightly larger than experiment. The Se-Se bond lengths are generally found to overestimate the experimental value by about 5% (∼2.4 Å). Recent neutron diffraction data indicate that 25% of the Ge atoms are involved in Ge-Ge homopolar bonds. However, none of our models shows such bonds. At present, this corresponds to a limitation of our model generation procedures. Vibrational features associated to Ge-Ge bonds can therefore not be identified with the present set of models.

We calculate pair correlation functions (PCFs) using Gaussian correlations of which the spread is derived from the vibrational eigenmodes and frequencies in the harmonic approximation. A detailed account of this approach is given in Sec. 2.2.1. This formulation offers the advantage of accounting for the zero-point motion and has been found to give a good description of oxide glasses at 300 K [70, 71].

In Figure 4.5, we show the PCFs calculated at room temperature for Model I of v-GeSe$_2$ together with corresponding experimental data [25]. Overall, we register a good
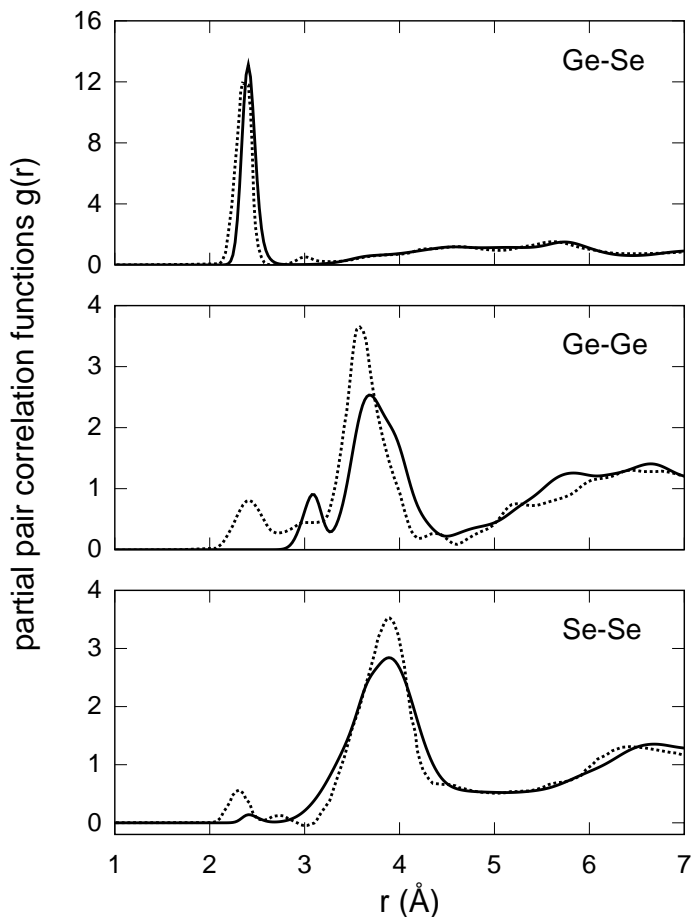
Figure 4.5: Partial pair correlation functions of v-GeSe$_2$ at room temperature: Model I (solid) and experimental data from Ref. [25] (dotted).

agreement between experiment and theory. In particular, the Ge-Se PCF is dominated by a strong peak in correspondence of the Ge-Se bond length. A spherical integration of the theoretical peak gives a coordination number of 3.96, slightly higher than the experimental value of 3.7 [25]. The theoretical peak is shifted by $\sim$0.06 Å with respect to the experimental one, reflecting the longer mean bond length in the simulation. Similarly, the main peak in the Ge-Ge PCF is shifted by $\sim$0.1 Å with respect to the experimental peak. The first two peaks in the theoretical Ge-Ge PCF reflect the Ge-Se-Ge angle distribution (Fig. 4.3), distinguishing Ge-Ge correlations in edge- and corner sharing tetrahedra at 3.1 and 4.0 Å, respectively. The experimental Ge-Ge PCF shows in addition a peak at 2.42 Å corresponding to homopolar Ge-Ge bonds, which are absent in our models. The difference between the experimental and theoretical Se-Se PCF is mainly limited to the peak at 2.32 Å corresponding to Se-Se homopolar bonds. Its intensity relates to the concentration of such bonds, which is lower in Model I (5%) than in the experiment (20%) (Table 4.2).
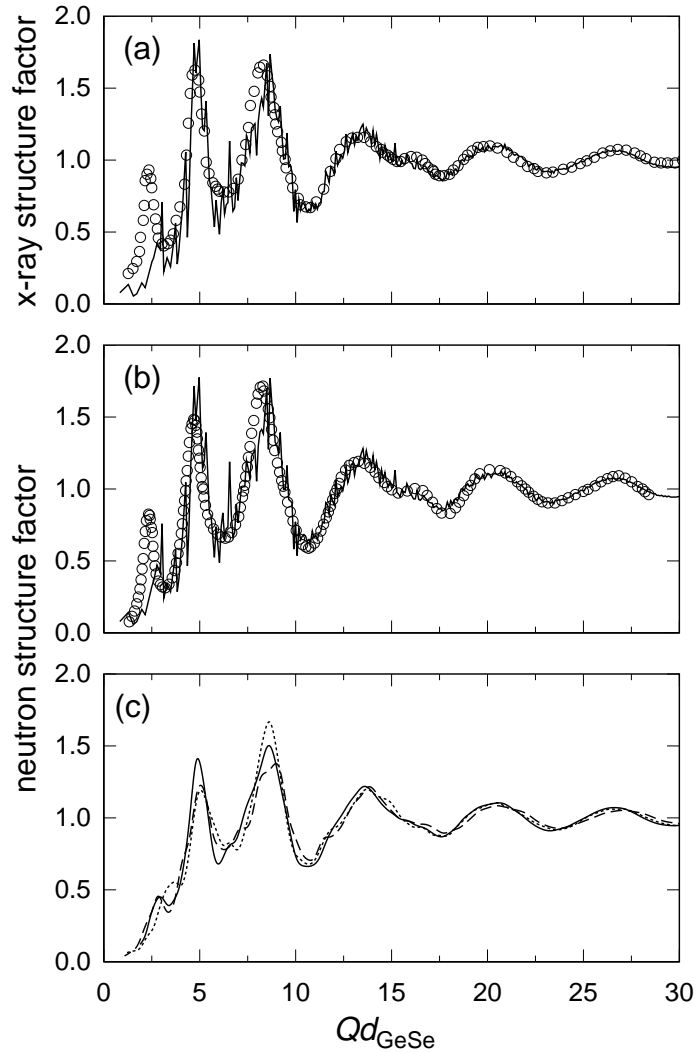
Figure 4.6:   (a) X-ray and (b) neutron structure factors at room temperature for Model I (solid) compared to the experimental data (circles) obtained in Refs. [126] and [131], respectively. (c) Comparison between calculated neutron structure factors of Models I (solid), II (dotted), and III (dashed). A Gaussian broadening of 0.1 Å^{-1} is used. The bond lengths in Table 3.1 are used to rescale the transferred momenta.

4.2.2   Reciprocal-space properties

We calculated x-ray, neutron, and partial structure factors at room temperature accounting for the vibrations in the harmonic approximation [96], as presented in our study of v-SiO$_2$ (Chapt. 2). For the x-ray structure factor, we used atomic structure factors dependent on the scattering vector [76]. For the neutron structure factor, we used scattering lengths of 8.185 and 7.97 fm for Ge and Se, respectively [132]. For v-GeSe$_2$, x-ray and neutron diffraction probes give very similar structure factors, since Ge and Se atomic species have close atomic numbers and similar neutron scattering lengths.

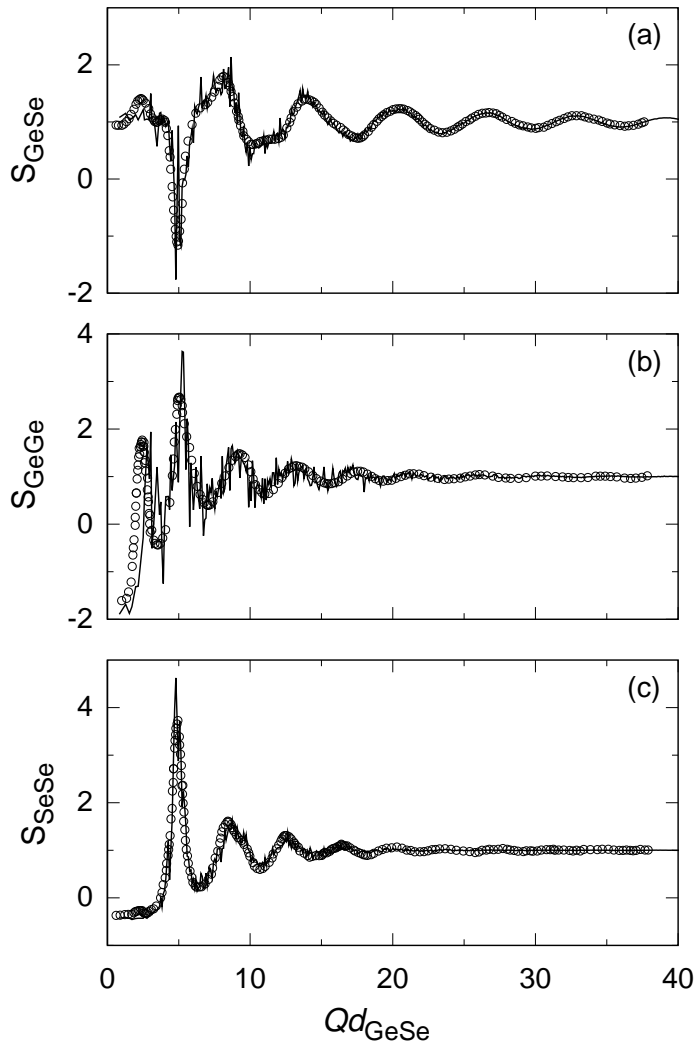In Fig. 4.6(a) and (b), we show the comparison between the x-ray and neutron structure

Figure 4.7:   Faber-Ziman partial structure factors at room temperature: Model I (solid) vs experiment (Ref. [25]) (circles). Transferred momenta are rescaled as in Fig. 4.6.

factors calculated for Model I and the experimental data [126, 131]. In the figure, the scattering vectors are rescaled to an adimensional quantity Qd_{GeSe}, in consideration of the different average bond lengths d_{GeSe} in theory and experiment. Our model structure shows good agreement with both experimental results, particularly in the range $Qd_{\mathrm{GeSe}} \geq$ 7, which mostly depends on the tetrahedral structural unit. The first sharp diffraction peak (FSDP) of Model I also shows fair agreement with the experiment as far as its intensity is concerned, but its position is found to be shifted to larger scattering vectors. This shift originates from slight differences in the atomic arrangements occurring over intermediate-range lengths, but this relation is nontrivial [133, 134].

We compare in Fig. 4.6(c) the neutron structure factors calculated for Models I, II, and III. The comparison shows that the structure factors differ for $Qd_{\mathrm{GeSe}} \leq 8$, but that they

become very similar for larger Q vectors. Models I and III give a very similar FSDPs as far as both their positions and intensities are concerned. In Model II, the FSDP does not stand out clearly and appears as a shoulder of the peak at $Qd_{GeSe} = 5$. The partial structure factors in the Faber-Ziman formulation calculated for Model I are compared to their experimental counterparts [25] in Fig. 4.7. The agreement with experiment is excellent for the partial structure factors S_{GeSe} and S_{SeSe} over the full range of scattering vectors, including the FSDP region. For S_{GeGe}, the agreement is similarly very good in the range of scattering vectors beyond the FSDP. We record the largest differences between theory and experiment in the FSDP region of S_{GeGe}. These differences might result from the absence of homopolar Ge-Ge bonds in Model I. A similar level of agreement is found for Models II and III (not shown).

To highlight effects associated to the chemical order, we focus in Fig. 4.8 on the concentration-concentration structure factor $S_{CC}(Q)$, as defined in the Bhatia-Thornton formulation [78]. We note that the number-number structure factor $S_{NN}(Q)$ in this formulation (not shown) faithfully reproduces the neutron structure factor because of the close scattering lengths of Ge and Se atoms [26]. In Fig. 4.8(a), we compare the $S_{CC}(Q)$ of Model I with experiment [127] finding overall good agreement. In particular, in the FSDP region, the theoretical spectrum shows a feature of comparable intensity with respect to the experimental FSDP. The respective results for Models I, II and III are compared in Fig. 4.8(b). Despite the important structural differences between the models, their $S_{CC}(Q)$ structure factors are very similar, with only minor discernable variations upto ~ 6 Å^{-1}.

Apart from the concentration of homopolar bonds, our three models well reproduce the experimental diffraction data pertaining to short-range order. This good agreement applies to models of both kinds of structural conception (Models I and II vs Model III), thereby confirming the weak sensitivity of diffraction probes to the underlying chemical order.
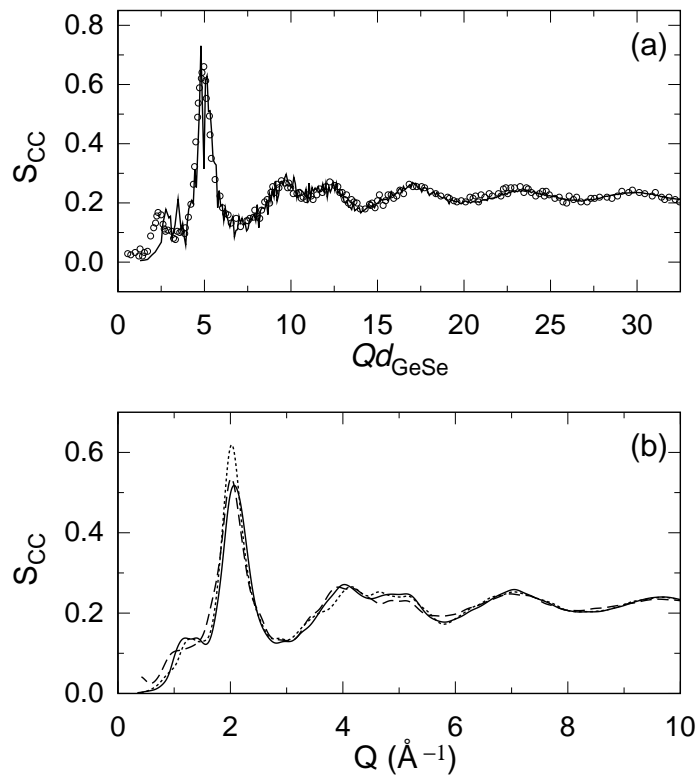
Figure 4.8:   (a) Bhatia-Thornton concentration-concentration partial structure factors at room temperature: Model I (solid) vs experiment (Ref. [127]) (circles). Transferred momenta are rescaled as in Fig. 4.6. (b) Comparison between calculated concentration-concentration partial structure factors of Models I (solid), II (dotted), and III (dashed). A Gaussian broadening of 0.1 Å^{-1} is used (cf. App. A).

4.3 Vibrational properties

In Fig. 4.9, we compare the vibrational densities of states (v-DOS) of Models I, II and III. The three spectra feature three main frequency bands: a low band extending upto 150 cm^{-1}, a middle band (150–200 cm^{-1}), and a high band above 200 cm^{-1}. Overall, the three models show similar spectra with minor differences. The model-dependent variations are larger for the middle and high bands than for the low band.

To analyse the nature of the vibrational modes, we focus in the following on the v-DOS of Model I. In Fig. 4.10(a), we show the decomposition of the v-DOS according to the Se and Ge weights in the vibrational eigenmodes [Eq. 2.23]. The low band shows a high Se character with a Se weight about three times larger than the Ge weight, a ratio higher than the ratio between the atomic concentrations. The dominance of Se character is even more important in the middle band, which features a weak Ge contribution. At variance the Ge character is well represented in the high band which shows similar Ge and Se weights. In Fig. 4.10(b), we further analyze the vibrations of the Se atoms in terms of rocking, bending, and stretching motions [60]. In this analysis, we only considered Se atoms twofold coordinated with Ge, which correspond to 94% of the Se atoms in Model I. We took the bending direction along the bisector of Ge-Se-Ge angle, the rocking direction normal to the plane of the Ge-Se-Ge bridge, and the stretching direction orthogonal to the previous two. The projections on these directions show that rocking motions only contribute to the low band, whereas bending and stretching motions strongly intermix in the middle and high bands. In particular, the bending and stretching motions contribute with similar weights to the Se peak at ~180 cm^{-1}. The bending contribution shows a second peak at 285 cm^{-1}, while a second peak of the stretching contribution occurs at 225 cm^{-1}.

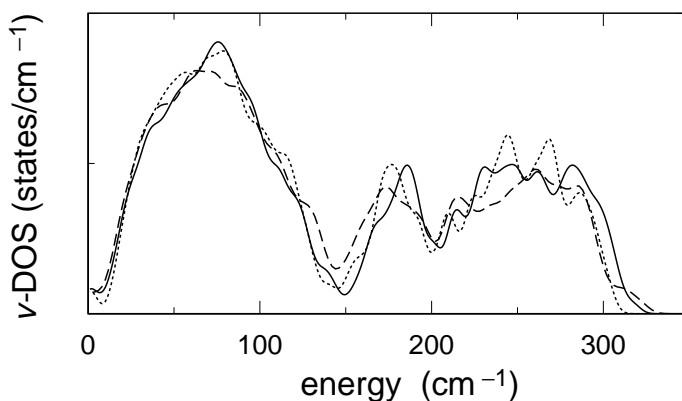A comparison with experiment can be carried out for the inelastic neutron spectrum.

Figure 4.9: Normalized vibrational density of states (v-DOS) of v-GeSe$_2$: a comparison between Models I (solid), II (dotted), and III (dashed). A Gaussian broadening of 4 cm^{-1} is used.
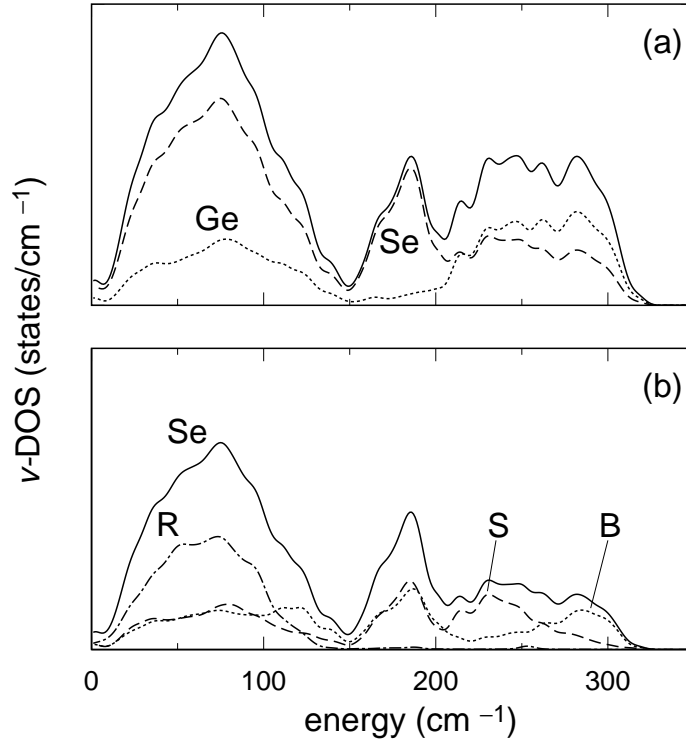
Figure 4.10:   (a) Vibrational density of states (v-DOS) of Model I of v-GeSe$_2$ and its decomposition into Ge (dotted) and Se (dashed) weights. (b) Further decomposition of the Se weight into bending (dotted), rocking (dot-dashed), and stretching (dashed) motions. Only Se atoms twofold coordinated by Ge are considered. A Gaussian broadening of 4 cm^{-1} is used.

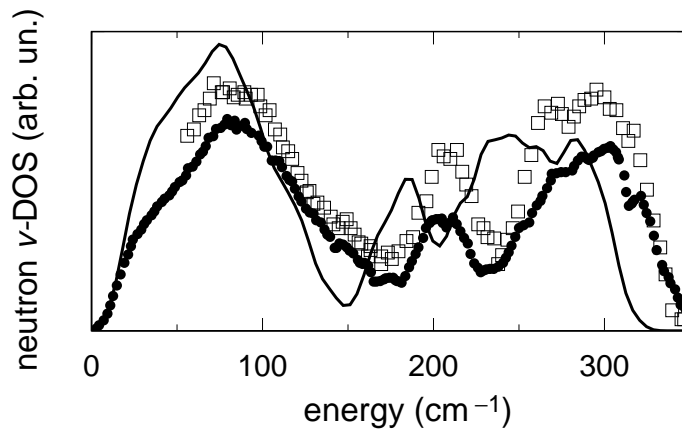Figure 4.11:   Neutron vibrational density of states of v-GeSe$_2$ at 13 K calculated for Model I (solid), compared to corresponding experimental data of Ref. [38] (open squares). Experimental data obtained at room temperature (Ref. [135], closed circles) are shown for comparison. Transferred momenta are taken in the range 0.6–8.5 Å^{-1}, corresponding to the experimental interval (Ref. [38]).

We calculated this spectrum for Model I in the one-phonon approximation [74, 35]. The calculated inelastic neutron spectrum in Fig. 4.11 is found to closely resemble the v-DOS in Fig. 4.9, in analogy with similar comparisons for v-SiO$_2$ (Ref. [35]) and v-GeO$_2$ (Ref. [96]). Figure 4.11 also shows that the calculated inelastic neutron spectrum compares well with the available experimental spectra, [38, 135] reproducing all the salient features. However, the calculated frequencies are systematically lower than the measured ones. Such underestimations have already been encountered in previous theoretical work on disordered systems [29, 37]. The good agreement with experiment recorded for the inelastic neutron spectrum appears as a solid basis for envisaging the analyses of the infrared and Raman spectra.

4.4   Infrared Spectra

4.4.1   Born charge tensors

The coupling of the vibrational motions to the electric field is described by the dynamical Born charge tensors [84]. We calculated, as explained in Secs. 2.6.1 and 2.4, Born charge tensors Z* of all the Ge and Se atoms in our models.

Because of their predominant tetrahedral bonding, the Born charge tensor of the Ge atoms is well described by an isotropic tensor. Averaging over all the Ge atoms in our models, we obtained an isotropic Born charge of 2.67. Correspondingly, the average of the isotropic Born charge of the Se atoms is -1.33. The individual models give similar average isotropic Born charges, as summarized in Table 4.3. It is interesting to note that the standard deviations of the distributions of isotropic Born charges in v-GeSe$_2$ are at least two times larger than in v-SiO$_2$ or v-GeO$_2$ [3, 96].

Focusing on the Se atoms with two Ge nearest neighbors, the dynamical Born tensor is conveniently expressed with respect to a local reference set based on the orientation of the Ge-Se-Ge unit. We took x, y, and z directions along the bending, rocking, and stretching directions defined in Sec. 4.3. By averaging over all models, we obtained

$$Z_{\text{Se}}^* = \left(\begin{array}{ccc} -0.96 & 0.02 & 0.05 \\ 0.01 & -1.00 & 0.00 \\ 0.04 & 0.04 & -2.25 \end{array} \right). \tag{4.1}$$

The average Z_{Se}^* tensor is well described by a diagonal tensor, as already found for the oxygen atoms in silica and germania [3, 96]. The displacements along the stretching direction (z direction) couple to the electric field twice as much as those along the other directions. Typically, the Se Born charge along the z direction is 20% lower than the corresponding
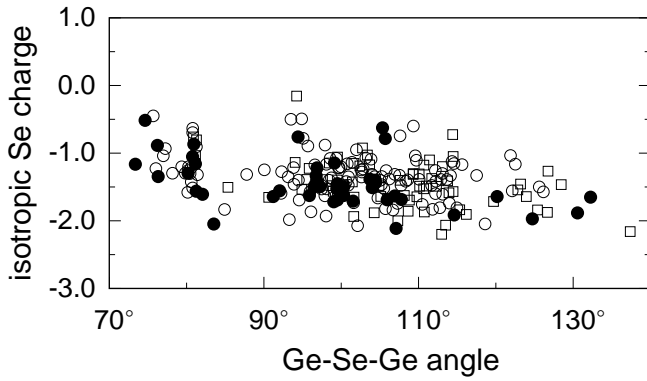
Figure 4.12: Isotropic Se Born charge (Z^*_{Se}) vs Ge-Se-Ge angle for Models I (open circles), II (open squares), and III (closed circles). Only Se atoms twofold coordinated by Ge are considered.

O one in disordered oxides [96]. A more detailed analysis of the calculated Born charge tensors reveals that differences among our three models are not significant.

For the Se atoms with two Ge nearest neighbors, we investigated the dependence of the isotropic part (Z^*_{Se}) of the Se Born charge tensors on the Ge-Se-Ge angle. Our results in Fig. 4.12 show that Z^*_{Se} tends to decrease with increasing Ge-Se-Ge angle. Such a dependence on the angle was already observed for the oxygen isotropic charge in v-SiO$_2$ and v-GeO$_2$ [3, 96]. However, in v-GeSe$_2$, the Se isotropic Born charge is much less sensitive on the intertetrahedral angle and the spread is significantly larger.

We also considered the average isotropic Born charges of threefold coordinated Se (Z^*_{SeIII}) and Ge (Z^*_{GeIII}) atoms. From an average over the three models, we derived $Z^*_{SeIII} = -1.84$ and $Z^*_{GeIII} = 2.39$. The value for the threefold coordinated Se atoms is more negative by 38% with respect to the full average, indicating a higher dynamic ionicity for these atoms. At variance, the threefold coordinated Ge atoms show a lower ionicity, as witnessed by a decrease of 10% of their isotropic Born charges. We note that the local enviroment around the threefold coordinated atoms does not only differ because of the modified coordination but also because of their specific Ge-Se bond length ($\sim$2.6 Å), which, for both threefold coordinated Se and Ge atoms, is found to elongate by about 7% with respect to the average bond length (Table 4.1). Average Born charges for threefold atoms in the individual models are given in Table 4.3. For Se atoms forming homopolar bonds, we calculated an average isotropic Born charge of -0.56 with a spread of 0.72. The spread is significantly larger than typical values in Table 4.3, indicating that these Born charges are highly sensitive to the local disorder.

4.4.2   Dielectric constants

For our models of v-GeSe$_2$, we calculated the high-frequency dielectric constant ϵ_∞ through second derivatives of the energy with respect to the electric field [Eq. (2.32)]. As given

Table 4.3: Average isotropic Born charge of all Se (Z^*_{Se}) and Ge (Z^*_{Ge}) atoms in our models of v-GeSe$_2$. The average isotropic Born charge of threefold coordinated Se (Z^*_{SeIII}) and Ge (Z^*_{GeIII}) atoms are also given. Standard deviations of the respective distributions are given in parentheses.

Model	Z^*_{SeIII}	Z^*_{GeIII}	Z^*_{Se}	Z^*_{Ge}
I	−1.67 (0.08)	2.18 (0.25)	−1.31 (0.40)	2.63 (0.21)
II	−1.93 (0.23)	2.43 (0.39)	−1.38 (0.57)	2.76 (0.29)
III	−1.84 (0.32)	2.46 (0.53)	−1.32 (0.60)	2.63 (0.39)
All	−1.84 (0.29)	2.39 (0.44)	−1.33 (0.51)	2.67 (0.30)

in Table 4.4, we calculated average values of ϵ_∞ in the range 7.2–7.7. Infrared oscillator strengths can be derived from the vibrational eigenmodes and the dynamical Born charges [3, 96]. The static dielectric constants ϵ_0 are then obtained from the vibrational frequencies and their corresponding oscillator strengths [Eq. (2.35)]. The values calculated for our models range between 11 and 15 (Table 4.4).

The calculated values for both the high-frequency and static dielectric constants are larger than the corresponding experimental values of 5.5 (Ref. [136]) and 7.2 (Ref. [137]), respectively. The differences between theory and experiment are too large to be explained by the usual overestimations of DFT calculations [138]. To understand the origin of these differences, it is instructive to consider the high-temperature crystalline form of GeSe$_2$, which is composed of corner- and edge-sharing tetrahedra [139]. Measured values of ϵ_∞ and ϵ_0 for this structure give, after averaging over Cartesian directions, ~ 8.7 and ~ 10.5, respectively [140]. These values do not reconcile well with the experimental data for v-GeSe$_2$. However, they are consistent with the theoretical values for Model I. Models II and III show considerably higher values for ϵ_0, indicating that this property is sensitive to the variety of underlying atomic structures considered here for v-GeSe$_2$.

Table 4.4: High-frequency (ϵ_∞) and static dielectric constants (ϵ_0) for our models of v-GeSe$_2$. Respective experimental data are taken from Refs. [136] and [137].

	Model I	Model II	Model III	Expt.
ϵ_∞	7.2	7.65	7.3	5.5
ϵ_0	11.4	14.1	15.0	7.22

4.4.3 Dielectric functions

The high-frequency dielectric constant, the vibrational frequencies, and their corresponding oscillator strengths fully determine the dielectric function [Eqs. (2.36)-(2.37)]. In Figure 4.13, we give for Model I the real (ϵ_1) and imaginary (ϵ_2) parts of the dielectric function, together with the longitudinal response function $-\omega \mathrm{Im}(1/\epsilon)$. Available experimental spectra from Refs. [39] and [141] are also reported for comparison.

The calculated ϵ_1 [Fig. 4.13(a)] shows two clear resonances in correspondence of the two principal peaks of ϵ_2 at 86 and 232 cm^{-1}. We did not find an experimental spectrum for ϵ_1 of v-Gese$_2$. However, the calculated spectrum shows a similar shape as for v-SiO$_2$ and v-GeO$_2$,[48, 96] with broadened features due to the higher degree of disorder.

For ϵ_2, our results reproduce the two main peaks of the experimental spectrum [Fig. 4.13(b)] [39, 141]. As for the v-DOS (Fig. 4.11), the peak positions in the theoretical spectrum are found to be shifted to lower frequencies with respect to their positions in the experimental spectrum, by 10 and 25 cm^{-1} for the peaks at 86 and 232 cm^{-1}, respectively. The peaks in the calculated spectrum are broader than their experimental counterparts. We attribute this effect to an excessive degree of residual strain in our model structure [48].

The theoretical longitudinal response function $-\omega \mathrm{Im}(1/\epsilon)$ agrees well with the corresponding experimental spectrum[39] [Fig. 4.13(c)] as far as are concerned the global shape and the relative heights of the main features. Only a slight difference between theory and experiment is observed on the high-frequency side of the principal peak. The shifts of the main features with respect to their position in ϵ_2 give the longitudinal-optic/transverse-optic (LO-TO) splittings. We obtained LO-TO splittings of 7 and 33 cm^{-1} for the two main features in ϵ_2 in fair agreement with the corresponding experimental splittings of 10 and 24 cm^{-1}.

In Figure 4.14, we compare the imaginary parts of the dielectric functions calculated for our three models. The agreement with experiment is clearly best for Model I, and degrades going from Model I to Model III. The spectrum of Model II resembles that of Model I, but the main features are further broadened. Indeed, these two models both show a large predominance of tetrahedra, but structural disortions are clearly more important in Model II, as witnessed by the larger spreads in the bond-length and Se-Ge-Se angle distributions (Table 4.1). For Model III, the broadening increases further and an additional peak arises at ~ 160 cm^{-1} which does not occur in the experiment. The degree of disorder in the first coordination shells in this model appears therefore incompatible with the experimental shape of the infrared ϵ_2.
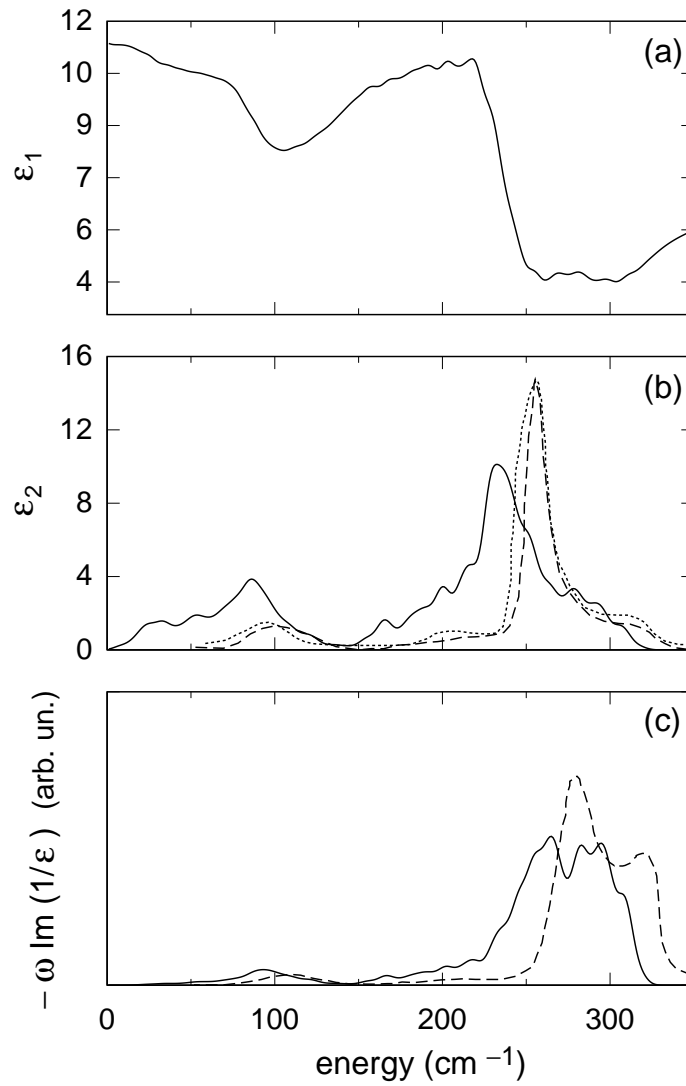
Figure 4.13: Dielectric function of Model I of v-Gese$_2$ (solid) compared to experimental data from Refs. [141] (dotted) and [39] (dashed): (a) real part, (b) imaginary part, and (c) longitudinal response $-\omega\text{Im}(-1/\epsilon)$. A Lorentzian broadening of $8\,\text{cm}^{-1}$ is used in (a), while Gaussian broadenings of $4\,\text{cm}^{-1}$ are used in (b) and (c). In (c), the experimental and theoretical spectra are rescaled to show the same integrated intensity.
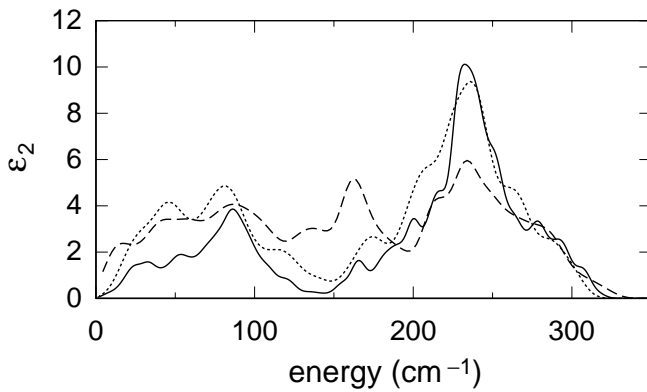
Figure 4.14: Comparison between the calculated imaginary parts of the dielectric functions of v-GeSe$_2$ for Models I (solid), II (dotted), and III (dashed). A Gaussian broadening of 4 cm^{-1} is used.

4.5   Raman spectra

Raman spectra of v-GeSe$_2$ are usually obtained for in-coming and out-going photons with either parallel (HH) or perpendicular polarizations (HV).

The experimental HH Raman spectrum of v-GeSe$_2$ is characterized by a strong doublet with a principal peak located at 201 cm^{-1} and a companion peak at 218 cm^{-1} [32]. Investigating Ge$_x$Se$_{1-x}$ samples for varying x, Tronc *et al.* [142] noticed that the principal line shows up as soon as a finite concentration of Ge occurs, and that its intensity strongly increases with Ge content. Therefore, the principal line indicates the occurrence of Ge atoms in a Se environment, i.e. the formation of the Ge(Se$_{1/2}$)$_4$ tetrahedron. The origin of the companion line has long been debated [31, 32, 33, 34]. Recent work supports the assignment of this line to vibrations in edge-sharing tetrahedra [31, 32, 33]. The high-temperature crystalline form in GeSe$_2$ which contains edge-sharing tetrahedra, indeed shows a line at 213 cm^{-1}, in close correspondence with the companion line of v-GeSe$_2$.

Other minor features can be discerned in the HH Raman spectrum of v-GeSe$_2$. The features located at 240 and 270 cm^{-1} are generally interpreted as due to vibrations associated to the Se-Se homopolar bonds [142, 32]. This assignment is achieved through comparisons with the Raman spectra of amorphous and crystalline selenium. The shoulder at ~ 179 cm^{-1} on the low-frequency side of the principal peak has been assigned to the homopolar Ge-Ge bond in an ethane-like atomic structure embedded in the glass [33].

4.5.1   Comparison with experiment

In Fig. 4.15, we compare the HH and HV reduced Raman spectra calculated for Model I to the experimental spectra [39] (we refer to Sec. 2.7 for the methodological aspects of the Raman spectra calculations). In the theoretical HH spectrum, the doublet is clearly recognizable despite the larger widths of the peaks and the overall shift to lower frequencies compared to the experiment. The calculated spectrum also shows bands at lower and
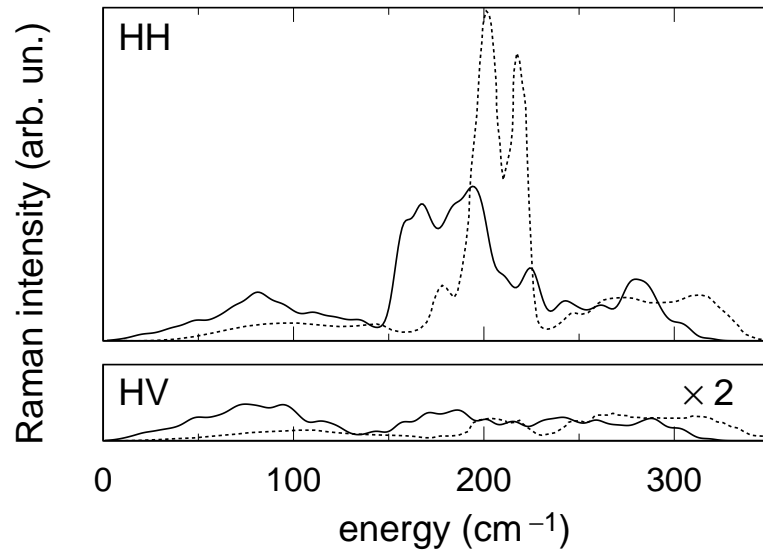
Figure 4.15:   Reduced HH and HV Raman spectra of v-GeSe$_2$ for Model I of v-GeSe$_2$ (solid), compared to experimental data of Ref. [39] (dotted). The calculated HH spectrum is scaled to match the integrated intensity of the experimental spectrum. The same scaling factor is used for the theoretical HV spectrum. For clarity, the HV spectra are magnified by a factor of two. A Gaussian broadening of 4 cm^{-1} is used.

higher frequencies of comparable intensity to the experimental spectrum. The Raman intensity of the HV spectrum is considerably weaker than that of the HH spectrum. We note that the experimental ratio between the integrated intensities of the HH and HV spectra is fairly well reproduced by our calculation. The experimental HV spectrum shows three distinct bands. In the calculation, the lowest band is clearly distinguishable but the two higher bands are found to merge.

In Fig. 4.16, we show the reduced HH Raman spectra of Models I, II, and III. Among these three models, the best agreement with the experimental spectrum is found for Model I (Fig. 4.15). The principal feature in the spectrum of Model II occurs in correspondence of the central doublet. However, the bands at lower and higher frequencies feature a considerably higher intensity than in Model I. This results in a diminuished contrast between the intensities in the central region of the spectrum and in the side bands. The spectrum of Model III shows a highly fluctuating intensity and differs significantly from the experimental spectrum. The calculated intensities are on average three times larger than in Model I, indicating a higher degree of polarisability in Model III. The absence of any similarity with the experimental spectrum and the high polarisability suggests that the variety of bonding motifs in Model III do not give a reliable representation of the structure of v-GeSe$_2$.

The three models showed comparable structure factors [Figs. 4.6(c) and 4.8(b)] and vibrational densities of states (Fig. 4.9). Nevertheless, we note that important differences
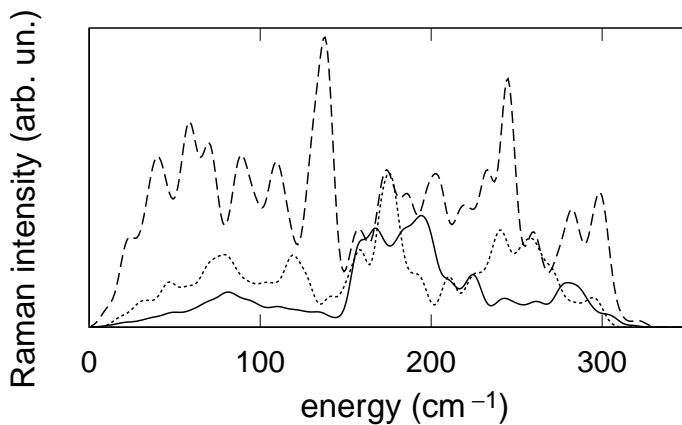
Figure 4.16: Comparison between the calculated reduced HH Raman spectra of v-GeSe$_2$ for Models I (solid), II (dotted), and III (dashed). A Gaussian broadening of 4 cm^{-1} is used.

occur in their Raman spectra. This indicates that the sensitivity of Raman coupling factors on structural parameters is particularly high. Therefore, the comparison of calculated and measured Raman spectra is a particularly selective criterion for identifying an optimal model structure.

4.5.2   Analysis in terms of atomic vibrations

With respect to their experimental counterparts, the simulated Raman spectra offer the advantage that they can conveniently be analyzed in terms of the underlying vibrational modes. In the following, we focused on Model I, which shows the best agreement with experiment. Figure 4.17(a) gives the decomposition of the Raman spectrum into Se and Ge weights. This is decomposition is achieved by selecting the components of the vibrational eigenmodes specific to either Se or Ge prior to the calculation of the Raman intensities. While the components obtained in this way do not sum up to give the full spectrum because of the interference terms, this analysis nevertheless provides insight into the origin of the various features. The central band (145-225 cm^{-1}) appears to originate almost exclusively from Se motions, whereas the rest of the spectrum also shows a considerable fraction of Ge vibrations. Overall, the distributions of the Se and Ge weights in the HH Raman spectrum show a similar behavior as in the vibrational density of states.

The contribution of Se atoms is further analyzed in Fig. 4.17(b) in terms of rocking, bending, and stretching motions. For this analysis, the decomposition shows important differences with respect to the analogous one of the vibrational density of states. In the frequency region below the main doublet, the Raman intensities associated with rocking, bending, and stretching motions have similar weights, while the rocking motions dominated in the v-DOS. Although the v-DOS indicates that both stretching and bending motions occur in comparable amounts in the frequency range of the main doublet, the major contribution to the Raman intensity of this feature originates mainly from the latter ones.
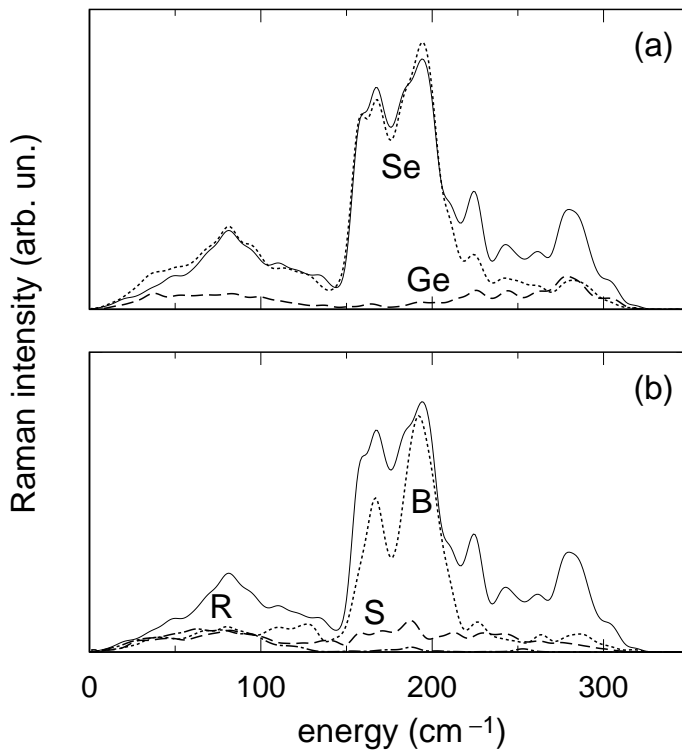
Figure 4.17: (a) Decomposition of the reduced HH Raman spectrum of Model I (solid) into Se (dotted) and Ge (dashed) weights following the procedure described in the text. (b) Further decomposition of the Se weight into rocking (dot-dashed), bending (dotted), and stretching (dashed) contributions (see text). A Gaussian broadening of $4 \, \text{cm}^{-1}$ is used.

The sum of the stretching and bending contributions to the principal peak noticeably differs from its total Se weight, indicating the occurrence of interference terms. For larger frequencies, both the contributions of stretching and bending motions are found to be of similar intensity, but do not separate in distinct peaks as for the v-DOS. In particular, the feature at $280 \, \text{cm}^{-1}$, which corresponds to the experimental peak at $310 \, \text{cm}^{-1}$ (Ref. [32]), shows the highest fraction of Ge motion and is accompanied by both stretching and bending Se motions.

This analysis shows that the bending motions give the largest contribution to the doublet in the HH Raman spectrum of v-GeSe$_2$. As for v-SiO$_2$ (Refs. [4] and [46]) and v-GeO$_2$ (Refs. [37] and [96]), the coupling to the bending motions is mainly isotropic. In particular, in the region of the main doublet, the isotropic bending contribution of Se atoms twofold coordinated by Ge accounts for 65% of the integrated intensity. In v-SiO$_2$ and v-GeO$_2$, the contribution of the isotropic bending coupling to O atoms reached percentages as high as 90% in the region of the principal Raman features [4, 37]. In v-GeSe$_2$, this percentage is lower because of the nonvanishing weight associated to stretching Se motions, particularly for the principal line.

4.5.3   Origin of the companion line

To investigate the contribution of edge-sharing tetrahedra to the HH Raman spectrum, we projected the vibrational eigenmodes onto Se breathing motions in four-atom rings. In these motions, the two Se atoms in the ring give rise to in-phase bending vibrations along the bisectors of their respective Ge-Se-Ge units [31, 32]. We then determined the contribution of these ring vibrations to the spectrum by using the projected eigenmodes in the expression for the Raman intensities [4, 96] (Sec. 2.7). For Model I, the Raman projection obtained in this way gives a distinct peak centered at 198 cm^{-1} [Fig. 4.18(a)], corresponding to the experimental position of the companion line [32]. However, we note that the intensity associated to the projected eigenmodes does not account for the full intensity of this line. Since the vibrational motions in this frequency range are almost exclusively given by Se bending motions [Fig. 4.17(b)], this results implies that the vibrational eigenmodes associated to four-atom ring vibrations are only partially localized on the rings. Analysis of Models II and III gives a similar picture with projected peaks at 193 and 194 cm^{-1}, respectively (not shown).

In principle, the ratio between the intensities of the companion and principal lines provides information concerning the concentration of edge-sharing tetrahedra. The large widths of the doublet lines in our calculation prevent an accurate determination of this ratio. However, we note that the relation between the intensities of the two doublet lines and the concentrations of edge- and corner-sharing tetrahedra is not trivial. Such a relation should account for the fact that the principal and companion lines show different decompositions into bending and stretching Se motions, hence implying different Raman activites. To illustrate the dependence of the Raman coupling on structural properties, we focus on Se bending motions [4, 96]. Figure 4.18(b) gives the isotropic component of this coupling vs. Ge-Se-Ge bond angle. We observe that there is a considerable spread (50 bohr^2) in the calculated values. However, the average coupling factor for Se atoms in four-atom rings (190 bohr^2) is sensibly higher than the average value pertaining to the other Se atoms (144 bohr^2). Incidentally, we remark that these coupling factors are one order of magnitude larger than corresponding ones for v-SiO$_2$ and v-GeO$_2$. This directly affects the relative integrated Raman intensities of these glasses.

4.5.4   Raman signature of Se–Se bonds

With the intent of identifying Raman peaks associated to homopolar Se-Se bonds, we calculated the Raman intensities accounting only for the contribution of the atoms involved in these bonds. As shown in Fig. 4.19(a), this gives a Raman intensity which spans the entire range of the spectrum. Specific projection onto Se-Se bond stretching motions re-
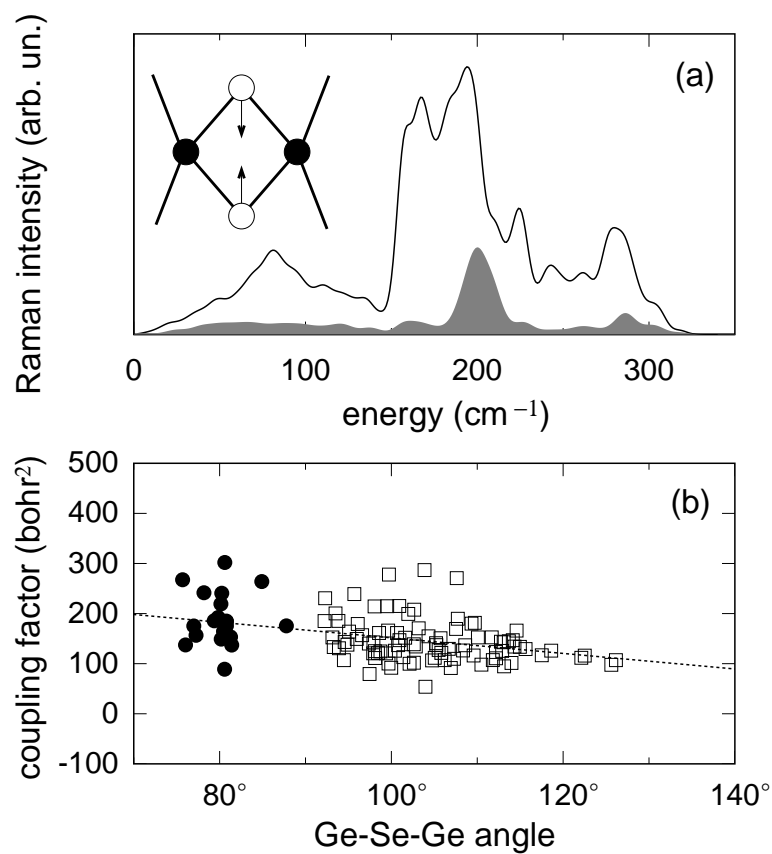
Figure 4.18: (a) Raman intensity (shaded) associated to in-phase Se bending vibrations in four-atom rings (see inset), compared to the full reduced HH Raman spectrum of Model I of v-GeSe$_2$ (solid). A Gaussian broadening of 4 cm^{-1} is used. (b) Isotropic coupling factor for Se bending motions vs Ge-Se-Ge angle for Se atoms in Model I. Only Se atoms twofold coordinated by Ge are considered, either inside (closed circles) or outside (open squares) of four-atom rings. The dotted line corresponds to a linear fit of the data.

duces the interval of the associated Raman intensity to 160–260 cm^{-1}. To understand this behavior, we then considered Se–Se bonds in an individual manner. We first projected the eigenmodes on the stretching motions associated to a given Se-Se bond, and then calculated the associated Raman intensity. For each Se-Se bond, this gave a sharp peak identifying a given frequency (not shown). In Fig. 4.19(b), the frequencies obtained in this way are displayed vs. the corresponding bond lengths, revealing a linear trend. The relation is particularly well satisfied in models I and II, while Model III shows larger deviations due to the enhanced level of disorder.

As can be inferred from the Se-Se partial pair correlation functions in Fig. 4.5, the width of the Se-Se bond-length distribution in Model I is comparable to the experimental result [25]. In view of the relation in Fig. 4.19(b), this further confirms that the contribution of Se-Se homopolar bonds to the HH Raman spectrum is spread over a large interval. To understand the extent of the observed Se-Se bond lengths in our models, we attempted to distinguish them according to their nearest neighbor coordination, but could not find any specific relation. Our results would therefore suggest that assignments of specific features to Se-Se stretching motions are doubtful. However, we estimate that a definite conclusion can only be reached through the consideration of a statiscally larger set of data.
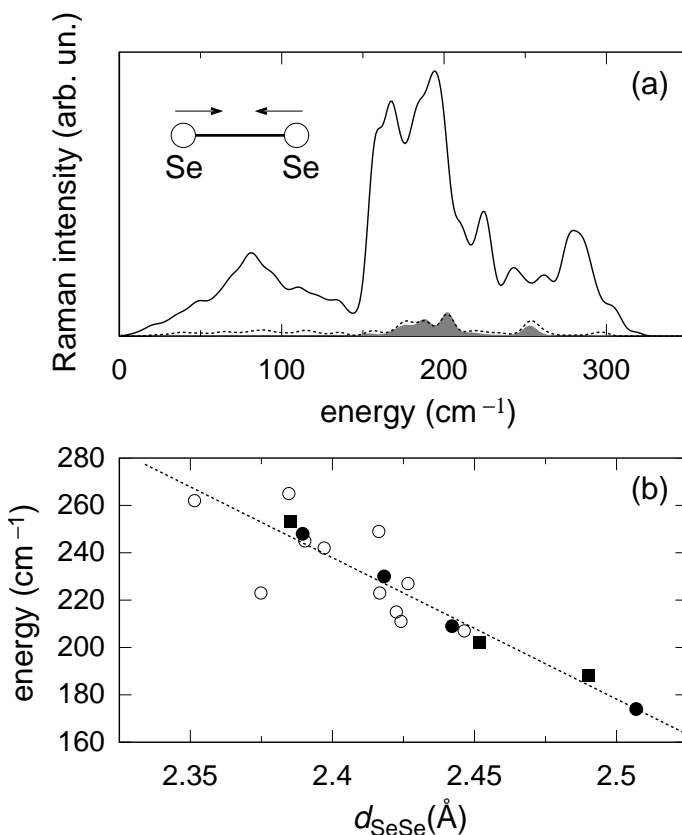

Figure 4.19: (a) Raman intensities associated to homopolar bonded Se atoms (dotted) and in particular to their Se-Se stretching vibrations (shaded), compared to the full reduced HH Raman spectrum of Model I of v-GeSe$_2$ (solid). A Gaussian broadening of 4 cm^{-1} is used. (b) Se-Se stretching-mode frequency vs bond-length d_{SeSe} for Models I (closed circles), II (closed squares), and III (open circles). The dotted line corresponds to a linear fit of all the data.

4.6   Conclusions

We studied the structural and vibrational properties of v-GeSe$_2$ within a density-functional scheme. In particular, we addressed the degree of chemical order in this vitreous material through the consideration of different model structures. Our investigation aimed at increasing our understanding of the structure of v-GeSe$_2$ by discriminating among the models through a comparison with experiment. We showed that diffraction probes are not sufficiently selective to discriminate among the models. The same observation also holds for the neutron vibrational density of states, which all models reproduce reasonably well. Significant differences among the model structures are observed for the infrared and Raman spectra. Comparison with experiment finally favors a structural model of v-GeSe$_2$ with strong chemical order.

Our best structural model shows a fair agreement with experiment for the infrared and Raman spectra. However, there appears to be significant room for further improvement. In particular, larger structural models appear instrumental to achieve this goal. Indeed, the finite-size effects affecting the level of distortion of the tetrahedra would be reduced, and consequently the quality of the infrared and Raman spectra would improve. Furthermore, larger statistics are needed to reliably represent spectral features associated to minority atomic arrangements.

Conclusions

In this thesis we investigated the vibrational spectra of the tetrahedrally bonded glasses v-SiO$_2$, v-GeO$_2$, and v-GeSe$_2$ by applying density-functional techniques.

Our investigation began with v-SiO$_2$ for which we considered three model structures differing by ring-statistics and intertetrahedral angle distribution. The comparisons between the vibrational spectra of these models helped us to extend our understanding of the relationship between the vibrational features and the underlying structure. Among the calculated vibrational spectra, we registered an excellent agreement with experiment for the Raman spectrum of one of these models.

Our study continued with v-GeO$_2$ for which we considered four model structures. Focusing on the larger of these structures, we showed that a Ge-O-Ge angular distribution with a mean value of 135° is consistent with the Raman spectrum. This mean angle is also in accord with diffraction and NMR experiments. Furthermore, we succeeded in assigning one feature appearing in the Raman spectrum to three-membered rings. For another one, we provided evidence in support of its bond-bending nature.

For the last material considered in this thesis, v-GeSe$_2$, we based our studies on three model structures generated according to two contending conceptions. The infrared and Raman spectra of our best structural model show a fair agreement with experiment, favoring the conception of a v-GeSe$_2$ structure showing strong chemical order.

An analysis which includes the vibrational spectra has now been applied to the series of tetrahedrally bonded glasses comprising v-SiO$_2$, v-GeO$_2$, and v-GeSe$_2$. The former two glasses feature a network of corner-sharing tetrahedra and differ by their packing density. Therefore, structural models of these two oxide glasses generally differ by their distributions of intertetrahedral angles. The present study indicates that the structure of v-GeSe$_2$ is also predominantly given by tetrahedra. Differences with respect to the former oxide glasses consist in the occurrence of edge-sharing tetrahedra and a low fraction of homopolar bonds. It is interesting to discuss how the structural differences between the networks of these three glasses affect the infared and Raman spectra. The consideration of various models of v-SiO$_2$ and v-GeO$_2$ differing by the distributions of intertetrahedral

angles led to minor differences in the infrared spectra. This should be contrasted with the important differences appearing in the infrared spectra of our models of v-GeSe$_2$, which show significant variations in the first-neighbor coordination shells. The sensitivity of Raman spectra on structural parameters, in particular on the intertetrahedral bond-angle distribution, was already emphasized for v-SiO$_2$ and v-GeO$_2$. The strong sensitivity of Raman spectra on structural properties is confirmed for the models of v-GeSe$_2$, which show more significant structural variations than bond-angle distributions. Overall, the modeling of vibrational spectra has proved to be a sensitive tool for refining our understanding of atomic arrangements in disordered materials. In particular, these spectra allow us to clearly discriminate among structural models, which are barely distinguishable on the basis of comparison with diffraction data.

Appendix A

A-1 Gaussian broadening

(I) The Gaussian broadening that we have used in order to broaden a discrete spectrum (ω_n, S_n) of N points, is obtained by applying a convolution with a Gaussian:

$$f(\omega) = \sum_n S_n \delta(\omega - \omega_n) \tag{A-1}$$

$$S(\omega) = \int f(\omega') \frac{1}{\sqrt{2\pi\sigma^2}} e^{-(\omega-\omega')^2/2\sigma^2} \, d\omega' \tag{A-2}$$

After the broadening we obtain a smooth continuous spectrum $S(\omega)$. We made use of this type of broadening in plotting the vibrational densities of states, the imaginary part of the dielectric function, the energy loss function, and the Raman spectra.

(II) However, $S(\omega)$ in Eq. (A-2) is not an interpolation of the points (ω_n, S_n). When an interpolated spectrum $S_g(\omega)$ is needed, we divide $S(\omega)$ by the density of points $\rho(\omega)$:

$$S_g(\omega) = S(\omega)/\rho(\omega) \tag{A-3}$$

$$\rho(\omega) = \sum_{n=1}^{N} \frac{1}{\sqrt{2\pi\sigma^2}} e^{-(\omega-\omega_n)^2/2\sigma^2}. \tag{A-4}$$

This type of broadening was used to broaden the structure factors in Secs. 2.3.2, 3.2.3, and 4.2.2.

A-2 Lorentzian broadening

We show in this section how we apply a Lorentzian broadening to Lorentzian functions like:

$$\mathcal{L}(\omega) = \frac{1}{\omega^2 - \omega_j^2}. \tag{A-5}$$

As first step we recast $\mathcal{L}(\omega)$ into the following shape

$$\frac{1}{\omega^2 - \omega_j^2} = \frac{1}{\omega + \omega_j} \cdot \frac{1}{\omega - \omega_j} \tag{A-6}$$

$$= \frac{1}{\omega + \omega_j} \cdot \frac{(\omega - \omega_j)}{(\omega - \omega_j)^2}. \tag{A-7}$$

Then we add an imaginary part $i\Gamma^2$ to the denominator $(\omega - \omega_j)^2$, so that we can finally write

$$\mathcal{L}(\omega) = \frac{(\omega - \omega_j)^3}{(\omega + \omega_j)\left\{(\omega - \omega_j)^4 + \Gamma^4\right\}} - i\Gamma^2 \frac{(\omega - \omega_j)^3}{(\omega + \omega_j)\left\{(\omega - \omega_j)^4 + \Gamma^4\right\}}. \tag{A-8}$$

In this way we have derived an expression that we apply to quantities involving Lorentzian functions such as Eq. (A-5). This occurs, for example, when we broaden the infrared spectra $\epsilon_1(\omega)$ [Eq. (2.36)]. The Lorentzian broadening proposed here is one of the possible forms of broadening that could be applied. One practical motivation that induced us to use this form of broadening is that the low frequency limit of $\epsilon_1(\omega)$ calculated with such a broadening coincides with the perturbative calculation of ϵ_0 [Eq. (2.35)].

Appendix B

B-1   Vibrational modes at Γ point of the α-quartz form of GeO$_2$

In order to more carefully examine the origin of the shift to lower frequencies observed in our calculated spectra, we here consider a system of known atomic structure, for which experimental frequencies are available. We address crystalline GeO$_2$ in the α-quartz structure [Fig. B-1]. Structural and vibrational calculations have been done using the PW code of the QUANTUM-ESPRESSO package [64]. We used a $3\times3\times3$ **k**-points grid. We made a cell-relaxation by varying the paramenter a of the cell and found that the energy shows a minimum for $a = 5.1$ Å, around 2% longer than its experimental value (4.9858 Å). Correspondingly, the equilibrium structure was found to show a Ge-O bond length larger than the experimental one by 2%, in excellent agreement with our results for vitreous GeO$_2$. Similarly, the vibrational frequencies of the α-quartz GeO$_2$ structure were found to underestimate by 7%, on average, the experimental ones ([143], Tab. B-1). Overall, this behavior agrees with the trends observed for v-GeO$_2$ and supports our assignment of the differences with respect to experiment to our density-functional setup rather than to the adopted model structure.
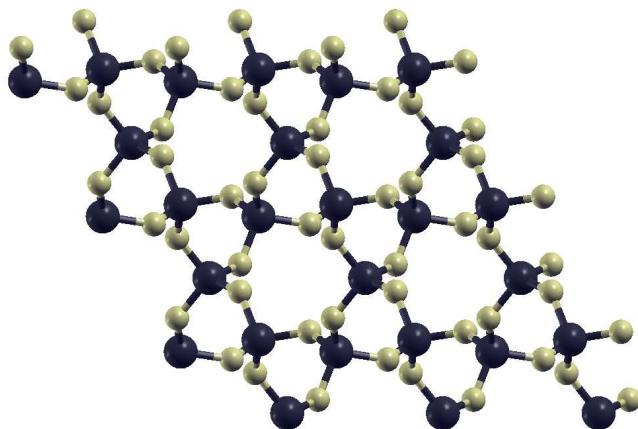

Figure B-1:   Snapshot of the α-quartz GeO$_2$ structure as found after cell-relaxation. Germanium and oxygen atoms atoms are depicted with dark and bright colors, respectively.

Table B-1: Vibrational frequencies of the α-quartz form of GeO_2 at the Γ point. The frequencies are given in cm^{-1}. The set of experimental vibrational frequencies, extrapolated to 0 K, are taken from the Raman spectra measurements of Ref. [143].

Theory	Expt.
A_1	
158	217
234	267
413	450
837	884
E	
111	127
195	170
239	249
302	331
486	
553	589
815	859
906	960

Bibliography

[1] *Insulating and semiconducting glasses* Vol. 17, edited by P. Boolchand (World Scientific Publishing, Singapore, 2000).

[2] S. R. Elliott, *Physics of amorphous materials*, 2nd Edn (Longman, London, 1990).

[3] A. Pasquarello and R. Car, Phys. Rev. Lett. **79**, 1766 (1997).

[4] P. Umari, X. Gonze, and A. Pasquarello, Phys. Rev. Lett. **90**, 027401 (2003).

[5] P. Umari and A. Pasquarello, Phys. Rev. Lett. **95**, 137401 (2005).

[6] *Light Scattering in Solids II*, edited by M. Cardona and G. Güntherod (Springer-Verlag, Berlin, 1982).

[7] P. Vashishta, R. K. Kalia, G. A. Antonio, and I. Ebbsjö, Phys. Rev. Lett. **62**, 1651 (1989); P. Vashishta, R. K. Kalia, and I. Ebbsjö, Phys. Rev. B **39**, 6034 (1989).

[8] B. W. H. van Beest, G. J. Kramer, and R. A. van Santen, Phys. Rev. Lett. **64**, 1955 (1990).

[9] M. Benoit and W. Kob, Europhys. Lett. **60**, 269 (2002).

[10] *Optical Fiber Communications*, edited by Li Tingye (Academic Press, Orlando, 1985), Vol. 1, p. 9; B. J. Ainslie and C. R. Day, J. Lightwave Technol. **4**, 967 (1986).

[11] M. L. Green, E. P. Gusev, R. Degraeve, and E. L. Garfunkel, J. Appl. Phys. **90**, 2057 (2001).

[12] J. L. Yarger, K. H. Smith, R. A. Nieman, J. Diefenbacher, G. H. Wolf, B. T. Poe, and P. F. McMillan, Science **270**, 1964 (1995); W. F. McDonough and S.-s Sun, Chem. Geol. **120**, 223 (1995); C. E. Manning, Earth Planet. Sci. Lett. **223**, 1 (2004);

[13] R. L. Mozzi and B. E. Warren, J. Appl. Crystallography **2**, 164 (1969).

[14] J. Neuefeind and K. D. Liss, Ber. Bunsenges. Phys. Chem. **100**, 1341 (1996).

[15] S. V. King, Nature (London) **213**, 1112 (1967).

[16] F. Mauri, A. Pasquarello, B. G. Pfrommer, Y. G. Yoon, and S. G. Louie, Phys. Rev. B **62**, R4786 (2000).

[17] A. C. Wright, G. Etherington, J. A. E. Desa, R. N. Sinclair, G. A. N. Connell, and J. C. Mikkelsen Jr. J. Non-Cryst. Solids **49**, 63 (1982).

[18] R. J. Hemley, H. K. Mao, P. M. Bell, and B. O. Mysen, Phys. Rev. Lett. **57**, 747 (1986).

[19] F. L. Galeener and G. Lucovsky, Phys. Rev. Lett. **37**, 1474 (1976).

[20] F. L. Galeener, A. J. Leadbetter, and M. W. Stringfellow, Phys. Rev. B **27**, 1052 (1983).

[21] A. Pasquarello and R. Car, Phys. Rev. Lett. **80**, 5145 (1998).

[22] F. L. Galeener, A. E. Geissberger, G. W. Ogar (Jr), and R. E. Loehman, Phys. Rev. B **28**, 4768 (1983).

[23] R. A. Barrio, F. L. Galeener, E. Martínez, and R. J. Elliott, Phys. Rev. B **48**, 15672 (1993). F. L. Galeener, R. A. Barrio, E. Martínez, and R. J. Elliott, Phys. Rev. Lett. **53**, 2429 (1984).

[24] W. H. Zachariasen J. Am. Chem. Soc. **54**, 3841 (1932); B. E. Warren, Phys. Rev. **45**, 657 (1934).

[25] I. Petri, P. S. Salmon, and H. E. Fisher, Phys. Rev. Lett. **84**, 2413 (2000).

[26] C. Massobrio, A. Pasquarello, and R. Car, Phys. Rev. Lett. **80**, 2324 (1998).

[27] C. Massobrio, A. Pasquarello, and R. Car, Phys. Rev. B **64**, 144205 (2001).

[28] M. Cobb and D. A. Drabold, Phys. Rev. B **56**, 3054 (1997).

[29] M. Cobb, D. A. Drabold, and R. L. Cappelletti, Phys. Rev. B **54**, 12162 (1996).

[30] P. Biswas, D. Tafen, and D. A. Drabold, Phys. Rev. B **71**, 054204 (2005).

[31] R. J. Nemanich, F. L. Galeener, J. C. Mikkelsen Jr, G. A. N. Connell, G. Etherington, A. C. Wright, and R. N. Sinclair, Physica **117**B & **118**B, 959 (1983); R. J. Nemanich, S. A. Solin, and G. Lucovsky, Solid State Commun. **21**, 273 (1977).

[32] S. Sugai, Phys. Rev. B **35**, 1345 (1987).

[33] K. Jackson, A. Briley, S. Grossman, D. V. Porezag, and M. R. Pederson Phys. Rev. B **60**, R14985 (1999).

[34] P. M. Bridenbaugh, G. P. Espinosa, J. E. Griffiths, J. C. Phillips, and J. P. Remeika, Phys. Rev. B **20**, 4140 (1979).

[35] J. Sarnthein, A. Pasquarello, and R. Car, Science **275**, 1925 (1997); A. Pasquarello, J. Sarnthein, and R. Car, Phys. Rev. B **57**, 14133 (1998).

[36] S. N. Taraskin and S. R. Elliott, Phys. Rev. B **55**, 117 (1997).

[37] L. Giacomazzi, P. Umari, and A. Pasquarello, Phys. Rev. Lett. **95**, 075505 (2005).

[38] U. Walter, D. L. Price, S. Susman, and K. J. Volin, Phys. Rev. B **37**, 4232 (1988).

[39] K. Murase, in Ref. [1], pp. 415-463.

[40] K. Vollmayr, W. Kob, and K. Binder, Phys. Rev. B **54**, 15808 (1996).

[41] M. Micoulaut, Y. Guissani, and B. Guillot, Phys. Rev. E **73**, 031504 (2006); M. Micoulaut, J. Phys. Condens. Matter **16**, L131 (2004).

[42] S. Baroni, S. de Gironcoli, A. Dal Corso, and P. Giannozzi, Rev. Mod. Phys. **73**, 515 (2001).

[43] F. Giustino and A. Pasquarello, Phys. Rev. Lett. **95**, 187402 (2005); Y. J. Chabal and K. Raghavachari, Surf. Science **502**, 41 (2002).

[44] A. Stirling, J. Chem. Phys. **104**, 1254 (1996).

[45] D. Porezag and M. R. Pederson, Phys. Rev. B **54**, 7830 (1996).

[46] P. Umari and A. Pasquarello, J. Phys. Condens. Matter **15**, S1547 (2003); P. Umari, A. Pasquarello, and A. Dal Corso, Phys. Rev. B **63**, 094305 (2001).

[47] P. Umari and A. Pasquarello, Phys. Rev. Lett. **89**, 157602 (2002).

[48] P. Umari and A. Pasquarello, Diam. Relat. Mat. **14**, 1255 (2005).

[49] R. D. Oeffner and S. R. Elliott, Phys. Rev. B **58**, 14791 (1998).

[50] W. J. Bresser, P. Boolchand, P. Suranyi, and J. P. de Neufville, Phys. Rev. Lett. **46**, 1689 (1981); P. Boolchand, J. Grothaus, W. J. Bresser and P. Suranyi, Phys. Rev. B **25**, 2975 (1982).

[51] M. P. Allen and D. J. Tildesley *Computer Simulations of Liquids* (Clarendon, Oxford, 1987); D. Frenkel and B. Smit, *Understanding Molecular Simulation*, second edition, (Academic Press, San Diego, 2002).

[52] A. Bongiorno and A. Pasquarello, Phys. Rev. Lett. **88**, 125901 (2002).

[53] X. Yuan and A. N. Cormack, J. Non-Cryst. Solids **283**, 69 (2001).

[54] P. Vashishta, R. K. Kalia, J. P. Rino, and I. Ebbsjö, Phys. Rev. B **41**, 12197 (1990);

[55] A. Rahman and P. Vashishta, in *The Physics of Superionic Conductors*, edited by J. W. Perram (Plenum, New York, 1983), p. 93; M. Parrinello, A. Rahman, and P. Vashishta, Phys. Rev. Lett. **50**, 1073 (1983).

[56] R. Car and M. Parrinello, Phys. Rev. Lett. **55**, 2471 (1985).

[57] D. Marx and J. Hutter, *Ab initio molecular dynamics: Theory and Implementation*, published in: *Modern Methods and Algorithms of Quantum Chemistry*, edited by J. Grotendorst, NIC Series, Vol. 1, (John von Neumann Institute for Computing, Jülich, 2000); G. Galli and A. Pasquarello, in *Computer Simulation in Chemical Physics*, edited by M. P. Allen and D. J. Tildesley (Kluwer, Dordrecht, 1993), pp. 261-313. G. Pastore, E. Smargiassi, and F. Buda, Phys. Rev. A **44**, 6334 (1991).

[58] R. Resta, *Berry Phase in Electronic Wavefunctions*, (Troisième Cycle de la Physique en Suisse Romande, Lausanne, 1996); Phys. Rev. Lett. **80**, 1800 (1998).

[59] J. Sarnthein, A. Pasquarello, and R. Car, Phys. Rev. B **52**, 12690 (1995); J. Sarnthein, A. Pasquarello, and R. Car, Phys. Rev. Lett. **74**, 4682 (1995).

[60] R. J. Bell, P. Dean, and D. C. Hibbins-Butler, J. Phys. C **4**, 1214 (1971).

[61] R. M. Van Ginhoven, H. Jónsson, and L. R. Corrales, Phys. Rev. B **71**, 024208 (2005).

[62] M. Benoit, S. Ispas, P. Jund, and R. Jullien, European Phys. J. B **13**, 631 (2000).

[63] A. Pasquarello, K. Laasonen , R. Car, C. Y. Lee, and D. Vanderbilt, Phys. Rev. Lett. **69**, 1982 (1992); K. Laasonen, A. Pasquarello, R. Car, C. Y. Lee, and D. Vanderbilt, Phys. Rev. B **47**, 10142 (1993).

[64] http://www.quantum-espresso.org.

[65] G. B. Bachelet, D. R. Hamann, and M. Schlüter, Phys. Rev. B **26**, 4199 (1982).

[66] D. Vanderbilt, Phys. Rev. B **41**, 7892 (1990).

[67] N. Binggeli, N. Troullier, J. L. Martins, and J. R. Chelikowsky, Phys. Rev. B **44**, 4771 (1991); F. Giustino and A. Pasquarello, Phys. Rev. Lett. **96**, 216403 (2006).

[68] F. J. Himpsel, Surf. Sci. **168**, 764 (1986); F. J. Grunthaner and P. J. Grunthaner, Mater. Sci. Rep. **1**, 65 (1986).

[69] Y. Waseda, *The structure of Non-Crystalline Materials* (McGraw-Hill, New York, 1980).

[70] A. Pasquarello, Phys. Rev. B **61**, 3951 (2000).

[71] S. Scandolo, P. Giannozzi, C. Cavazzoni, S. de Gironcoli, A. Pasquarello, and S. Baroni, Z. Kristallogr. **220**, 574 (2005).

[72] D. Stöffler and J. Arndt, Naturwissenshaften **56**, 100 (1969).

[73] D. L. Price and A. Pasquarello, Phys. Rev. B **59**, 5 (1999).

[74] D. L. Price and J. M. Carpenter, J. Non-Cryst. Solids **92**, 153 (1987).

[75] S. Susman, K. J. Volin, D. L. Price, M. Grimsditch, J. P. Rino, R. K. Kalia, P. Vashishta, G. Gwanmesia, Y. Wang, and R. C. Liebermann, Phys. Rev. B **43**, 1194 (1991).

[76] *International Tables for Crystallography*, Volume C, 1992, edited by A. J. C. Wilson (Kluwer, Dordrecht, 1992), Table 6.1.1.4, pp. 500-502.

[77] R. Brüning and D. Cottrell, J. Non-Cryst. Solids **325**, 6 (2003).

[78] A. B. Bhatia and D. E. Thornton, Phys. Rev. B **2**, 3004 (1970).

[79] D. L. Price, M-L. Saboungi, Y. S. Badyal, J. Wang, S. C. Moss, and R. L. Leheny, Phys. Rev. B **57**, 10496 (1998).

[80] C. Massobrio and A. Pasquarello, Phys. Rev. B **68**, 020201 (2003).

[81] X. Gonze and C. Lee, Phys. Rev. B **55**, 10355 (1997).

[82] M. Born, K. Huang, *Dynamical theory of crystal lattices*, (Oxford University Press, Oxford, 1954).

[83] P. Umari, X. Gonze, A. Pasquarello, Phys. Rev. B **69**, 235102 (2004); D. Donadio, M. Bernasconi, and F. Tassone, *ibid.* **68**, 134202 (2003).

[84] R. Resta, Rev. Mod. Phys. **66**, 899 (1994).

[85] J. M. Carpenter and D. L. Price, Phys. Rev. Lett. **54**, 441 (1985).

[86] D. L. Price and K. Sköld, in *Neutron Scattering*, edited by K. Sköld and D.L. Price (Academic, Orlando, 1986), p. 1.

[87] E. Fabiani, A. Fontana, and U. Buchenau, www.arXiv.org/abs/cond-mat/0502207

[88] U. Buchenau, M. Prager, N. Nücker, A. J. Dianoux, N. Ahmad, and W. A. Phillips, Phys. Rev. B **34**, 5665 (1986).

[89] E. Duval, A. Boukenter, and T. Achibat, J. Phys. Condens. Matter **2**, 10227 (1990).

[90] O. Pilla, A. Fontana, S. Caponi, F. Rossi, G. Viliani, M. Gonzalez, E. Fabiani, and C. Varsamis, J. Non-Cryst. Solids **322**, 53 (2003).

[91] Ph. Ghosez, J.P. Michenaud, and X. Gonze, Phys. Rev. B **58**, 6224 (1998).

[92] X. Gonze, D. C. Allan, and M. P. Teter, Phys. Rev. Lett. **68**, 3603 (1992); in *Phonon Scattering in Condensed Matter VII*, edited by M. Meissner and R.O. Pohl (Springer-Verlag, Berlin, 1993), p. 511.

[93] H. R. Philipp, in: *Handbook of optical constants of solids*, edited by D. Palik (Academic Press, San Diego, 1998), p. 749.

[94] *Handbook of chemistry and physics*, edited by D. R. Lide (CRC Press, New York, 1998).

[95] M. F. Thorpe and S. W. de Leeuw, Phys. Rev. B **33**, 8490 (1986).

[96] L. Giacomazzi, P. Umari, and A. Pasquarello, Phys. Rev. B **74**, 155208 (2006).

[97] L. Lapidus and G. F. Pinder, *Numerical Solutions of Partial Differential Equations in Science and Engineering*, (Wiley-Interscience, New York, 1982) p. 35.

[98] H. Kuzmany, *Solid-State Spectroscopy* (Springer-Verlag, Berlin, 1998).

[99] F. L. Galeener, Solid State Comm. **44**, 1037 (1982); F. L. Galeener, J. Non-Cryst. Solids **49**, 53 (1982).

[100] F. L. Galeener J. Non-Cryst. Solids **40**, 527 (1980).

[101] M. V. Wolkenstein, C. R. Acad. Sci. URSS **30**, 791 (1941); M. A. Eliashevich and M. V. Wolkenstein, J. Phys. (USSR) **9**, 101 (1944).

[102] F. L. Galeener, Phys. Rev. B **19**, 4292 (1979); P. N. Sen and M. F. Thorpe, Phys. Rev. B **15**, 4030 (1977).

[103] C. Guillon, J. Burgin, P. Langot, F. Vallée, and B. Hehlen, Appl. Phys. Lett. **86**, 081909 (2005).

[104] P. Umari and A. Pasquarello, Physica B **316**, 572 (2002).

[105] A. Rahmani, M. Benoit, C. Benoit Phys. Rev. B **68**, 184202 (2003).

[106] J. P. Perdew, J. A. Chevary, S. H. Vosko, K. A. Jackson, M. R. Pederson, and C. Fiolhais, Phys. Rev. B **46**, 6671 (1992).

[107] A. Dal Corso, A. Pasquarello, A. Baldereschi, and R. Car, Phys. Rev. B **53**, 1180 (1996).

[108] N. M. Ravindra, R. A. Weeks, and D. L. Kinser, Phys. Rev. B **36**, 6132 (1987); L. Pajasováá, Czech. J. Phsy. B **19**, 1265 (1969).

[109] D. M. Christie and J. R. Chelikowsky, Phys. Rev. B **62**, 14703 (2000); T. Tamura, G. H. Lu, R. Yamamoto, and M. Kohyama, Phys. Rev. B **69**, 195204 (2004).

[110] D. L. Price, M. L. Saboungi, and A. C. Barnes, Phys. Rev. Lett. **81**, 3207 (1998).

[111] C. E. Stone, A. C. Hannon, T. Ishihara, N. Kitamura, Y. Shirakawa, R. Sinclair, N. Umesaki, and A. C. Wright J. Non-Cryst. Solids **293-295**, 769 (2001).

[112] J. A. E. Desa, A. C. Wright, and R. N. Sinclair, J. Non-Cryst. Solids **99**, 276 (1988).

[113] N. Umesaki, T. M. Brunier, A. C. Wright, A. C. Hannon, and R. N. Sinclair, Physica B **213 & 214**, 490 (1995).

[114] S. Sampath, C. J. Benmore, K. M. Lantzky, J. Neuefeind, K. Leinenweber, D. L. Price, and J. L. Yarger, Phys. Rev. Lett. **90**, 115502 (2003).

[115] D. L. Price, A. J. G. Ellison, M. L. Saboungi, R. Hu, T. Egami, and W. S. Howells, Phys. Rev. B **55**, 11249 (1997).

[116] D. L. Price, S. C. Moss, R. Reijers, M. L. Saboungi, and S. Susman, J. Phys. Condens. Matter **1**, 1005 (1989).

[117] P. S. Salmon, A. C. Barnes, R. A. Martin, and G. J. Cuello, Phys. Rev. Lett. **96**, 235502 (2006).

[118] B. K. Sharma and M. Wilson, Phys. Rev. B **73**, 060201 (2006).

[119] W. A. Harrison, *Electronic Structure and the Properties of Solids*, (Dover Publications, New York, 1989), pp. 282-287.

[120] M. K. Murthy and J. Ip, Nature (London) **201**, 285 (1964).

[121] P. Umari and A. Pasquarello, Phys. Rev. B **68**, 085114 (2003).

[122] R. Hussin, R. Dupree and D. Holland, J. Non-Cryst. Solids **246**, 159 (1999).

[123] For a discussion on the width of the X_2 feature, we refer to Ref. [37].

[124] J. Burgin, C. Guillon, P. Langot, F. Vallée, and B. Hehlen, *to be published*.

[125] R. M. Martin and F. L. Galeener, Phys. Rev. B **23**, 3071 (1981).

[126] Q. Mei, C. J. Benmore, R. T. Hart, E. Bychkov, P. S. Salmon, C. D. Martin, F. M. Michel, S. M. Antao, P. J. Chupas, P. L. Lee, S. D. Shastri, J. B. Parise, K. Leinenweber, S. Amin, and J. L. Yarger, Phys. Rev. B **74**, 014203 (2006).

[127] P. S. Salmon and I. Petri, J. Phys. Condens. Matter **15**, S1509 (2003);

[128] K. Hachiya, J. Non-Cryst. Solids **291**, 160 (2001).

[129] N. Binggeli, N. Troullier, J. L. Martins, and J. R. Chelikowsky, Phys. Rev. B **44**, 4771 (1991); F. Giustino and A. Pasquarello, Phys. Rev. Lett. **96**, 216403 (2006).

[130] K. M Kandil, M. F. Kotkata, M. L. Theye, A. Gheorghiu, C. Senemaud, and J. Dixmier, Phys. Rev. B **51**, 17565 (1995).

[131] S. Susman, K. J. Volin, D. G. Montague, and D. L. Price, J. Non-Cryst. Solids **125**, 168 (1990).

[132] Neutron scattering lengths and cross sections are taken from: http://www.ncnr.nist.gov/resources/n-lengths/

[133] S. R. Elliott, Phys. Rev. Lett. **67**, 711 (1991).

[134] C. Massobrio and A. Pasquarello, J. Chem. Phys. **114**, 7976 (2001); C. Massobrio, A. Pasquarello, and R. Car, J. Am. Chem. Soc. **121**, 2943 (1999).

[135] R. L. Cappelletti, M. Cobb, D. A. Drabold, and W. A. Kamitakahara, Phys. Rev. B **52**, 9133 (1995).

[136] G. Lucovsky, Phys. Rev. B **15**, 5762 (1977).

[137] A. Feltz, H. Aust, and A. Blayer, J. Non-Cryst. Solids **55**, 179 (1983).

[138] X. Gonze, P. Ghosez and R. W. Godby, Phys. Rev. Lett. **74**, 4035 (1995).

[139] G. Dittmar and H. Schäfer, Acta Cryst. B **32**, 2726 (1976).

[140] Z. V. Popović and P. M. Nikolić, Solid State Commun. **27**, 561 (1978).

[141] G. Lucovsky, R. J. Nemanich, S. A. Solin, and R. C. Keezer, Solid State Commun. **17**, 1567 (1975).

[142] P. Tronc, M. Bensoussan, A. Brenac, and C. Sebenne, Phys. Rev. B **8**, 5947 (1973).

[143] T. P. Mernagh and L. G. Liu, Phys. Chem. Minerals **24**, 7 (1997).

Acknowledgments

Curriculum vitae

Name: Luigi Giacomazzi
Date and place of birth: 16.04.1978, Camposampiero (PD), Italy
Citizenship: Italian
Languages: Italian, English, French

Education:

- 2003-2006: Ph.D. thesis under the direction of Prof. A. Pasquarello at the
  Swiss Federal Institute of Technology in Lausanne (EPFL):
  "First principles vibrational spectra of tetrahedrally-bonded glasses: SiO_2,
  GeO_2, and $GeSe_2$"

- 2002: Diploma thesis under the direction of Prof. F. Ancilotto at the Università degli Studi di Padova: "Proprietà dinamiche di ^{4}He liquido: risultati della Teoria del Funzionale Densità". Degree in Physics with marks 110/110 *cum laude*.

- 1997-2002: Undergraduate studies of Physics at the Università degli Studi di Padova, Padova, Italy

List of Publications:

- Luigi Giacomazzi, C. Massobrio, and Alfredo Pasquarello, *First-Principles Investigation of the Structural and Vibrational Properties of Vitreous GeSe₂. Submitted for publication (Dec. 2006).*

- Luigi Giacomazzi, P. Umari, and Alfredo Pasquarello,
  Vibrational spectra of vitreous germania from first-principles.
  Physical Review B **74**, 155208 (2006).

- Luigi Giacomazzi, P. Umari, and Alfredo Pasquarello,
  Medium-Range Structural Properties of Vitreous Germania Obtained through First-Principles Analysis of Vibrational Spectra.
  Physical Review Letters, **95**, 075505 (2005).

- Luigi Giacomazzi, F. Toigo, and F. Ancilotto,
  Dynamics of liquid ^{4}He in confined geometries from time-dependent density functional calculations.
  Physical Review B **67**, 104501 (2003).